Search for a high-mass Higgs boson decaying to a W boson pair in pp collisions at s√=8s=8 TeV with the ATLAS detector

ATLAS Collaboration

DOI:
10.1007/JHEP01(2016)032

Document Version
Peer reviewed version

Citation for published version (Harvard):
ATLAS Collaboration 2016, 'Search for a high-mass Higgs boson decaying to a W boson pair in pp collisions at s√=8s=8 TeV with the ATLAS detector', *JHEP*. https://doi.org/10.1007/JHEP01(2016)032

EUROPEAN ORGANISATION FOR NUCLEAR RESEARCH (CERN)

Submitted to: JHEP

CERN-PH-EP-2015-185
19th January 2016

Search for a high-mass Higgs boson decaying to a W boson pair in pp collisions at $\sqrt{s} = 8$ TeV with the ATLAS detector

The ATLAS Collaboration

Abstract

A search for a high-mass Higgs boson H is performed in the $H \to WW \to \ell\nu\ell\nu$ and $H \to WW \to \ell\nu qq$ decay channels using pp collision data corresponding to an integrated luminosity of 20.3 fb^{-1} collected at $\sqrt{s} = 8$ TeV by the ATLAS detector at the Large Hadron Collider. No evidence of a high-mass Higgs boson is found. Limits on $\sigma_H \times \mathrm{BR}(H \to WW)$ as a function of the Higgs boson mass m_H are determined in three different scenarios: one in which the heavy Higgs boson has a narrow width compared to the experimental resolution, one for a width increasing with the boson mass and modeled by the complex-pole scheme following the same behavior as in the Standard Model, and one for intermediate widths. The upper range of the search is $m_H = 1500$ GeV for the narrow-width scenario and $m_H = 1000$ GeV for the other two scenarios. The lower edge of the search range is 200–300 GeV and depends on the analysis channel and search scenario. For each signal interpretation, individual and combined limits from the two WW decay channels are presented. At $m_H = 1500$ GeV, the highest-mass point tested, $\sigma_H \times \mathrm{BR}(H \to WW)$ for a narrow-width Higgs boson is constrained to be less than 22 fb and 6.6 fb at 95% CL for the gluon fusion and vector-boson fusion production modes, respectively.

Contents

1 Introduction

The boson discovered in 2012 by the ATLAS [1] and CMS [2] collaborations at the LHC matches the predictions for a Standard Model (SM) Higgs boson within the precision of current measurements [3, 4]. Several extensions of the SM predict heavy neutral scalars in addition to a low-mass scalar compatible with the discovered boson. Examples include generic models in which a low-mass Higgs boson mixes with a heavy electroweak singlet [5–10] to complete the unitarisation of WW scattering at high energies.

This paper reports the results of a search for a heavy neutral scalar by the ATLAS Collaboration in the decay mode into two W bosons. Two final states are used: $H \to WW \to \ell\nu\ell\nu$ and $H \to WW \to \ell\nu qq$ ($\ell = e, \mu$). In these final states, ATLAS has previously reported the results of searches for heavy Higgs bosons using 4.7 fb^{-1} of data collected at a centre-of-mass energy of 7 TeV [11, 12]. In the $H \to WW \to \ell\nu\ell\nu$ final state, a SM Higgs boson in the mass range $133\,\text{GeV} < m_H < 261\,\text{GeV}$ was excluded at 95% confidence level (CL), while the $H \to WW \to \ell\nu qq$ final state was not sensitive to a SM Higgs boson of any mass with the $\sqrt{s} = 7$ TeV dataset. The CMS Collaboration has performed a search for a heavy Higgs boson in the $H \to WW$ and $H \to ZZ$ channels [13]. From a combination of the two channels, a hypothetical second Higgs boson with couplings identical to those predicted by the Standard Model is excluded in the mass range $145\,\text{GeV} < m_H < 1000\,\text{GeV}$.

The analyses reported here improve the results in Refs. [11, 12] by using an integrated luminosity corresponding to 20.3 fb^{-1} of pp collision data at $\sqrt{s} = 8$ TeV collected by the ATLAS detector. Both analyses are designed to be sensitive to a heavy Higgs boson produced through either or both of the gluon-fusion (ggF) or vector-boson fusion (VBF) processes. Both also use a profile-likelihood fit to a distribution in which the hypothetical signal is peaked but background is monotonically decreasing in the search range in order to test for the presence of signal. The $H \to WW \to \ell\nu\ell\nu$ analysis uses the dilepton transverse mass distribution for the discriminant because the two neutrinos in the final state result in insufficient kinematic information to reconstruct the invariant mass of the WW system. The $H \to WW \to \ell\nu qq$ analysis uses as the discriminant the invariant mass of the WW system, reconstructed using the W mass as a kinematic constraint to recover the neutrino momentum up to a twofold ambiguity. The results of the searches are interpreted in three scenarios:

1. A Higgs boson with the couplings predicted by the SM for a Higgs boson at high mass and a width correspondingly increasing with m_H, and the lineshape modeled by the complex-pole scheme (CPS) for most mass hypotheses, as explained in Sec. 2. Accordingly, this is referred to as the CPS scenario.

2. A Higgs boson with a narrow width: labelled as narrow-width approximation ('NWA').

3. An intermediate-width ('IW') scenario, motivated by the electroweak singlet model.

Section 2 of this paper discusses the CPS lineshape model. Section 3 describes the ATLAS detector, the data sample and physics object reconstruction. Section 4 summarises the simulation of signal and background samples. The event selection and background estimation techniques used in the analyses are described in Sections 5 and 6. Systematic uncertainties affecting the analyses are discussed in Section 7. Distributions of the discriminants are shown in Section 8. Section 9 presents the interpretations of the

results from the $H \to WW \to \ell\nu\ell\nu$ and $H \to WW \to \ell\nu qq$ final states, as well as from their combination, in the scenarios listed above. Conclusions of the study are given in Section 10.

2 CPS lineshape model for a heavy Higgs boson

Narrower widths are allowed in general for Higgs bosons in extensions to the Standard Model, but to explore the implications of the width of the additional Higgs boson, the data are also interpreted using a signal hypothesis with a lineshape and width identical to a SM Higgs boson. The width of a SM Higgs boson increases with increasing mass. For example, it is $\sim 30\,\text{GeV}$ at $m_H = 400\,\text{GeV}$, and increases to $\sim 650\,\text{GeV}$ at $m_H = 1000\,\text{GeV}$. Up to $m_H \sim 400$ GeV, the lineshape of the WW invariant mass (m_{WW}) distribution is well described by a Breit–Wigner distribution with a running width, meaning that the Higgs boson propagator is calculated for each event based on m_{WW} as described in Ref. [14]. For $m_H \geq 400\,\text{GeV}$, the complex-pole scheme [15–17] provides a more accurate description. The CPS propagator is therefore used to describe the lineshape of the Higgs boson produced via both the ggF and VBF processes for $m_H \geq 400\,\text{GeV}$ [18–20]. The limits using this signal hypothesis are labeled "CPS scenario" even though a Breit–Wigner distribution is used for $m_H < 400\,\text{GeV}$. For that mass range the distributions are similar, so this is a minor simplification.

For a Higgs boson with a large width, the production cross section as well as the shapes of kinematic variables are affected by the interference between signal and non-resonant WW background. The interference is small for $m_H < 400\,\text{GeV}$, but is significant at higher masses, since it increases with increasing Higgs boson width. The effect of the interference is included in the signal samples which use the CPS lineshape, i.e. $m_H \geq 400\,\text{GeV}$. The interference calculations are described in Section 4.

3 Data sample and object reconstruction

The ATLAS detector [21] is a general-purpose particle detector used to investigate a broad range of physics processes. It includes inner tracking devices surrounded by a superconducting solenoid, electromagnetic (EM) and hadronic calorimeters and a muon spectrometer with a toroidal magnetic field. The inner detector (ID) consists of a silicon pixel detector, a silicon microstrip detector, and a straw tube tracker that also has transition radiation detection capability. The ID provides precision tracking of charged particles with pseudorapidity[1] $|\eta| < 2.5$. The calorimeter system covers the pseudorapidity range $|\eta| < 4.9$. It is composed of sampling calorimeters with either liquid argon or scintillator tiles as the active medium. The muon spectrometer provides muon identification and measurement for $|\eta| < 2.7$. During Run 1 of the LHC, the ATLAS detector used a three-level trigger system to select events for offline analysis.

Owing to the high LHC luminosity and a bunch separation of 50 ns, the number of proton–proton interactions occurring in the same bunch crossing is large (on average 20.7 in 2012). Proton–proton interactions

[1] ATLAS uses a right-handed coordinate system with its origin at the nominal interaction point (IP) in the centre of the detector and the z-axis along the beam pipe. The x-axis points from the IP to the centre of the LHC ring, and the y-axis points upward. Cylindrical coordinates (r, ϕ) are used in the transverse plane, ϕ being the azimuthal angle around the beam pipe. The pseudorapidity is defined in terms of the polar angle θ as $\eta = -\ln\tan(\theta/2)$.

Table 1: The minimum transverse momentum (p_{T}) requirements used at the different levels of the trigger. An "i" next to the threshold value indicates an isolation requirement that is less restrictive than the isolation requirement used in the offline selection. The single-lepton triggers with higher-p_{T} thresholds are more efficient at high lepton p_{T} than the lower-p_{T} triggers because of this isolation requirement. For dilepton triggers, the pair of thresholds corresponds to the leading and subleading lepton, respectively. The 0 GeV in the line describing the dimuon trigger indicates that only one muon is required at Level 1.

Name	Level-1 trigger	High-level (software) trigger
Single lepton		
e	18 OR 30 GeV	24i OR 60 GeV
μ	15 GeV	24i OR 36 GeV
Dilepton		
e, e	10 AND 10 GeV	12 AND 12 GeV
μ, μ	15 AND 0 GeV	18 AND 8 GeV
e, μ	10 AND 6 GeV	12 AND 8 GeV

in nearby bunch crossings also affect the detector response. These additional interactions are collectively referred to as event "pile-up"[2] and require the use of dedicated algorithms and corrections to mitigate its effect on particle identification, energy calibrations, and event reconstruction.

The triggers used in these analyses are listed in Table 1, together with the minimum transverse momentum (p_{T}) requirements at the different levels. Both the $H \to WW \to \ell\nu\ell\nu$ and the $H \to WW \to \ell\nu qq$ analyses use the single-lepton triggers while the dilepton triggers are used only by the $H \to WW \to \ell\nu\ell\nu$ analysis. The lepton trigger efficiencies are measured using Z boson candidates as a function of lepton p_{T} and η. The single-lepton trigger efficiencies are approximately 70% for muons with $|\eta| < 1.05$, 90% for muons in the range $1.05 < |\eta| < 2.40$, and $\geq 95\%$ for electrons in the range $|\eta| < 2.40$. Dilepton triggers increase the signal acceptance for the $H \to WW \to \ell\nu\ell\nu$ analysis by enabling lower lepton p_{T} thresholds to be used.

Events are required to have a primary vertex consistent with the known interaction region, with at least three associated tracks with $p_{\mathrm{T}} > 0.4$ GeV. If multiple collision vertices are reconstructed, the vertex with the largest summed p_{T}^2 of the associated tracks is selected as the primary vertex. Data quality criteria are applied to events to suppress non-collision backgrounds such as cosmic-ray muons, beam-related backgrounds or noise in the calorimeters. The resulting integrated luminosity is 20.3 fb^{-1} at $\sqrt{s} = 8$ TeV.

Electron candidates are required to have a well-reconstructed track in the ID pointing to a cluster of cells with energy depositions in the EM calorimeter. They are required to be in the range $|\eta| < 2.47$, excluding the range $1.37 < |\eta| < 1.52$ which corresponds to the transition region between the barrel and the endcap calorimeters. Only electrons with $E_{\mathrm{T}} > 15$ GeV are used in the analysis. The fine lateral and longitudinal segmentation of the calorimeter and the transition radiation detection capability of the ID allow for robust electron reconstruction and identification in the high pile-up environment. Criteria including the calorimeter shower shape, the quality of the match between the track and the cluster, and the amount of transition radiation emitted in the ID, are used to define a set of identification criteria [22–

[2] Multiple pp collisions occurring in the same (nearby) bunch crossing are referred to as in-time (out-of-time) pile-up.

24]. The "tight" criteria, which have the best background rejection, are used in the $H \to WW \to \ell\nu qq$ analysis. The $H \to WW \to \ell\nu\ell\nu$ analysis uses the "medium" selection, which is more efficient but admits more background, for electrons with $E_{\mathrm{T}} > 25\,\mathrm{GeV}$. For electrons with $15\,\mathrm{GeV} < E_{\mathrm{T}} < 25\,\mathrm{GeV}$, a likelihood-based electron selection at the "very tight" operating point is used for its improved background rejection.

Muon candidates are identified by matching tracks reconstructed in the ID with tracks reconstructed in the muon spectrometer [25]. The muon spectrometer track is required to have a track segment in each of the three layers of the spectrometer, while the ID track must have a minimum number of associated hits in each subdetector. In the $H \to WW \to \ell\nu\ell\nu$ analysis, muons are required to have $|\eta| < 2.5$ and $p_{\mathrm{T}} > 15\,\mathrm{GeV}$. For the $H \to WW \to \ell\nu qq$ analysis, muons must satsify $|\eta| < 2.4$ and $p_{\mathrm{T}} > 25\,\mathrm{GeV}$, since the sole lepton in the event must be within the acceptance of the trigger.

Additional selection criteria on the lepton isolation and impact parameter are used to reduce backgrounds from non-prompt leptons and lepton-like signatures produced by hadronic activity. These requirements are identical for the $H \to WW \to \ell\nu\ell\nu$ and $H \to WW \to \ell\nu qq$ analyses. Lepton isolation is defined using track-based and calorimeter-based quantities. The track isolation is based on the scalar sum Σp_{T} of all tracks with $p_{\mathrm{T}} > 0.4\,\mathrm{GeV}$ in a cone in η–ϕ space around the lepton, excluding the lepton track. The cone size is $\Delta R = \sqrt{(\Delta\phi)^2 + (\Delta\eta)^2} = 0.3$. The track isolation requires that Σp_{T} divided by the electron transverse energy E_{T} (muon p_{T}) be less than 0.10 (0.12) for $E_{\mathrm{T}}(p_{\mathrm{T}}) > 20\,\mathrm{GeV}$. For electrons (muons) with $15\,\mathrm{GeV} < E_{\mathrm{T}}(p_{\mathrm{T}}) < 20\,\mathrm{GeV}$, the threshold is 0.08.

The calorimeter isolation selection criterion is also based on a ratio. For electrons, it is computed as the sum of the transverse energies, ΣE_{T}, of surrounding energy deposits (topological clusters) in the EM and hadronic calorimeters inside a cone of size $\Delta R = 0.3$ around the candidate electron cluster, divided by the electron E_{T}. The cells within $\eta \times \phi = 0.125 \times 0.175$ around the cluster barycentre are excluded. The pile-up and underlying event contribution to the calorimeter isolation is estimated and subtracted event-by-event [26]. Electrons with $E_{\mathrm{T}} > 20\,\mathrm{GeV}$ are required to have relative calorimeter isolation less than 0.28. For $15\,\mathrm{GeV} < E_{\mathrm{T}} < 20\,\mathrm{GeV}$, the threshold decreases to 0.24.

For muons, the relative calorimeter isolation discriminant is defined as ΣE_{T} of EM and hadronic calorimeter cells above a noise threshold inside a cone of size $\Delta R = 0.3$ around the muon direction divided by the muon p_{T}. All calorimeter cells within a cone of size $\Delta R = 0.05$ around the muon candidate are excluded from the sum. A correction based on the number of reconstructed primary vertices in the event is applied to ΣE_{T} to compensate for extra energy due to pile-up. Muons with $p_{\mathrm{T}} > 25\,\mathrm{GeV}$ are required to have relative calorimeter isolation less than 0.30. Below that p_{T} value the threshold decreases in steps with decreasing p_{T}, with a minimum value of 0.12.

The significance of the transverse impact parameter, defined as the transverse impact parameter d_0 divided by its estimated uncertainty, σ_{d_0}, of tracks with respect to the primary vertex is required to satisfy $|d_0|/\sigma_{d_0} < 3.0$. The longitudinal impact parameter z_0 must be $|z_0| \sin\theta < 0.4$ mm for electrons and $|z_0| \sin\theta < 1.0$ mm for muons.

Jets are reconstructed from topological clusters of calorimeter cells [27–29] using the anti-k_t algorithm with a radius parameter of 0.4 [30]. The jet energy dependence on pile-up is mitigated by applying two data-derived corrections. One is based on the product of the event p_{T} density and the jet area [26]. The second correction depends on the number of reconstructed primary vertices and the mean number of

expected interactions. After these corrections, an energy- and η-dependent calibration is applied to all jets. Finally, a residual correction from *in situ* measurements is applied to refine the jet calibration. In both analyses, jets are required to have $p_{\mathrm{T}} > 25$ GeV if they have $|\eta| < 2.4$. For jets with $2.4 < |\eta| < 4.5$, the p_{T} threshold is raised to 30 GeV. The increased threshold in the forward region reduces the contribution from jet candidates produced by pile-up. To reduce the pile-up contribution further, jets within the inner detector acceptance are required to have more than 50% of the sum of the scalar p_{T} of their associated tracks due to tracks coming from the primary vertex.

Very heavy Higgs bosons give large momenta to their decay products. In the $H \to WW \to \ell\nu qq$ analysis, the dijet system produced by the W boson from such a decay is highly boosted and the jets overlap in the calorimeter, so they cannot always be resolved with the standard anti-k_t algorithm. Therefore, in this analysis the hadronic W decay can also be reconstructed as a single jet found by the Cambridge/Aachen algorithm [31], built from topological clusters with a radius parameter of 1.2, referred to as large-R jets. These jets can mitigate the loss of signal efficiency, and background can be reduced by selecting those with features typical of jets originating from two hard partons. These jets are selected using a mass-drop filter algorithm [32].

Jets containing b-hadrons are identified using a multivariate b-tagging algorithm [33, 34] which combines impact parameter information of tracks and the reconstruction of charm and bottom hadron decays. These analyses use a working point with an efficiency of 85% for b-jets and a mis-tag rate for light-flavour jets of 10.3% in simulated $t\bar{t}$ events. High b-jet tagging efficiency maximises top-quark background rejection, which is important for the sensitivity of analysis categories that require one or more jets.

In the $H \to WW \to \ell\nu\ell\nu$ analysis, two different definitions of missing transverse momentum are used. The calorimeter-based definition, $E_{\mathrm{T,calo}}^{\mathrm{miss}}$, is the magnitude of the negative vector sum of the transverse momenta of muons, electrons, photons, and jets. Clusters of calibrated calorimeter cells that are not associated with any of these objects are also included [35]. This definition takes advantage of the hermeticity of the calorimeters and their ability to measure energies of neutral particles. However, the resolution of the calorimeter-based quantity is degraded by the significant event pile-up. The resolution can be improved by using track-based measurements of the momenta of particles not associated with an identified object to replace the calorimeter cell based measurements. The tracks are required to have $p_{\mathrm{T}} > 0.5$ GeV and must originate from the primary vertex. In practice, the p_{T} of these tracks replace the E_{T} of calorimeter cells not associated with identified objects. The accurate primary-vertex association makes the track-based measurement more robust against pile-up than the calorimeter-based measurement. The quantity thus formulated is referred to as $p_{\mathrm{T}}^{\mathrm{miss}}$.

Using the direction of $p_{\mathrm{T}}^{\mathrm{miss}}$ relative to leptons and jets improves the rejection of Drell–Yan backgrounds in the $H \to WW \to \ell\nu\ell\nu$ final state. A quantity $p_{\mathrm{T,rel}}^{\mathrm{miss}}$ is defined as follows:

$$p_{\mathrm{T,rel}}^{\mathrm{miss}} = \begin{cases} p_{\mathrm{T}}^{\mathrm{miss}} \sin\Delta\phi_{\mathrm{near}} & \text{if } \Delta\phi_{\mathrm{near}} < \pi/2 \\ p_{\mathrm{T}}^{\mathrm{miss}} & \text{otherwise,} \end{cases} \tag{1}$$

where $\Delta\phi_{\mathrm{near}}$ is the azimuthal distance of the $p_{\mathrm{T}}^{\mathrm{miss}}$ and the nearest high-p_{T} lepton or jet. A calorimeter-based quantity $E_{\mathrm{T,rel}}^{\mathrm{miss}}$ is defined similarly. In Drell–Yan events, in which $E_{\mathrm{T}}^{\mathrm{miss}}$ arises from mismeasurement of the E_{T} or p_{T} of objects, these quantities tend to have small values, while in events with genuine $E_{\mathrm{T}}^{\mathrm{miss}}$

they have larger values on average. Selection using these quantities therefore rejects Drell–Yan events in preference to signal events.

4 Signal and background simulation

This section describes the signal and background Monte Carlo (MC) generators used in the analyses, the different signal models used in the hypothesis tests, and the cross-section calculations used to normalise backgrounds.

For most processes, separate MC programs are used to generate the hard scattering and to model the parton showering (PS), hadronisation, and underlying event (UE). Pythia8 [36], Pythia6 [37], Herwig [38] and Sherpa [39] are used for the latter three steps for the signal and for some of the background processes. When Herwig is used for the hadronisation and PS, the UE is modelled using Jimmy [40].

The parton distribution function (PDF) set from CT10 [41] is used for the Powheg [42] and Sherpa samples, while CTEQ6L1 [43] is used for the Alpgen [44], Herwig, GG2WW [45], Pythia6 and Pythia8 samples. Acceptances and efficiencies are obtained from a full simulation [46] of the ATLAS detector using either Geant4 [47], or Geant4 combined with a parameterised calorimeter simulation [48]. The simulation incorporates a model of the event pile-up conditions in the data, including both in-time and out-of-time pile-up.

4.1 Simulation and normalisation of signal processes

The Powheg generator combined with Pythia8 is used to model all signal processes. Heavy Higgs boson production via the ggF and VBF processes are considered in both the $H \to WW \to \ell\nu\ell\nu$ and $H \to WW \to \ell\nu qq$ analysis channels. Contributions from Higgs-strahlung and $t\bar{t}H$ production mechanisms are not considered owing to their very small cross sections at high Higgs boson masses. For leptonic W decays, the small contribution from leptonic $W \to \tau\nu \to \ell\nu\nu$ decays is included.

The ggF signal cross-section calculation includes corrections up to next-to-next-to-leading order (NNLO) in QCD [49–54]. Next-to-leading-order (NLO) electroweak (EW) corrections are also applied [55, 56], as well as QCD soft-gluon resummations up to next-to-next-to-leading logarithmic order (NNLL) [57]. These calculations are described in Refs. [14, 58, 59] and assume factorisation between the QCD and EW corrections. The VBF signal cross section is computed with approximate NNLO QCD corrections [60] and full NLO QCD and EW corrections [61–63]. The total width for the CPS scenario follows the SM predictions for high mass and has been calculated using Hdecay [64]. The branching fractions for the decay to WW as a function of m_H have been calculated using Prophecy4f [65, 66].

4.1.1 Signal samples for CPS scenario

Simulated Higgs boson samples with the width predicted by the SM as a function of m_H are generated using Powheg+Pythia8, at 20 GeV intervals for 220 GeV $\leq m_H \leq$ 580 GeV, and at 50 GeV intervals for

600 GeV $\leq m_H \leq$ 1000 GeV. The CPS-scenario interpretation is not performed for $m_H >$ 1000 GeV because of the large width of the resonance. For $m_H <$ 400 GeV, ggF and VBF samples are generated with the running-width Breit–Wigner propagator described in Section 2. For $m_H \geq$ 400 GeV, samples are generated using a CPS propagator. The calculations using the Breit–Wigner and the CPS propagators are in good agreement in the mass range below 400 GeV.

Calculations of the interference effect between resonant and non-resonant $gg \to WW$ production are available only at leading-order (LO) accuracy in QCD. Therefore, this effect is not directly included in the generation of the ggF and VBF CPS-scenario signal samples, and is implemented via event weighting at particle level. The full weighting procedure, including the treatment of associated uncertainties, is described in detail in Ref. [10] and summarised here.

For ggF signal samples, the interference weights are computed at LO using the MCFM [67] program, and rescaled to NNLO following the recommendations given in Ref. [10]. EW corrections are also included in the NNLO result used in the rescaling. The interference changes the total cross section. For $m_H >$ 400 GeV, it increases with increasing m_H, with an enhancement of almost a factor of four for $m_H =$ 1 TeV [18]. The interference is negative below $m_H \approx$ 400 GeV, but changes the cross section by 10% or less. The weighting procedure has also been performed with the GG2WW program; the results show good agreement with those using MCFM. The procedure accounts for theoretical uncertainties associated with the LO-to-NNLO scaling as well as those due to missing higher-order terms in the presently available interference estimation. The weights are applied to the signal samples only, because in the absence of signal there is no effect on the background. The sum of the weighted signal and the continuum WW background spectra approximately reproduces the results of the full calculation.

For VBF signal samples, the REPOLO tool provided by the authors of VBFNLO [68] is used to extract the interference weights. QCD scale and modelling uncertainties associated with the weights are also estimated using REPOLO. In this case, the LO-to-N(N)LO differences are expected to be small [60–62, 69, 70], and no explicit uncertainty is assigned to take these differences into account. Because not all of the information needed for the weight calculation is present in the fully reconstructed Monte Carlo samples, the weights are parameterised as a function of m_{WW} and m_H. A closure test comparing the signal lineshapes produced by the reweighting compared to the full calculation for the interference effects shows some differences, which are largest for m_{WW} far from m_H, but do not exceed 10%. These differences are treated as a systematic uncertainty on the signal.

For both ggF and VBF signal, the weights accounting for interference effects are calculated for each Higgs boson mass at which the samples are simulated, and applied as a function of m_{WW} in the range 0.5 $< m_{WW}/m_H <$ 1.5. The procedure modifies the event kinematics, including the m_{T} distribution used in the $H \to WW \to \ell\nu\ell\nu$ analysis. It has been shown that the weights describe the effect of interference on all kinematic variables used in the analyses [10].

4.1.2 Narrow-width signal samples

For the narrow-width Higgs boson scenario, signal samples are generated with Powheg+Pythia8 using a fixed 4.07 MeV-wide Breit–Wigner lineshape at 100 GeV intervals for 300 GeV $\leq m_H \leq$ 1500 GeV. Owing to the small width, the effect of interference between signal and continuum background is negligible over

the full mass range explored in the analyses [18, 71], therefore no interference weights are applied to these samples.

4.1.3 Signal samples for intermediate-width scenario

The intermediate-width scenario signal samples are derived by weighting the CPS signal samples to modify the width and lineshape and to account for interference. The lineshape of the heavy Higgs boson is weighted to one derived from a running-width Breit–Wigner propagator, and to scale the width down from the SM width. The interference weights are derived using the MCFM and REPOLO tools respectively for ggF and VBF signals, as in the CPS scenario, and are computed as a function of the modified width of the heavy scalar. The interference is a significant effect for $\Gamma_H \gtrsim 10\,\text{GeV}$. The weights are applied to the m_{WW} distribution and modify the event kinematics accordingly.

Intermediate-width signal scenarios are explored for a mass m_H between 200 GeV and 1000 GeV and a width in the range $0.2\Gamma_{H,\text{SM}} \leq \Gamma_H \leq 0.8\Gamma_{H,\text{SM}}$, where Γ_H is the width of the hypothetical particle and $\Gamma_{H,\text{SM}}$ is the width of a SM Higgs boson for the same mass. The extremes of a very narrow width and the same width as the SM are covered by the NWA and CPS scenarios.

4.2 Background processes

4.2.1 Background processes for the $H \to WW \to \ell\nu\ell\nu$ analysis

The MC generators used to simulate the background processes in the $H \to WW \to \ell\nu\ell\nu$ analysis, and the cross sections used to normalise them, are listed in Table 2. In this table, all W and Z boson decays into leptons (e, μ, τ) are included in the corresponding products of the cross sections (σ) and the branching ratios (BR).

Cross sections for top-quark and diboson processes are computed as follows. The $t\bar{t}$ production cross section is normalised to the NNLO+NNLL computation from TOP++2.0 [72–74], and single-top processes are normalised to NNLL calculations of the cross section [75–77]. The WW cross section is calculated at NLO accuracy in QCD using MCFM. The cross section for non-resonant gluon-fusion production is calculated at LO accuracy with GG2WW, including both WW and ZZ production and their interference.

Top-quark event generation uses Powheg+Pythia6, except for the single-top t-channel process $tq\bar{b}$, for which AcerMC [78]+Pythia6 is used. The WW background is also modelled using Powheg+Pythia6. For WW, WZ and ZZ backgrounds with two additional jets produced, the Sherpa generator is used for event modelling. The $W(Z/\gamma^*)$ process is simulated with Sherpa and Powheg+Pythia8, with m_{γ^*} extending down to the kinematic threshold and lepton masses included in the modeling of the γ^* decay. The $W\gamma$ and Drell–Yan processes are modelled using Alpgen+Herwig with merged LO matrix element calculations of up to five jets. The merged samples are normalised to the NLO calculation of MCFM (for $W\gamma$) or the NNLO calculation of DYNNLO [79, 80] (for Z/γ^*). A Sherpa sample is used to model the $Z\gamma \to \ell\ell\gamma$ background. The cross section of this process is normalised to NLO using MCFM. The W+ jets background shape and normalisation are derived from data, as described in Section 5.2, so no simulated W+ jets events are used.

Table 2: Monte Carlo generators used to model the background processes in the $H \to WW \to \ell\nu\ell\nu$ analysis. All leptonic decay branching ratios (e, μ, τ) of the W and Z bosons are included in the product of cross section (σ) and branching ratio (BR).

Background	MC generator	$\sigma \cdot$ BR (pb)
$t\bar{t}$	POWHEG + PYTHIA6	26.6
tW	POWHEG + PYTHIA6	2.35
$tq\bar{b}$	ACERMC + PYTHIA6	28.4
$t\bar{b}$	POWHEG + PYTHIA6	1.82
$q\bar{q}/g \to WW$	POWHEG + PYTHIA6	5.68
$gg \to WW$	GG2WW+ HERWIG	0.20
QCD WW + 2 jets	SHERPA	0.568
EW WW + 2 jets	SHERPA	0.039
Z/γ^*+jets ($m_{\ell\ell} \geq 10$ GeV)	ALPGEN + HERWIG	16.5×10^3
EW Z/γ^* (includes t-channel)	SHERPA	5.36
$Z^{(*)}Z^{(*)} \to 4\ell$	POWHEG + PYTHIA8	0.73
$W(Z/\gamma^*)(m_{(Z/\gamma^*)} < 7$ GeV)	SHERPA	12.2
$Z\gamma(p_{\mathrm{T}}^{\gamma} > 7$ GeV)	SHERPA	163
$W\gamma$	ALPGEN + HERWIG	369
Higgs boson ($m_H = 125$ GeV)	POWHEG + PYTHIA8	0.60

4.2.2 Background processes for the $H \to WW \to \ell\nu qq$ analysis

Several different Monte Carlo generators are used to simulate the background to the $H \to WW \to \ell\nu qq$ process. The processes used to model the background in the analysis are shown in Table 3. In general, the treatment follows that of the $H \to WW \to \ell\nu\ell\nu$ analysis, with the exceptions described here.

The W+jets background is modelled with the SHERPA generator version 1.4.1. In order to have enough events for a background prediction at high mass, the SHERPA samples are generated in multiple bins of p_{T}^{W}. The bin boundaries are: 40–70 GeV, 70–140 GeV, 140–280 GeV, 280–500 GeV, and > 500 GeV. An inclusive sample is used for $p_{\mathrm{T}}^{W} < 40$ GeV. Samples of W bosons with only electroweak vertices are also generated to ensure sufficiently good modelling of this background in the VBF topology.

The top-quark background is modelled using the same generators as in the $H \to WW \to \ell\nu\ell\nu$ analysis. Events in the $t\bar{t}$ sample are reweighted according to the p_{T} of the $t\bar{t}$ system and the individual top quarks to improve the kinematic agreement between the data and the POWHEG prediction, following the prescription outlined in Ref. [81] based on the measurements of Ref. [82]. This treatment is not needed for the $H \to WW \to \ell\nu\ell\nu$ analysis because the distributions affected are primarily the number of jets and the jet p_{T}, and the analysis is not sensitive to either of these because of the normalisation of the top-quark background individually in each jet bin. The Z+jets background is also generated via SHERPA and, like the SHERPA W+jets background, uses samples binned in p_{T}^{Z}, with a binning identical to the p_{T}^{W} used for the W+jets samples.

Table 3: Monte Carlo generators used to model the background processes in the $H \to WW \to \ell\nu qq$ analysis, and the associated cross sections σ. Leptonic decay branching ratios BR of the W and Z bosons are not included in the number quoted unless explicitly indicated in the process name.

Background	MC generator	$\sigma \cdot$ BR (pb)
$t\bar{t}$	POWHEG + PYTHIA6	252.9
tW	POWHEG + PYTHIA6	22.4
$tq\bar{b}$	AcerMC + PYTHIA6	28.4
$t\bar{b}$	POWHEG + PYTHIA6	1.82
$W \to \ell\nu$	SHERPA	35.6×10^3
$W \to \ell\nu$ VBF	SHERPA	12.6
$W\gamma \to \ell\nu\gamma$	ALPGEN + HERWIG	369
$Z \to \ell\ell$	SHERPA	3.62×10^3
$Z\gamma \to \ell\ell\gamma$ ($p_{\mathrm{T}}^{\gamma} > 10$ GeV)	SHERPA	96.9
WW	HERWIG	32.5
WZ	HERWIG	12.0
ZZ	HERWIG	4.69

The HERWIG generator is used for the WW, WZ, and ZZ processes. These samples are produced with inclusive vector boson decays and a single-lepton filter at the event generation stage.

5 The $H \to WW \to \ell\nu\ell\nu$ analysis

In the $H \to WW \to \ell\nu\ell\nu$ channel, the final state is two oppositely charged leptons and two neutrinos, which are reconstructed as missing transverse momentum. Additional jets may be present from QCD radiation or from the scattering quarks in the VBF production mode. The analysis described here is similar to the one designed to study the Higgs boson with $m_H \approx 125$ GeV in the $WW \to \ell\nu\ell\nu$ final state [83], with adaptations made to enhance the sensitivity for a high-mass Higgs boson.

5.1 Event selection

The event is required to have two oppositely charged leptons and no additional lepton with $p_{\mathrm{T}} > 10$ GeV, with the higher- and lower-p_{T} leptons respectively satisfying $p_{\mathrm{T}} > 22$ GeV and $p_{\mathrm{T}} > 10$ GeV. Both leptons must satisfy the quality criteria discussed in Section 3. Background from low-mass resonances constitutes a significant contribution, and is rejected by requiring $m_{\ell\ell} > 10$ GeV in the same-flavour channel and $m_{\ell\ell} > 12$ GeV in the different-flavour channel, in which resonances decaying to $\tau\tau$ may contribute. In the same-flavour channel, a veto on Z bosons is applied by requiring $|m_{\ell\ell} - m_Z| > 15$ GeV. These criteria form the preselection.

Table 4: Event selection criteria used to define the signal regions in the $H \to WW \to \ell\nu\ell\nu$ analysis. The criteria specific to different-flavour (DF) and same-flavour (SF) channels are noted as such; otherwise, they apply to both. Preselection applies to all N_{jet} categories. In the ≥2 jets category, the rapidity gap is the rapidity range spanned by the two leading jets.

Category	$N_{\text{jet}} = 0$	$N_{\text{jet}} = 1$	$N_{\text{jet}} \geq 2$
Preselection	Two isolated leptons ($\ell = e, \mu$) with opposite charge $p_{\text{T}}^{\text{lead}} > 22$ GeV, $p_{\text{T}}^{\text{sublead}} > 10$ GeV DF: $m_{\ell\ell} > 10$ GeV SF: $m_{\ell\ell} > 12$ GeV, $\lvert m_{\ell\ell} - m_Z \rvert > 15$ GeV		
Lepton p_{T}	$p_{\text{T}}^{\text{lead}} > 60$ GeV $p_{\text{T}}^{\text{sublead}} > 30$ GeV	$p_{\text{T}}^{\text{lead}} > 55$ GeV $p_{\text{T}}^{\text{sublead}} > 35$ GeV	$p_{\text{T}}^{\text{lead}} > 45$ GeV $p_{\text{T}}^{\text{sublead}} > 20$ GeV
Missing transverse momentum	DF: $p_{\text{T}}^{\text{miss}} > 45$ GeV SF: $E_{\text{T,rel}}^{\text{miss}} > 45$ GeV SF: $p_{\text{T,rel}}^{\text{miss}} > 65$ GeV	DF: $p_{\text{T}}^{\text{miss}} > 35$ GeV SF: $E_{\text{T,rel}}^{\text{miss}} > 45$ GeV SF: $p_{\text{T,rel}}^{\text{miss}} > 70$ GeV	DF: $E_{\text{T,calo}}^{\text{miss}} > 25$ GeV SF: $E_{\text{T,calo}}^{\text{miss}} > 45$ GeV -
General selection	- $p_{\text{T}}^{\ell\ell} > 60$ GeV	$N_{b\text{-jet}} = 0$ -	$N_{b\text{-jet}} = 0$ $p_{\text{T}}^{\text{tot}} < 40$ GeV
VBF topology	- - - -	- - - -	$m_{jj} > 500$ GeV $\Delta y_{jj} > 4.0$ No jet ($p_{\text{T}} > 20$ GeV) in rapidity gap Both ℓ in rapidity gap
$H \to WW \to \ell\nu\ell\nu$ topology	$m_{\ell\ell} > 60$ GeV $\Delta\eta_{\ell\ell} < 1.35$	$m_{\ell\ell} > 65$ GeV $\Delta\eta_{\ell\ell} < 1.35$	DF: $m_{\ell\ell} > 60$ GeV, SF: $m_{\ell\ell} > 45$ GeV $\Delta\eta_{\ell\ell} < 1.85$

The signal and background compositions depend strongly on the final-state jet multiplicity (N_{jet}). For $N_{\text{jet}} = 0$, the signal is predominantly from the ggF process, and WW events dominate the background. For $N_{\text{jet}} = 1$, both the ggF and VBF signal processes contribute, and the large majority of background events are from WW and top-quark events, which contribute approximately equally to the background. For $N_{\text{jet}} \geq 2$, the signal originates mostly from the VBF process and top-quark events dominate the background. The analysis is consequently divided into $N_{\text{jet}} = 0$, 1 and ≥ 2 categories.

The event selection in the various jet multiplicity categories is optimised using the BumpHunter [84] program, maximising the quantity $s/\sqrt{(b + (\Delta b)^2)}$, where s and b are the numbers of signal and background events, respectively, and Δb represents the systematic uncertainty on the background. The value $\Delta b = 10\%$ is used. The optimisation has also been performed with $\Delta b = 20\%$ to test for sensitivity to the assumed systematic uncertainties, but the resulting selection is not significantly different from the one adopted. The optimisation is performed separately for the different- and same-flavour channels. The optimised event selection criteria that define the signal regions (SRs) in the analysis are summarised in Table 4.

Owing to the topology of $H \to WW \to \ell\nu\ell\nu$ events, a selection on the missing transverse momentum is useful. In the different-flavour channel in both the $N_{\text{jet}} = 0$ and $N_{\text{jet}} = 1$ categories, requirements are imposed on $p_{\text{T}}^{\text{miss}}$. In the same-flavour channel in these N_{jet} categories, selections on $p_{\text{T,rel}}^{\text{miss}}$ and $E_{\text{T,rel}}^{\text{miss}}$ are used since, as explained in Section 3, these quantities efficiently reject Drell–Yan events. In the $N_{\text{jet}} \geq 2$ category, $E_{\text{T,calo}}^{\text{miss}}$ thresholds are used in both the different- and same-flavour channels. Selection using $p_{\text{T,rel}}^{\text{miss}}$ or $E_{\text{T,rel}}^{\text{miss}}$ in this category rejects a large fraction of signal events and is not optimal; they are therefore not used.

In the $N_{\text{jet}} = 0$ category, additional requirements on the p_{T} of the dilepton system $p_{\text{T}}^{\ell\ell}$ and on $m_{\ell\ell}$ are applied. In the $N_{\text{jet}} = 1$ category, a b-jet veto is applied to suppress the top background, and a selection on $m_{\ell\ell}$ is imposed. To orthogonalise the $N_{\text{jet}} = 0$ and $N_{\text{jet}} = 1$ signal regions with respect to the WW control regions (Section 5.2), the pseudorapidity difference $\Delta\eta_{\ell\ell}$ between the two leptons is required to be smaller than 1.35.

The $N_{\text{jet}} \geq 2$ category is optimised to extract the Higgs boson signal produced via vector-boson fusion. The invariant mass m_{jj} of the two highest-p_{T} jets, referred to as the tagging jets, is required to be larger than 500 GeV. The magnitude of the rapidity difference between the tagging jets, Δy_{jj}, is required to be larger than 4.0. In addition, the event must have no additional jets with $p_{\text{T}} > 20$ GeV within the rapidity gap of the tagging jets, while both leptons are required to be within this rapidity gap. A b-jet veto is applied, and the total transverse momentum $p_{\text{T}}^{\text{tot}}$ in the event is required to be smaller than 40 GeV. The quantity $p_{\text{T}}^{\text{tot}}$ is defined as the magnitude of $\boldsymbol{p}_{\text{T}}^{\ell 1} + \boldsymbol{p}_{\text{T}}^{\ell 2} + \boldsymbol{p}_{\text{T}}^{\text{miss}} + \sum \boldsymbol{p}_{\text{T}}^{\text{jets}}$, where the sum is over all jets that pass the nominal analysis jet selection. Selections on $m_{\ell\ell}$ are applied as in the $N_{\text{jet}} \leq 1$ categories, and $\Delta\eta_{\ell\ell} < 1.85$ is required. For a Higgs boson with $m_H = 300$ GeV and the ratio of ggF and VBF cross sections predicted by the SM, 83% of the total signal selected in the $N_{\text{jet}} \geq 2$ category is produced by the VBF process. In the $N_{\text{jet}} = 0$ and $N_{\text{jet}} = 1$ categories, these fractions are 2% and 12%, respectively. The signal fractions from the VBF process increase with increasing m_H.

The discriminant used to derive the final results in this analysis is the transverse mass m_{T}, defined as:

$$m_{\text{T}} = \sqrt{(E_{\text{T}}^{\ell\ell} + E_{\text{T}}^{\text{miss}})^2 - |\mathbf{p}_{\text{T}}^{\ell\ell} + \mathbf{E}_{\text{T}}^{\text{miss}}|^2}, \tag{2}$$

where $E_{\text{T}}^{\ell\ell} = \sqrt{|\mathbf{p}_{\text{T}}^{\ell\ell}|^2 + m_{\ell\ell}^2}$.

5.2 Background determination

The major backgrounds in this analysis are top-quark and WW production, with additional contributions from W/Z+jets, multijets, and the diboson processes WZ, $W\gamma$, $W\gamma^*$, and ZZ. The top-quark and WW backgrounds are normalised to data in control regions (CRs) defined by criteria similar to those used for the SR, but with some requirements loosened or reversed to obtain signal-depleted samples enriched in the relevant backgrounds. This normalisation is done through a simultaneous fit to the signal region and all control regions, as described in Section 9.1. This fit uses the complete background prediction in each region in order to account for the presence of other backgrounds and the potential small presence of signal. In particular, any background whose normalisation is determined by a control region is scaled by the same normalisation factor in all signal and control regions, not just its own control region. The following subsections describe the methods used to estimate the most important backgrounds, namely, WW, top-quark events, and W+jets, in more detail. The Drell–Yan and non-WW diboson backgrounds are small, and their predictions are computed from simulation. The small background from the Higgs boson with $m_H \approx 125$ GeV is also included. The predicted cross section, branching ratio, and kinematics for the SM Higgs boson are used. With few exceptions, the background estimates use the same techniques as Ref. [83]. They are described there in more detail, and summarized here.

Table 5: Event selection criteria for the $N_{\text{jet}} = 0$ and $N_{\text{jet}} = 1$ WW control regions in the $H \to WW \to \ell\nu\ell\nu$ analysis. The criteria that are different with respect to the SR definition are shown. Only the different-flavour final state is used.

Category	$N_{\text{jet}} = 0$	$N_{\text{jet}} = 1$
Lepton transverse momentum	$p_{\text{T}}^{\text{lead}} > 22$ GeV $p_{\text{T}}^{\text{sublead}} > 15$ GeV	
Missing transverse momentum	$p_{\text{T}}^{\text{miss}} > 20$ GeV	$p_{\text{T}}^{\text{miss}} > 35$ GeV
General selection and $H \to WW \to \ell\nu\ell\nu$ topology	-	$N_{b\text{-jet}} = 0$
	$p_{\text{T}}^{\ell\ell} > 35$ GeV	-
	$m_{\ell\ell} > 75$ GeV	$m_{\ell\ell} > 75$ GeV
	$\Delta\eta_{\ell\ell} > 1.35$	$\Delta\eta_{\ell\ell} > 1.35$

5.2.1 WW background

In the $N_{\text{jet}} \leq 1$ categories, the WW background is normalised using a CR defined with the selection summarised in Table 5. To orthogonalise the WW CRs to the $N_{\text{jet}} = 0$ and $N_{\text{jet}} = 1$ SRs, the selection on $\Delta\eta_{\ell\ell}$ is reversed with respect to the SR definitions: $\Delta\eta_{\ell\ell} > 1.35$ is required. Only the different-flavour final states are used to determine the WW background, and the purity is 70.5% and 40.6% in the $N_{\text{jet}} = 0$ and $N_{\text{jet}} = 1$ categories, respectively. The normalisation factors obtained from the simultaneous fit to the signal and control regions are 1.18 ± 0.04 for the $N_{\text{jet}} = 0$ CR and 1.13 ± 0.08 for the $N_{\text{jet}} = 1$ CR, where the uncertainty quoted includes only the statistical contribution. The high normalisation factor for WW events with zero jets has been studied in Ref. [83], and results from poor modelling of the jet veto efficiency. The WW prediction in the $N_{\text{jet}} \geq 2$ category is taken from simulation, because it is difficult to isolate a kinematic region with a sufficient number of WW events and a small contamination from the top-quark background.

Figure 1 shows the m_{T} distributions in the $N_{\text{jet}} \leq 1$ WW CRs. Normalisation factors obtained from the top CRs as well as from the WW CRs have been applied to these distributions.

5.2.2 $t\bar{t}$ and single top background

Top-quark events can be produced as a $t\bar{t}$ pair, or in association with a W boson or another flavour of quark. In the $H \to WW \to \ell\nu\ell\nu$ analysis, contributions from $t\bar{t}$ and single-top events are estimated together, with their relative contributions determined by the predicted cross sections and MC simulation of the acceptances, since it is not easy to kinematically separate the two processes and the contribution from single top is relatively small.

Owing to the difficulty of defining reasonably pure control regions in the $N_{\text{jet}} = 0$ category, the top-quark background in this category is not estimated from the likelihood fit. The jet veto survival probability (JVSP) procedure, described in more detail in Ref. [85], is employed instead. In this method, the normalisation is derived from the top-quark event yield determined in a control region defined by events with a

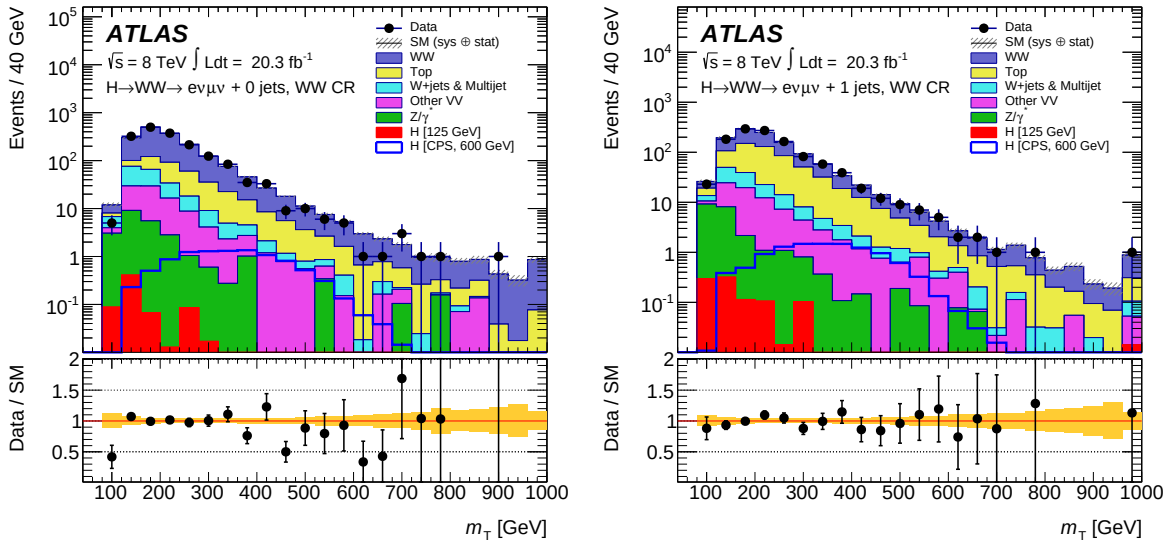

Figure 1: Transverse mass distribution in the $N_{\text{jet}} = 0$ (left) and $N_{\text{jet}} = 1$ (right) WW control regions of the $H \to WW \to \ell\nu\ell\nu$ analysis. Only the different-flavour final state is used. In each figure, the last bin contains the overflow. The combined statistical and systematic uncertainties on the prediction are shown by the hatched band in the upper pane and the shaded band in the lower pane. Normalisation factors obtained from a comparison of data and prediction have been applied in these figures.

different-flavour opposite-sign lepton pair, any number of jets, and $p_{\text{T}}^{\text{miss}} > 45$ GeV. This sample is dominated by top-quark events. The estimated top-quark event yield is the total number of events N_{CR} passing this selection minus the expected contribution B_{CR} from other processes. The theoretical cross sections and acceptances from MC simulation are used to calculate B_{CR}, except the W+jets background, for which the data-derived estimate described later in this section is used. The resulting estimated top-quark event yield is multiplied by the fraction ϵ_0 of top-quark events with no reconstructed jets obtained from simulation in the CR. This fraction is corrected using data from a second CR defined like the first, with the additional requirement of at least one b-tagged jet. The fraction of events in this CR with zero jets in addition to the b-tagged one is measured in both data and simulated top-quark events, denoted f_0^{data} and f_0^{MC}, respectively. Using these inputs, the estimated number of top-quark background events $N_{\text{top}}^{\text{est.}}$ in the $N_{\text{jet}} = 0$ signal region is estimated as:

$$N_{\text{top}}^{\text{est.}} = (N_{\text{CR}} - B_{\text{CR}}) \cdot \epsilon_0 \cdot (f_0^{\text{data}} / f_0^{\text{MC}})^2 \cdot \epsilon_{\text{rest}} \,, \tag{3}$$

where ϵ_{rest} is the efficiency of the $N_{\text{jet}} = 0$ selection requirements applied after the jet veto, derived from simulated top-quark events. The theoretical uncertainties on the quantities derived from top-quark MC simulation, namely ϵ_0, f_0^{MC}, and ϵ_{rest}, are described in Section 7.

In the $N_{\text{jet}} = 1$ and $N_{\text{jet}} \geq 2$ categories, the normalisation of the top-quark background is determined from control regions. As with the WW CR, and unlike the $N_{\text{jet}} = 0$ CRs, these are included in the simultaneous fit with the signal regions. These CRs are defined identically to the respective signal regions, except that the $p_{\text{T}}^{\text{miss}}$ threshold is lowered to 20 GeV and the veto on b-tagged jets is inverted to require exactly

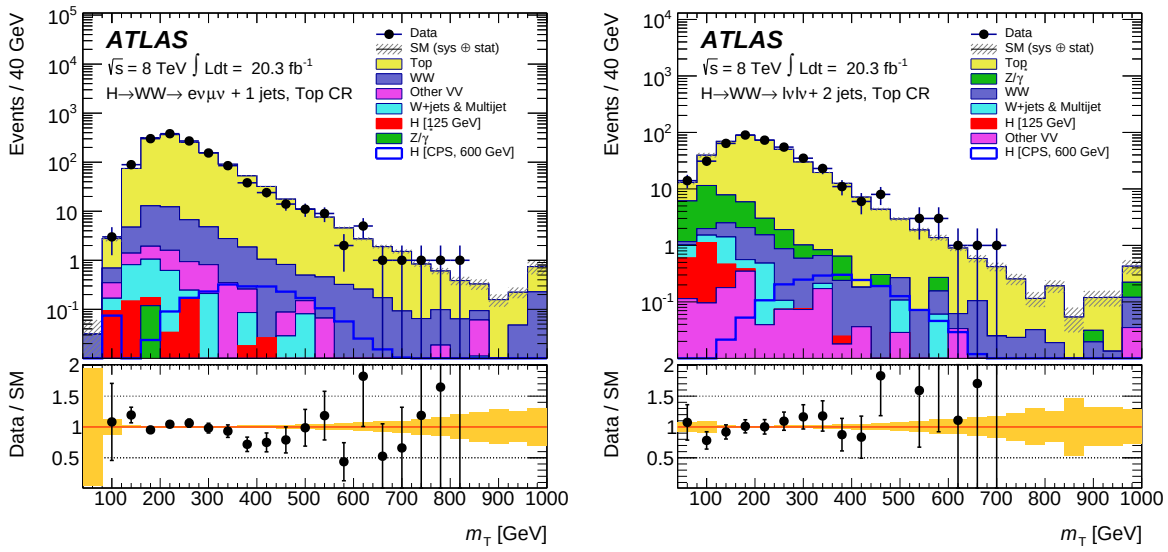

Figure 2: Transverse mass distribution in the $N_{\text{jet}} = 1$ (left) and $N_{\text{jet}} \geq 2$ (right) top control regions of the $H \to WW \to \ell\nu\ell\nu$ analysis. In the $N_{\text{jet}} = 1$ category only the different-flavour final state is used; in the $N_{\text{jet}} \geq 2$ category different-flavour and same-flavour final states are used. In each figure, the last bin contains the overflow. The combined statistical and systematic uncertainties on the prediction are shown by the hatched band in the upper pane and the shaded band in the lower pane. Normalisation factors obtained from a comparison of data and prediction have been applied in these figures.

one b-tagged jet with $p_{\text{T}} > 25\,\text{GeV}$. The purity is 96.5% in the $N_{\text{jet}} = 1$ category and 90.7% in the $N_{\text{jet}} \geq 2$ category. In the $N_{\text{jet}} = 1$ category, only the different-flavour final states are used to obtain the normalisation. In the $N_{\text{jet}} \geq 2$ category same-flavour and different-flavour final states are used to increase the number of events and thereby improve the statistical precision. The normalisation factors obtained from the simultaneous fit to the signal and control regions are 1.05 ± 0.03 for the $N_{\text{jet}} = 1$ CR and 0.92 ± 0.06 for the $N_{\text{jet}} \geq 2$ CR, where the uncertainty quoted includes only the statistical contribution. Figure 2 shows the m_{T} distributions in the $N_{\text{jet}} = 1$ and $N_{\text{jet}} \geq 2$ top CRs. The normalisation factors have been applied in these distributions.

5.2.3 W+jets and multijet background

The procedures to estimate the W+ jets and multijet backgrounds using data are described in more detail in Ref. [83] and summarised here. The W+ jets background contribution is estimated using a control sample of events in which one of the two lepton candidates satisfies the identification and isolation criteria used to define the signal sample (these lepton candidates are denoted "fully identified"), and the other lepton fails to meet these criteria and satisfies a less restrictive selection (denoted "anti-identified"). Events in this sample are otherwise required to satisfy all of the signal selection criteria. The dominant component of this sample (85% to 90%) is W+ jets events in which hadronic activity produces an object reconstructed as an anti-identified lepton. It may be either a non-prompt lepton from the decay of a hadron containing a

heavy quark, or a particle from a jet reconstructed as a lepton candidate.

The W+jets contamination in the SR is determined by scaling the number of events in the control sample by an extrapolation factor, which is measured in a data sample of jets produced in association with Z bosons reconstructed in either the e^+e^- or the $\mu^+\mu^-$ final state. Kinematic vetoes reduce contamination from ZZ and WZ events, and the expected remaining contribution is subtracted. The extrapolation factor is the ratio of the number of fully identified leptons to the number of anti-identified leptons, measured in bins of anti-identified lepton p_{T} and η. To account for differences between the jets associated with W and Z boson production, the extrapolation factors are measured in simulated W+jets and Z+jets events, and the ratio of the two extrapolation factors is multiplied by the one measured in the Z+jets data as a correction. The central value of the correction factor is close to unity; differences among Monte Carlo generators for this ratio of about 20% are observed and are taken as a systematic uncertainty.

The background in the SR due to multijets is determined using a control sample that has two anti-identified lepton candidates, but otherwise satisfies all of the SR selection criteria. An extrapolation factor is estimated using a multijet sample in data and applied twice to the control sample. The sample used to determine the extrapolation factor is expected to have a similar sample composition in terms of heavy-flavour jets, light-quark jets and gluon jets as the control sample. Since the presence of one misidentified lepton in a multijet sample can change the sample composition with respect to a multijet sample with no lepton selection imposed, corrections to the extrapolation factor are made that take into account such correlations. These are evaluated using a multijet Monte Carlo sample and range from 1.0 to 4.5 depending on the lepton p_{T} and flavour. The uncertainty on these is 30–50%, with the dominant contribution being from the heavy-quark cross sections.

6 The $H \to WW \to \ell\nu qq$ analysis

In the $H \to WW \to \ell\nu qq$ channel the final state consists of one W boson decaying into a quark-antiquark pair leading to a pair of jets, with the other W boson decaying into a charged lepton and a neutrino ($W \to \ell\nu$, with $\ell = e$ or μ). This channel is particularly sensitive in searching for a Higgs boson with a mass greater than twice the W boson mass since m_H can be reconstructed on an event-by-event basis and used as the discriminant to search for a signal. This event-by-event reconstruction is done using kinematic constraints that provide an estimate of the component of the neutrino momentum along the beam axis and require signal jets in the event to be consistent with coming from a hadronic W decay.

6.1 Event preselection and categorisation

Events are required to have exactly one reconstructed lepton candidate (e or μ) with $p_{\mathrm{T}} > 25\,\mathrm{GeV}$; no additional lepton with $p_{\mathrm{T}} > 15\,\mathrm{GeV}$ is allowed. The selected lepton must match the object that triggered the event. Events in the SR are required to have $E_{\mathrm{T,calo}}^{\mathrm{miss}} > 60\,\mathrm{GeV}$ in order to suppress multijet processes while retaining a high signal efficiency.

Jets are used to distinguish between ggF and VBF production as well as to reconstruct the hadronic W boson decay. Anti-k_t jets are selected with $p_{\mathrm{T}} > 30\,\mathrm{GeV}$ and $|\eta| < 4.5$, and large-R jets are selected with

$p_{\mathrm{T}} > 100\,\mathrm{GeV}$, $|\eta| < 1.2$, and $m_J > 40\,\mathrm{GeV}$, where the J subscript indicates a large-R jet. Both the anti-k_t and large-R jets are required to be separated from the charged lepton by $\Delta R > 0.3$. There is no explicit overlap removal between anti-k_t and large-R jets.

The momentum of W bosons from the Higgs boson decay increases with increasing Higgs boson mass. This feature leads to a progressively smaller opening angle between the jets produced by the W boson decay, making the jets difficult to distinguish using standard jet reconstruction algorithms. To mitigate the resulting loss in signal efficiency, the hadronic W decay may be reconstructed from either two anti-k_t jets or one large-R jet consistent with originating from a W boson decay.

In hadronic W boson decays reconstructed from two anti-k_t jets, the best candidate jet pair is referred to as the "W jets". The two jets with an invariant mass closest to the W boson mass are taken to be the W jets, unless there is more than one jet pair with $|m_{jj} - m_W| < 15\,\mathrm{GeV}$. In that case, the pair having the highest p_{T} is chosen. Categorisation by production mode is done prior to identification of the hadronic W boson, so jets identified as the VBF tagging jets according to the procedure described below are excluded. Hadronic W boson decays are identified using a single large-R jet if there is one with $p_{\mathrm{T}} > 100\,\mathrm{GeV}$ and a mass closer to the W boson mass than the invariant mass of the best dijet pair. In this case, the large-R jet replaces the W jets as the candidate for the hadronically decaying W boson.

Events are classified into two categories designed to distinguish between the ggF and VBF production modes, based on the number of jets in the event and the properties of those jets. In the category designed to be sensitive to the ggF production mode, referred to as the ggF selection, all events are required to have at least two anti-k_t jets or at least one large-R jet, and fail the VBF selection.

In the second category, designed to be sensitive to the VBF production mode, events are required to have at least four anti-k_t jets or at least two anti-k_t jets and one large-R jet. Orthogonality between the ggF and VBF categories is ensured by identifying the two anti-k_t jets j_1 and j_2 with the largest invariant mass, and assigning the event to the VBF (ggF) category if these jets pass (fail) to meet criteria, referred to as the VBF selection, characteristic of the forward jets produced by the VBF process. This VBF tagging jet pair is required to have an invariant mass $m_{j_1,j_2} > 600\,\mathrm{GeV}$, with the leading jet $p_{\mathrm{T}} > 40\,\mathrm{GeV}$, and be well separated in rapidity such that $\Delta y(j_1, j_2) = |y_{j_1} - y_{j_2}| > 3$. If the ratio of the ggF and VBF cross sections is as predicted by the SM, 63% of signal events passing the full VBF preselection are produced via VBF, and 93% of signal events passing the ggF preselection are produced via ggF.

Vetoes, based on the presence of b-jets in the event, reject $t\bar{t}$ background. If both of the W jets are b-tagged, the event is vetoed. If only one of the W jets is b-tagged, the event is kept to maintain signal efficiency since a large fraction of jets from $W \to c\bar{s}$ decays are b-tagged. If any other jet in the event is b-tagged, including the VBF tagging jets, the event is vetoed. If a large-R jet is used to reconstruct the W boson, events with b-tagged jets outside of $\Delta R = 0.4$ from the axis of the large-R jet are vetoed. No flavour tagging is applied to large-R jets.

Further selections are applied to ggF and VBF selected events. In both categories, each of the W jets is required to have $|\eta| < 2.4$ and their invariant mass to be in the range $65\,\mathrm{GeV} \leq m_{jj/J} \leq 96\,\mathrm{GeV}$, that is, close to the W boson mass. Additionally, for hadronic W boson candidates reconstructed from two anti-k_t jets, one of the two W jets is required to have $p_{\mathrm{T}} > 60\,\mathrm{GeV}$ in both ggF and VBF selected events. Further requirements are imposed on the azimuthal separation of reconstructed objects which exploit the

Table 6: Summary of event preselection in the $H \to WW \to \ell\nu qq$ analysis. The "tagging jets" j_1 and j_2 are the pair of anti-k_t jets with the highest invariant mass among all pairs in the event, and j_1 is the higher-p_{T} jet in the pair. The decay topology selection differs between events in which the hadronic W boson candidate is reconstructed as a pair of jets jj or as a single large-R jet J. For the jet-pair topology, the leading jet is denoted j_{lead} and if only a single jet j is referenced, the requirement is applied to both jets.

Object selection	1 isolated charged lepton (e or μ): $p_{\mathrm{T}} > 25\,\mathrm{GeV}$, $\lvert\eta\rvert < 2.4$ $E_{\mathrm{T,calo}}^{\mathrm{miss}} > 60\,\mathrm{GeV}$ jet: $p_{\mathrm{T}} > 30\,\mathrm{GeV}$, $\lvert\eta\rvert < 4.5$ large-R jet: $p_{\mathrm{T}} > 100\,\mathrm{GeV}$, $\lvert\eta\rvert < 1.2$	
VBF selection	(≥ 4 jets) or (≥ 2 jets + ≥ 1 large-R jets) $m_{j_1,j_2} > 600\,\mathrm{GeV}$ $p_{\mathrm{T}}^{j_1} > 40\,\mathrm{GeV}$ $\Delta y(j_1, j_2) > 3.0$	
ggF selection	not VBF tagged and (≥ 2 jets or ≥ 1 large-R jet)	
Further selection, hadronic W boson reconstructed as:	jet pair	large-R jet
Decay topology	$p_{\mathrm{T}}^{j_{\mathrm{lead}}} > 60\,\mathrm{GeV}$ $\Delta\phi(jj) < 2.5$ $\Delta\phi(j, \ell) > 1.0$ $\Delta\phi(j, E_{\mathrm{T,calo}}^{\mathrm{miss}}) > 1.0$ $\Delta\phi(\ell, E_{\mathrm{T,calo}}^{\mathrm{miss}}) < 2.5$	- - $\Delta\phi(J, \ell) > 1.0$ $\Delta\phi(J, E_{\mathrm{T,calo}}^{\mathrm{miss}}) > 1.0$
b-tagging veto events with:	both W candidate jets b-tagged or any other jet b-tagged	b-tagged jet with $\Delta R(j, J) > 0.4$ -
W-mass window	$65\,\mathrm{GeV} \leq m_{jj} \leq 96\,\mathrm{GeV}$	$65\,\mathrm{GeV} \leq m_J \leq 96\,\mathrm{GeV}$

decay topology of signal events to improve the expected sensitivity. A summary of the event preselection is shown in Table 6.

The signal region is subdivided into exclusive categories which separate sources of signal and background. In addition to the ggF and VBF selection which separates the two signal production modes, the signal regions are separated by the flavour of the charged lepton and the sign of its charge. Electrons and muons are affected differently by the multijet background, and the categories with positively-charged leptons have a higher proportion of W+ jets background because of the charge asymmetry of W production in pp collisions.

6.2 WW invariant mass reconstruction

The invariant mass of the WW system is reconstructed from the four-momenta of the two W boson candidates. The reconstructed invariant mass is denoted $m_{\ell\nu jj}$ regardless of whether the hadronic W boson is reconstructed from a jet pair or a large-R jet. The reconstruction of the leptonic W boson decay relies on the charged lepton and neutrino four-momenta. The complete four-vector is measured for the charged lepton, and the $p_{\mathrm{T}}^{\mathrm{miss}}$ provides the transverse components of the neutrino momentum. The neutrino longitudinal momentum p_z^ν is computed using the quadratic equation resulting from the mass constraint $m(\ell\nu) = m(W)$. In the case of two real solutions of this equation, the solution with the smaller $|p_z^\nu|$ is taken. In the case of complex solutions, only the real part of the solution is taken. Based on signal simulation, this procedure has been shown to give the correct p_z^ν solution in 60–70% of events after the preselection, depending on the event category and the Higgs boson mass. The experimental mass resolution of the reconstructed Higgs boson varies from $\sim 30\,\mathrm{GeV}$ for $m_H = 300\,\mathrm{GeV}$ to $\sim 60\,\mathrm{GeV}$ for $m_H = 1\,\mathrm{TeV}$. For $m_H = 420\,\mathrm{GeV}$, the mass resolution is about the same as the width of a SM Higgs boson at that mass, $\sim 36\,\mathrm{GeV}$.

6.3 Signal region selection

The sensitivity to a heavy Higgs boson in the $H \to WW \to \ell\nu qq$ channel is improved by applying event selection in addition to the preselection described in Section 6.1, as a function of the Higgs boson mass hypothesis.

The mass-dependent optimised selection is based on a set of kinematic quantities that discriminate between the signal from a hypothetical CP-even scalar and the background. For the ggF selection, these are the leading jet p_{T}, the subleading jet p_{T}, the large-R jet p_{T}, the lepton p_{T}, $\Delta\phi_{jj}$, $\Delta\phi_{\ell\nu}$ and $E_{\mathrm{T}}^{\mathrm{miss}}$. For the VBF selection, these are $\Delta\phi_{jj}$, $\Delta\phi_{\ell\nu}$ and p_{T} balance, where p_{T} balance is defined as

$$p_{\mathrm{T,balance}} = \frac{\left(\boldsymbol{p}^{\ell} + \boldsymbol{p}^{\nu} + \boldsymbol{p}^{j_3} + \boldsymbol{p}^{j_4}\right)_{\mathrm{T}}}{p_{\mathrm{T}}^{\ell} + p_{\mathrm{T}}^{\nu} + p_{\mathrm{T}}^{j_3} + p_{\mathrm{T}}^{j_4}} \tag{4}$$

with j_3 and j_4 representing the W-jets, to distinguish them from the tagging jets j_1 and j_2. In the case of large-R jet events, the terms representing j_3 and j_4 are replaced with a single term p_{T}^J which represents the large-R jet momentum instead. Also, the $\Delta\phi_{jj}$ selection is only applied to events in which two resolved jets form the hadronically decaying W boson. Fewer criteria are used for the VBF selection than the ggF selection because of the smaller event yields in the VBF channel.

The selection is optimised as a function of the Higgs boson mass through a two-step procedure. In the first step, the selection that optimises the expected signal significance are found in 100 GeV increments of the mass hypothesis m_H. The expected signal significance is defined as $s/\sqrt{s+b}$, where s is the number of expected signal events and b is the number of expected background events. Other estimators for the significance have been tested ($s/\sqrt{b}$ and $s/\sqrt{b+\Delta b}$ with $\Delta b = 10\%$ and 30%) and shown to provide the same optimal selection. Since the majority of signal events are localised to a region in $m_{\ell\nu jj}$ that is small compared with the overall fit region, the significance calculation does not include all signal and background events, but rather only events in which $m_{\ell\nu jj}$ is within a specified range around m_H, defined

as the region that contains 90% of the signal events. The resulting selection criteria become stricter with increasing m_H as the decay products are produced at higher momenta, allowing greater background rejection while maintaining good signal efficiency.

In the second step, the selection is slightly relaxed, because the optimal selection, particularly for low m_H, typically causes the peak of the signal $m_{\ell\nu jj}$ distribution to coincide with that of the expected background, thus reducing the sensitivity of the analysis because of large systematic uncertainties in describing the turn-over region in $m_{\ell\nu jj}$. Typically, the optimal value for the next lower m_H increment is used.

6.4 Background estimation

In all signal regions, the background is expected to be dominated by W+jets production, with other important contributions from $t\bar{t}$, single top, and multijet production that can be selected owing to the presence of leptons from heavy-flavour decays or jets misidentified as leptons. Diboson events, including WW, WZ, ZZ, $W\gamma$, and $Z\gamma$, as well as Z+jets events, contribute at a smaller level and are also accounted for as backgrounds.

The W+ jets and top-quark backgrounds are modelled using simulation but their normalisations (one for W+jets and one for top-quark backgrounds) are determined through a simultaneous fit to the signal and control regions, similarly to what is done for the $\ell\nu\ell\nu$ final state. The profile likelihood fit is described in more detail in Section 9.1. Multijet backgrounds are estimated using a CR selected in data to be enriched in leptons produced by hadronic activity. The small additional background from Z+ jets and dibosons, including $Z\gamma$ and $W\gamma$, are estimated using their theoretical cross sections with simulation for the event selection acceptance and efficiency.

6.4.1 W+jets and top-quark background

W+jets and top-quark production are the most important backgrounds in the $H \to WW \to \ell\nu qq$ analysis. Their normalisations are set, and the $m_{\ell\nu jj}$ shape corrected, using the data observed in the corresponding CRs, defined below.

The W control region (WCR) is defined similarly to the SR, but with the signal contributions suppressed by rejecting events with a dijet mass, or a large-R jet mass, consistent with the hadronic decay of a W boson. The WCR for the ggF selection is defined by the upper and lower sidebands to the reconstructed W boson mass,

$$52\,\text{GeV} < m_{jj} < 65\ \text{GeV},\ \text{ggF lower sideband} \tag{5}$$

$$96\,\text{GeV} < m_{jj} < 126\ \text{GeV},\ \text{ggF upper sideband} \tag{6}$$

using the dijet or large-R jet mass closest to the W mass, as described in Section 6.1. The corresponding sidebands in the WCR for the VBF selection are

$$43\,\text{GeV} < m_{jj} < 65\ \text{GeV},\ \text{VBF lower sideband} \tag{7}$$

$$96\,\text{GeV} < m_{jj} < 200\ \text{GeV},\ \text{VBF upper sideband.} \tag{8}$$

The width of the sidebands is increased in the VBF selection compared to the ggF selection to improve the statistical precision of the background estimate. For both the ggF and VBF selection, the number of background events is similar in the upper and lower sidebands, so no statistical bias is generated by using them jointly to define a common background normalisation. Separate CRs are defined for the ggF and VBF selection, but all lepton flavours and charges as well as the large-R and dijet W reconstruction topologies are merged into a single CR. The CR selection also follows the mass-dependent SR selection described in Section 6.3. The purity of the WCR depends on the particular selection, but varies between about 70% and over 80%, with higher purities for higher m_H selection and for ggF compared to VBF. The W+ jets normalisation factors are consistent with unity and stable with respect to the m_H-dependent selection and ggF vs. VBF selection. The normalisation factors resulting from the simultaneous fit to the signal and control regions range from 0.9 ± 0.1 to 1.3 ± 0.3. The quoted uncertainties include statistical and experimental systematic components. The highest values are found with the VBF and high-m_H selection.

Figure 3 shows the $m_{\ell\nu jj}$ distributions observed in the ggF and VBF WCRs. Non-W-boson contributions are subtracted from the data, and the resulting distribution is compared to the prediction from simulated W+ jets events, after normalising the prediction to the data. The observed distributions differ substantially from those predicted in both the ggF and VBF WCRs. An alternative MC sample, generated using Alpgen + Pythia6, results in better agreement with the data in the WCR, but does not have enough events for a statistically precise prediction in the signal region for large values of m_H.

To correct the observed mismodelling, simulated W+ jets events are reweighted using the $m_{\ell\nu jj}$ distribution observed in the WCR. In order to obtain a smooth function to use for the reweighting, the ratio of the data to the prediction is fit with polynomial functions. The degree of the polynomial is chosen to have enough flexibility to yield a good fit quality, the fit range being restricted to $m_{\ell\nu jj}$ values where a statistically meaningful fit can be made. For the ggF WCR, shown on the left side of Figure 3, a second-order polynomial function is used and the fit is extended to $m_{\ell\nu jj} = 1.7$ TeV. Above that value of $m_{\ell\nu jj}$, a constant function at the value of the polynomial at $m_{\ell\nu jj} = 1.7$ TeV is used. For the VBF WCR, shown on the right side of Figure 3, a third-order polynomial function is used, up to $m_{\ell\nu jj} = 0.9$ TeV. Fits extending to higher values of $m_{\ell\nu jj}$ have been attempted but require either a more complex fitting function or have a visibly poor-quality fit to the data. For simplicity, a constant function is used for $m_{\ell\nu jj} > 0.9$ TeV, as illustrated in the figure. The value of the function is the value of the third-order polynomial at $m_{\ell\nu jj} = 0.9$ TeV.

The top-quark control region (TopCR) is designed to be as pure as achievable for the second largest background, $t\bar{t} \to WbWb \to \ell\nu jj + bb$. The event topology of this background is similar to that of the Higgs boson signal, but contains two characteristic b-jets. The TopCR is defined to be identical to the SR, but with the b-jet veto reversed. As with the WCR, the TopCR region selection follows the mass-dependent signal region selection described in Section 6.3, and lepton flavours and hadronic W topologies are merged but separate TopCRs are defined for the ggF and VBF topologies. The purity of the TopCR is about 80% and does not depend strongly on the region-specific selection. Similarly, the value of the resulting normalisation factor is stable with respect to the kinematic selection and is consistent with unity within the uncertainties. The values of the normalisation factor found by the simultaneous fit to the signal and control regions range from 0.9 ± 0.1 to 1.3 ± 0.2. Both extremes occur in the VBF control region for m_H-dependent selection for $m_H \geq 700$ GeV, which is most subject to statistical fluctuations.

The $m_{\ell\nu jj}$ distributions in the ggF and VBF TopCRs are shown in Figure 4. As in Figure 3, processes other than top-quark single and pair production are subtracted from the data, and the resulting distribution

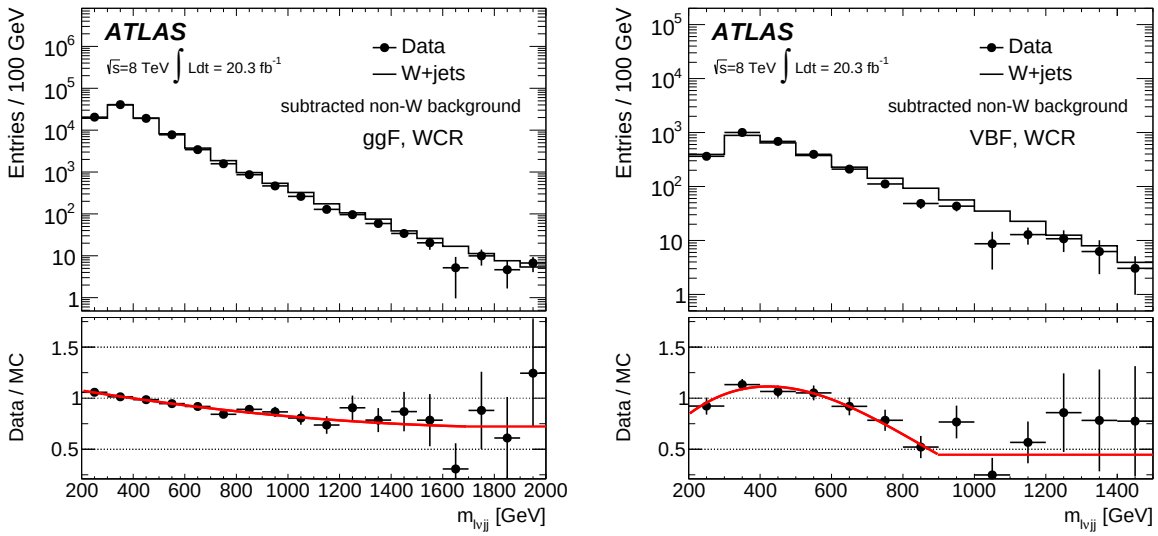

Figure 3: Data and Monte Carlo comparison of the shape of the invariant mass of the WW system $m_{\ell\nu jj}$ in the ggF (left) and VBF (right) WCRs after the $m_H = 300\,\text{GeV}$ selection for the $H \to WW \to \ell\nu qq$ analysis. All the lepton flavour and charge categories are summed together. To isolate the effects of W+jets background modelling, other contributions (top, diboson, Z+ jets, multijet) are subtracted from the data. The Monte Carlo distributions are normalised to the remaining data. The ratio of the data to the Monte Carlo distribution is shown in the bottom panel, along with a red line showing the resulting weights that are applied to correct the Monte Carlo predictions in the rest of the analysis.

is compared to the top-quark prediction after normalising the prediction to the data. Similarly to the WCR, differences in shape are observed, and simulated top-quark events are reweighted accordingly as a function of $m_{\ell\nu jj}$. A first-order polynomial function is fit to the data. Since the purity of events with a top quark in the TopCR is very high, the W+jets contribution in Figure 4 has no $m_{\ell\nu jj}$ reweighting applied.

For both the W+ jets and top-quark backgrounds, the event weights used to correct the MC simulated events are derived from corresponding CRs after the $m_H = 300\,\text{GeV}$ selection, because this is the most inclusive selection. The higher-mass criteria select subsets of the events accepted by the 300 GeV selection. The agreement between the data and MC distributions in the W and top-quark CRs when other mass-dependent selection criteria are applied is consistent with the results from the 300 GeV selection. The reweighting is event-by-event, using the fitted functions shown in Figures 3 and 4 and the $m_{\ell\nu jj}$ value of each simulated W+jets or top-quark background event. The reweighting is applied after the preselection, and therefore propagates to all signal and control regions. For events with $m_{\ell\nu jj}$ above the fitted range, the weight at the upper boundary of the fit is used.

Half of the difference between the nominal and the reweighted $m_{\ell\nu jj}$ distribution is taken as a systematic uncertainty on the $m_{\ell\nu jj}$ shape of these backgrounds. These uncertainties are included as Gaussian constraints in the profile likelihood fit, which allows the fit to adjust the shape of these backgrounds using the shape of the data in the signal regions.

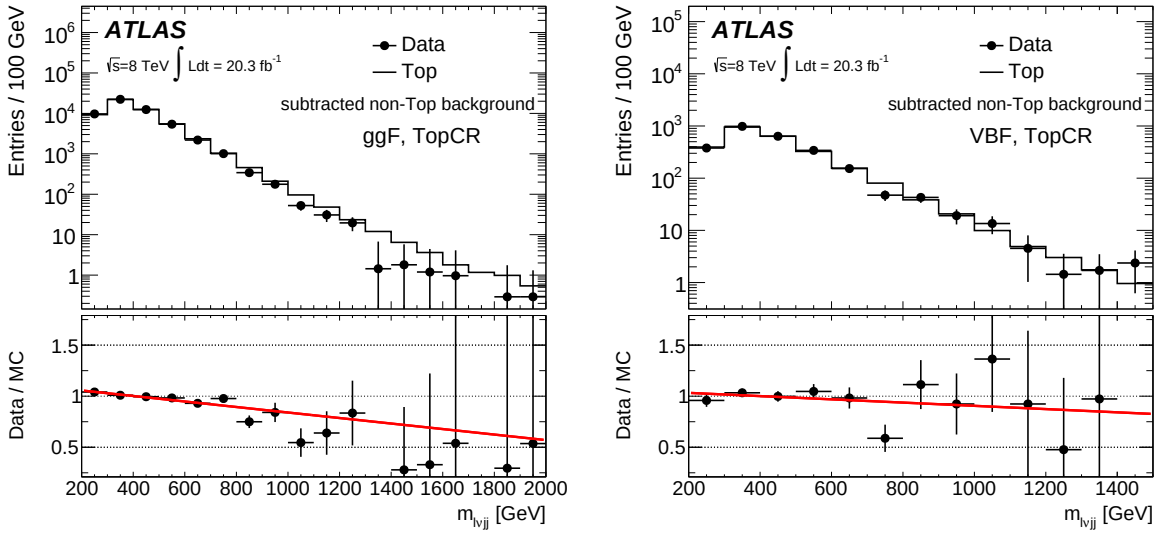

Figure 4: Data and Monte Carlo comparison of the shape of the invariant mass of the WW system $m_{\ell\nu jj}$ in the ggF (left) and VBF (right) TopCRs after the $m_H = 300\,\text{GeV}$ selection for the $H \to WW \to \ell\nu qq$ analysis. All the lepton flavour and charge categories are summed together. To isolate the effects of top-quark background modelling, other contributions (W+ jets, diboson, Z+ jets, multijet) are subtracted from the data. The Monte Carlo distributions are normalised to the remaining data. The ratio of the data to the Monte Carlo distribution is shown in the bottom panel, along with a red line showing the resulting weights that are applied to correct the Monte Carlo predictions in the rest of the analysis.

6.4.2 Multijet background

The shapes of multijet background distributions are modelled using histograms derived from data samples selected similarly as for signal events, except that the lepton identification requirements are loosened, while the isolation requirement is not changed. In the electron channels, a loosened identification selection is applied to the data, with a veto for electrons selected using the standard criteria. In the muon channels, the impact parameter significance requirement is reversed.

The normalisation of the multijet background in a given event category is derived from a standalone template fit (separate from the final simultaneous fit) to the $E_{\text{T}}^{\text{miss}}$ distribution without the $E_{\text{T}}^{\text{miss}}$ requirement applied. The template for the multijet background in each region is taken from data selected with modified lepton selection as described above, but otherwise following the event selection of that signal or control region. The relative contributions of backgrounds other than the multijet background are fixed to their SM expectations.

The multijet background is relatively small, constituting between 1% and 4% of the total expected background depending on the selection used, with smaller contributions for the mass-dependent SR selection applied at higher values of m_H. This background is also concentrated at low values of $m_{\ell\nu jj}$, so its effect is reduced by the $m_{\ell\nu jj}$ shape fit.

7 Systematic uncertainties

This section describes the systematic uncertainties affecting the analysis results. Experimental and theoretical uncertainties common to the $H \to WW \to \ell\nu\ell\nu$ and $H \to WW \to \ell\nu qq$ analyses are described first, followed by a discussion of uncertainties particular to each channel.

7.1 Common experimental uncertainties

The dominant sources of experimental uncertainties on the signal and background yields are the jet energy scale and resolution, and the b-tagging efficiency. Other sources of uncertainty include those on the scale and resolution of the lepton energy or momentum, lepton identification and trigger efficiencies, the scale and resolution of the missing transverse momentum, and the luminosity calibration. All experimental uncertainties are treated by varying the object subject to a particular uncertainty and then re-running the full analysis.

The jet energy scale is determined from a combination of test-beam data, simulation, and *in situ* measurements [27]. Its uncertainty is split into several independent categories: modelling and statistical uncertainties on the extrapolation of the jet calibration from the central region (η intercalibration), high-p_{T} jet behaviour, Monte Carlo non-closure uncertainties, uncertainties on the jet quark and gluon compositions and their calibrations, the b-jet energy scale uncertainties, uncertainties due to modelling of in-time and out-of-time pile-up, and uncertainties on *in situ* jet energy corrections. Some of these categories are further subdivided by the physical source of the uncertainty. For the anti-k_t jets used in these analyses, the jet energy scale uncertainty ranges from 1% to 7% depending on p_{T} and η. The resolution varies from 5% to 20%, and the relative uncertainty on the resolution ranges from 2% to 40%. The lowest-p_{T} jets, immediately above the jet selection thresholds, have both the poorest resolution and the largest uncertainty.

The evaluation of the b-jet tagging efficiency uses a sample dominated by dileptonic decays of top-quark pairs [34]. To improve the precision, this method is combined with a second calibration method based on samples containing muons reconstructed in the vicinity of the jet. The uncertainties related to b-jet identification are decomposed into six uncorrelated components using an eigenvector method [33], the number of components being equal to the number of p_{T} bins used in the calibration. The uncertainties range from $< 1\%$ to 7.8%. The uncertainties on the misidentification rate for light-quark jets depend on p_{T} and η, with a range of 9%–19%. The uncertainties on c-jets reconstructed as b-jets range between 6%–14% depending on the jet p_{T}.

The reconstruction, identification, isolation, and trigger efficiencies for electrons and muons, as well as their momentum scales and resolutions, are estimated using $Z \to ee, \mu\mu$, $J/\psi \to ee, \mu\mu$, and $W \to e\nu, \mu\nu$ decays [22, 23, 25]. The uncertainties on the lepton identification and trigger efficiencies are smaller than 1% except for the uncertainty on the electron identification efficiency, which varies between 0.2% and 2.7% depending on p_{T} and η.

The changes in jet energy and lepton momenta due to systematic variations are propagated to $E_{\mathrm{T}}^{\mathrm{miss}}$, such that changes in the high-p_{T} object momenta and in $E_{\mathrm{T}}^{\mathrm{miss}}$ are fully correlated. Additional contributions to

the $E_{\mathrm{T}}^{\mathrm{miss}}$ uncertainty arise from the modelling of low-energy particle measurements ("soft terms") [35]. Calorimeter measurements of these particles, used in $E_{\mathrm{T,calo}}^{\mathrm{miss}}$, use calibrated clusters of cells not associated with reconstructed physics objects, with a noise threshold applied. The longitudinal and perpendicular components of the soft terms, defined with respect to the $E_{\mathrm{T}}^{\mathrm{miss}}$ computed using hard objects, are smeared and rescaled to evaluate the associated uncertainties. The uncertainties are parameterised as a function of the magnitude of the vector sum $\vec{p_{\mathrm{T}}}$ of the high-p_{T} objects, and are evaluated in bins of the average number of interactions per bunch crossing. Differences of the mean and width of the soft term components between data and simulation result in variations on the mean of the longitudinal component of about 0.2 GeV. The uncertainty on the resolution of the longitudinal and perpendicular components is 2% on average. The systematic uncertainties related to the track-based soft term for $p_{\mathrm{T}}^{\mathrm{miss}}$ are calculated by comparing the properties of $p_{\mathrm{T}}^{\mathrm{miss}}$ in $Z \rightarrow ee, \mu\mu$ events in data and simulation as a function of the magnitude of the summed $\vec{p_{\mathrm{T}}}$ of the leptons and jets in the event. The variations on the mean of the longitudinal component are in the range 0.3–1.4 GeV and the uncertainties on the resolution on the longitudinal and perpendicular components are in the range 1.5–3.3 GeV, where the lower and upper bounds correspond to the range of the sum of the hard p_{T} objects below 5 GeV and above 50 GeV, respectively.

The uncertainty on the integrated luminosity is 2.8%. It is derived following the same methodology as in Ref. [86] from a calibration of the luminosity scale derived from beam-separation scans.

7.2 Common theoretical uncertainties

Theoretical uncertainties on the signal production cross section affect the $H \rightarrow WW \rightarrow \ell\nu\ell\nu$ and $H \rightarrow WW \rightarrow \ell\nu qq$ analyses in the same way. These include uncertainties due to the choice of QCD renormalisation and factorisation scales, the PDF model used to evaluate the cross section and acceptance, and the underlying event and parton shower models. These are described and evaluated as a function of m_H in Refs. [87, 88]. The QCD scale uncertainty on the inclusive signal cross sections is evaluated to be 8% for ggF and 1% for VBF production. The PDF uncertainty on the inclusive cross sections is 8% for ggF and 4% for VBF production. Uncertainties on the interference weighting of the CPS signal samples, described in Section 4, are also included.

7.3 Uncertainties specific to the $H \rightarrow WW \rightarrow \ell\nu\ell\nu$ analysis

The uncertainties specific to the $H \rightarrow WW \rightarrow \ell\nu\ell\nu$ analysis arise primarily from the theoretical modelling of the signal acceptance in jet bins, the theoretical models used in the background predictions, and the additional consideration of uncertainties on the m_{T} shape used in the likelihood fit. Statistical uncertainties on yields in control regions, and the effect of subtracting other processes from the control region yield, are also included in the total uncertainty on background yields predicted using control regions.

Since the analysis is binned by jet multiplicity, large uncertainties from variations of QCD renormalisation and factorisation scales affect the predicted contribution of the ggF signal in the exclusive jet bins, and can cause event migration among bins. These uncertainties are estimated using the HNNLO program [79, 89] and the method reported in Ref. [90] for Higgs boson masses up to 1500 GeV. The sum in quadrature of

the inclusive jet bin uncertainties amounts to 38% in the 0-jet category and 42% in the 1-jet category for $m_H = 600$ GeV. For $m_H = 1$ TeV, these uncertainties are 55% and 46%, respectively.

For the backgrounds normalised using control regions, theoretical uncertainties arise from the use of simulations of the background used in the extrapolation from the control region to the signal region. For the WW background in the $N_{\text{jet}} \leq 1$ categories and the top-quark background in the $N_{\text{jet}} = 1$ and $N_{\text{jet}} \geq 2$ jet categories, theoretical uncertainties on the extrapolation are evaluated according to the prescription of Ref. [88]. The uncertainties include the impact of missing higher-order QCD corrections, PDF variations and MC modelling. For backgrounds normalised to the theoretical prediction without use of a control region, a similar prescription is followed for the acceptance uncertainty, and uncertainties on the predicted inclusive cross section also apply.

For the WW background, the uncertainties on the control region extrapolation in the 0- and 1-jet categories amount to 4.2% and 9.7%, respectively. In the ≥ 2 jet category, the WW yield is taken from the theoretical expectation. The PDF uncertainty on the cross sections of the $q\bar{q} \to WW + 2$ jets and $gg \to WW + 2$ jets processes is evaluated to be 4% and that on the acceptance of these processes to be 2%. The QCD scale uncertainty on QCD $WW + 2$ jets is 14%, while that on the acceptance is 20%. The modelling uncertainty is derived by comparing samples generated with Sherpa and MadGraph [91] generators. This uncertainty amounts to 34% for QCD $WW + 2$ jets and 7% for EW $WW + 2$ jets after the selection on $m_{\ell\ell}$. In all jet categories, a correction is applied to the WW background to take higher-order EW corrections to the cross section into account. A conservative uncertainty of 100% is applied to this correction.

For the top-quark background estimation in the 0-jet category, a 3.9% theoretical uncertainty is assigned from the use of simulated top-quark events to model the ratio of the signal region jet veto efficiency to the square of the efficiency of the additional-jet veto in the b-tagged control region ($\epsilon_0/(f_0^{\text{MC}})^2$ in Eq. 3). An additional 4.5% theoretical uncertainty is used on the efficiency ϵ_{rest} on the remaining selection that defines the $N_{\text{jet}} = 0$ signal region, which is also derived from simulated top-quark events. The most important component of these uncertainties is the variation among predictions by different MC generator and parton shower algorithms. Smaller uncertainties attributable to the QCD scale choice, PDF model, $t\bar{t}$–Wt interference, and the single-top cross section are also included. For the top-quark background in the 1- and ≥ 2 jet categories, the uncertainties are respectively 5.7% and 9.8%.

The main uncertainty on the W+ jets and multijet background predictions arise from the extrapolation factors relating anti-identified to identified leptons. For W+ jets, a modelling uncertainty on the simulation-based correction applied to the Z+ jets extrapolation factor of about 20% and the statistical uncertainty from the Z+ jets data used to measure the extrapolation factor contribute in roughly equal proportions. The main uncertainty on the multijet contribution arises from an uncertainty on the modelling of the correlation between the extrapolation factors for two anti-identified leptons in the same event.

In the same-flavour channel in the ≥ 2 jet category, the Drell–Yan background is non-negligible. The background is estimated from simulation in this final state as in the other final states, but a 15% theoretical uncertainty is assigned to the cross section of the process using the total relative theoretical uncertainty on the $Z + 2$ jets cross-section prediction in the high-m_{jj} region, following Ref. [92].

In addition to the uncertainties on the normalisation of backgrounds, experimental and theoretical uncertainties on the m_{T} shape model used in the fit are considered. Simulated data are used for the m_{T} shape

for signal and all backgrounds except for W+ jets. Only shape variations which are statistically significant compared to the statistical uncertainty from the simulation model of the shape are included. For the background model, uncertainties due to b-tagging efficiency, lepton identification, trigger, and isolation efficiency scale factors fall into this category, as does the uncertainty on the extrapolation factors for the W+ jets and multijet background estimates. For the ggF signal, the experimental systematic uncertainties from $E_{\mathrm{T}}^{\mathrm{miss}}$ are treated as m_{T} shape uncertainties. The theoretical uncertainty from the interference weighting are also included as a systematic uncertainty on the m_{T} shape for the ggF CPS signal samples.

7.4 Uncertainties specific to the $H \to WW \to \ell\nu qq$ analysis

Uncertainties in the $H \to WW \to \ell\nu qq$ analysis are analogous to those in the $H \to WW \to \ell\nu\ell\nu$ analysis, but different uncertainties are prominent. The absence of exclusive jet binning means that there are no additional theoretical uncertainties on the signal acceptance. Experimental uncertainties, particularly those relating to the modelling of jet energies, are more important.

In addition to the common experimental uncertainties, the $H \to WW \to \ell\nu qq$ results have an uncertainty arising from the energy resolution of large-R jets. This uncertainty is determined by matching reconstructed jets in simulated events with their associated particle-level jets, and computing the ratio of the reconstructed energy (mass) to their true values as determined after parton showering and hadronisation. Previous ATLAS studies of large-R jet energy/mass resolution indicate that the resolution in simulation can vary by up to 20% [93]. Based on these studies, a systematic uncertainty is estimated by smearing the jet energies by a factor corresponding to an increase of 20% in their resolution in bins of p_{T} and $|\eta|$.

The dominant uncertainty on the background modelling in the $H \to WW \to \ell\nu qq$ analysis is that on the shape of the $m_{l\nu jj}$ spectrum for the W+ jets and top-quark backgrounds. This uncertainty is 50% of the difference between the reweighted and nominal $m_{l\nu jj}$ distributions, as described in Section 6.4.1, and is taken as a systematic uncertainty on the shape of the background distribution.

The systematic uncertainty on multijet production is determined by comparing the nominal background estimate with an estimate derived using different lepton selection criteria including a reversed isolation requirement. Uncertainties are derived for different production mechanisms and decay channels as a function of the Higgs boson mass, and vary from about 10% to 100% of the multijet background.

8 Signal and background predictions compared to data

8.1 The $H \to WW \to \ell\nu\ell\nu$ analysis

In Table 7, the expected signal and background in the $H \to WW \to \ell\nu\ell\nu$ analysis are summarized and compared to the number of data events passing the signal region selection. The CPS scenario is used for the signal, and the SM Higgs boson cross section is used to normalise it. For this comparison only, to give an indication of the sensitivity of the shape fit, an m_{T} window is added to the selection. The m_{T} requirements are chosen to be about 80% efficient for the signal, and are: $180\,\mathrm{GeV} < m_{\mathrm{T}} < 270\,\mathrm{GeV}$ for $m_H = 300\,\mathrm{GeV}$, $250\,\mathrm{GeV} < m_{\mathrm{T}} < 500\,\mathrm{GeV}$ for $m_H = 600\,\mathrm{GeV}$, and $300\,\mathrm{GeV} < m_{\mathrm{T}} < 750\,\mathrm{GeV}$ for

Table 7: Summary of the expected signal and background in the $H \to WW \to \ell\nu\ell\nu$ signal regions. The top table compares the observed number of candidate events in data N_{data} with the expected signal N_{sig} for several m_H values and the total background N_{bkg}, along with its statistical ($\sqrt{N_{\text{bkg}}}$) and systematic ($\delta N_{\text{bkg}}^{\text{sys}}$) uncertainties. The predictions are quoted for an m_{T} interval which is about 80% efficient for the signal (details in the text). The different-flavour and same-flavour final states are combined, and in the top table the $N_{\text{jet}} = 0$ and $N_{\text{jet}} = 1$ categories are summed. The bottom table shows the composition of the background for the analysis categories of different jet multiplicity. The VV background category includes all diboson processes except for WW. The $Wj + jj$ column contains the sum of the W+ jets and multijet backgrounds.

	CPS signal expectation			Bkg. expectation	Observed
Category	m_H	$N_{\text{sig}}^{\text{ggF}}$	$N_{\text{sig}}^{\text{VBF}}$	$N_{\text{bkg}} \pm \sqrt{N_{\text{bkg}}} \pm \delta N_{\text{bkg}}^{\text{sys}}$	N_{data}
$N_{\text{jet}} \leq 1$	300 GeV	144	10	$961 \pm 31 \pm 47$	951
	600 GeV	29	3	$584 \pm 24 \pm 12$	538
	900 GeV	5	2	$325 \pm 18 \pm 8$	290
$N_{\text{jet}} \geq 2$	300 GeV	3.1	13.5	$18 \pm 4.2 \pm 5$	20
	600 GeV	0.8	4.2	$9.5 \pm 3.1 \pm 1.9$	15
	900 GeV	0.2	2.3	$5.6 \pm 2.4 \pm 1.5$	10

Category	WW	VV	top quark	$Wj + jj$	Z/γ^*	H[125 GeV]
$N_{\text{jet}} = 0$	54.8%	3.5%	37.3%	2.6%	1.6%	0.1%
$N_{\text{jet}} = 1$	40.7%	3.5%	49.3%	3.4%	2.9%	0.2%
$N_{\text{jet}} \geq 2$	24.6%	2.3%	36.3%	2.5%	30.7%	3.6%

$m_H = 900\,\text{GeV}$. The predicted event yields given do not include adjustments resulting from the fit to data.

The systematic uncertainty on the background is derived from the expected uncertainty on the fit results, by fitting the nominal expected signal and background using the profile likelihood described in Section 9. The total expected uncertainty on the fit result has contributions from the theoretical uncertainties on the signal and background predictions, the experimental uncertainties, and the statistical uncertainties. After removing the signal theoretical uncertainties and the statistical uncertainty in quadrature, the approximate systematic uncertainty on the background, accounting for all systematic correlations among the backgrounds, can be extracted.

The fractional background composition for each N_{jet} category is given in the bottom half of the table. The relative contributions of the various sources to the total background does not vary substantially as a function of m_{T}, so the m_{T} selection described above is not applied.

Figure 5 shows m_{T} distributions in the signal regions, separately for the different- and same-flavour channels and for each jet category. No significant data excess is observed in any final state. The deficit of data events in the high-m_{T} region of the 0-jet different-flavour final state has been investigated and no underlying systematic experimental or modelling effect has been identified. In particular, no correlated kinematic

effects are observed in the data, an alternative WW MC event generator (MC@NLO [94]) does not qualitatively change the level of disagreement, and the m_{T} distribution in the WW control region (Figure 1) does not show a comparable deficit.

8.2 The $H \to WW \to \ell\nu qq$ analysis

In Table 8, the expected signal and background in the $H \to WW \to \ell\nu qq$ analysis are summarized and compared to the number of data events passing the signal region selection. For this comparison only, to give an indication of the sensitivity of the shape fit, a requirement that $m_{\ell\nu jj}$ be close to the mass hypothesis m_H is added to the m_H-dependent signal region selection. The requirement is $|m_{\ell\nu jj} - m_H| < 200\,\mathrm{GeV}$), except for $m_H = 300\,\mathrm{GeV}$, for which the lower bound is 200 GeV, corresponding to the lower $m_{\ell\nu jj}$ considered in the analysis. The systematic uncertainty on the background is derived by fitting the nominal expected signal and background, following the procedure used for the $H \to WW \to \ell\nu\ell\nu$ analysis. The fractional background composition for the ggF and VBF analysis categories and the m_H-dependent selection is shown in the bottom half of the table. The relative contributions of the various sources to the total background do not vary substantially as a function of $m_{\ell\nu jj}$, so the $m_{\ell\nu jj}$ window described above is not applied.

Figure 6 show the $m_{\ell\nu jj}$ distributions and the ratio of data to background expectation for the WCR (top), TopCR (middle), and SR (bottom) after the ggF preselection on the left hand side of the figure. Shown on the right are the corresponding distributions for the VBF preselection. These distributions do not include the background normalisations applied by the fit to the control regions, but the $m_{\ell\nu jj}$ reweighting described in Section 6.4.1 is applied.

The Higgs boson signal yield in each final state is determined using a binned maximum likelihood fit to the observed $m_{\ell\nu jj}$ distribution in the range $200\,\mathrm{GeV} < m_{\ell\nu jj} < 2000\,\mathrm{GeV}$. For the $m_H = 500\,\mathrm{GeV}$ selection, the control and signal regions distributions are shown in Figure 7. In these distributions, the $m_{\ell\nu jj}$ reweighting is applied and the background normalisations are corrected using the results of the fit to the signal and control regions. There is no indication of a significant excess of data above the background expectation. A slight deficit can be seen in the VBF channel in the centre and lower panels of Figure 6 but its effect is mitigated by the mass-dependent selection.

9 Results and Interpretations

9.1 Statistical methodology

The methodology used to derive statistical results is described in detail in Ref. [95]. A likelihood function $\mathcal{L}$ is defined using the distributions of the discriminant for events in the signal region of each analysis category, namely, the 0-, 1- and $\geq$ 2-jet categories in the $H \to WW \to \ell\nu\ell\nu$ analysis and the ggF and VBF categories in the $H \to WW \to \ell\nu qq$ analysis. The likelihood is a product of Poisson functions over the bins of the discriminant in the signal regions and ones describing the total yield in each control region. Each systematic uncertainty is parameterised by a corresponding nuisance parameter θ modelled by a

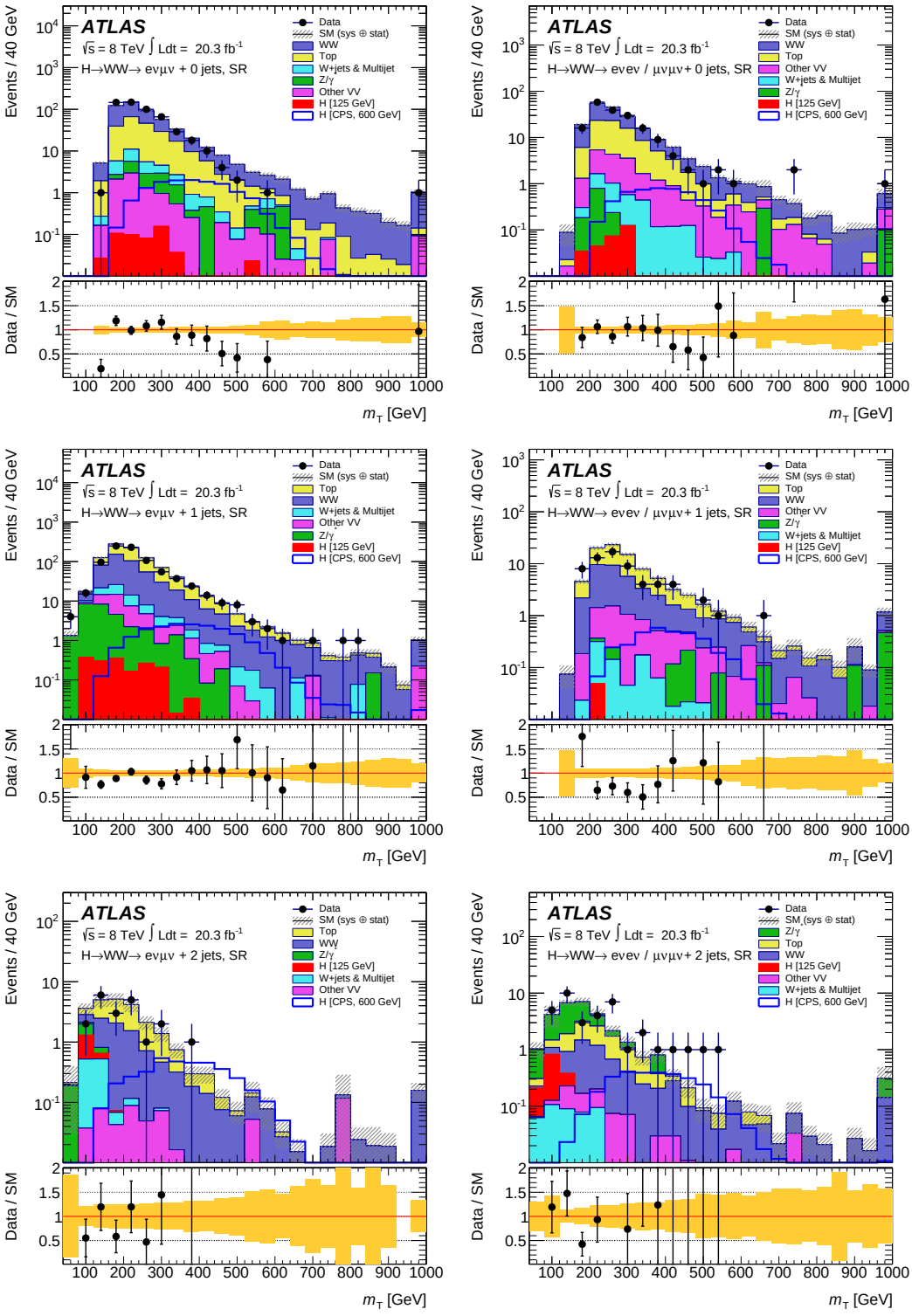

Figure 5: Transverse mass distributions in the 0-jet (top), 1-jet (middle) and ≥ 2 jet (bottom) categories in the $H \to WW \to \ell\nu\ell\nu$ signal regions. Different-flavour (left) and same-flavour (right) final states are shown. The histograms for the background processes, including the observed $H[125\,\text{GeV}]$, are shown stacked, and the distribution for a hypothetical CPS signal process with $m_H = 600\,\text{GeV}$ and the cross section predicted by the SM for that mass is overlaid. The combined statistical and systematic uncertainties on the prediction are shown by the hatched band in the upper pane and the shaded band in the lower pane. In each figure, the last bin contains the overflow.

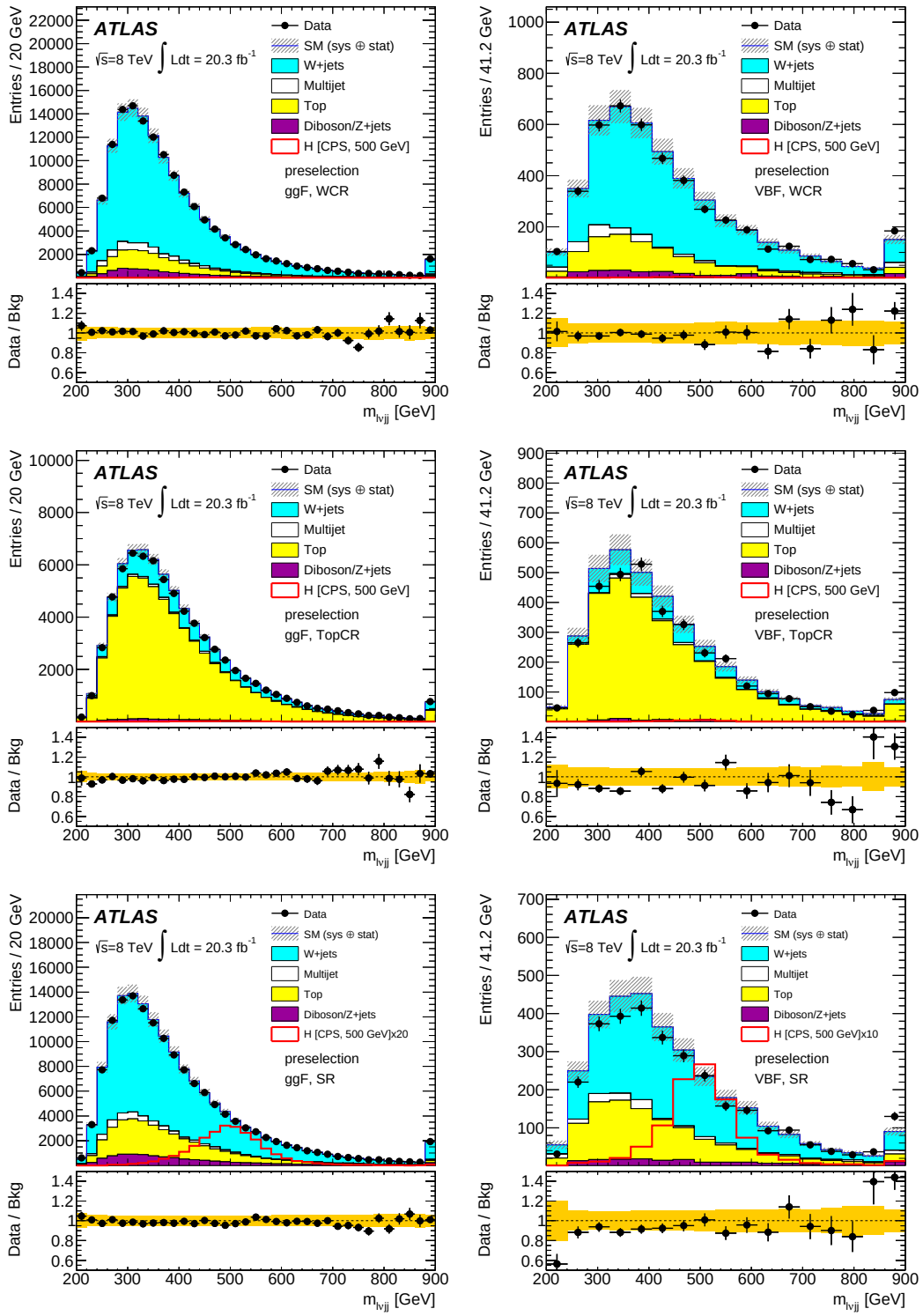

Figure 6: Distributions of the invariant mass $m_{\ell\nu jj}$ of the WW system and the ratio of data to background expectation for the WCR (top), TopCR (middle), and SR (bottom) after the ggF preselection (left) and the VBF preselection (right) for the $H \to WW \to \ell\nu qq$ analysis. The histograms for the background processes are shown stacked, and the distribution for a hypothetical CPS signal process with $m_H = 500\,\text{GeV}$ and the cross section predicted by the SM for that mass is overlaid. All the flavour and charge categories are summed in each plot. No normalisation scale factors are applied to the top-quark or W background samples. The combined statistical and systematic uncertainties on the prediction are shown by the hatched band in the upper pane and the shaded band in the lower pane. In each figure, the last bin contains the overflow.

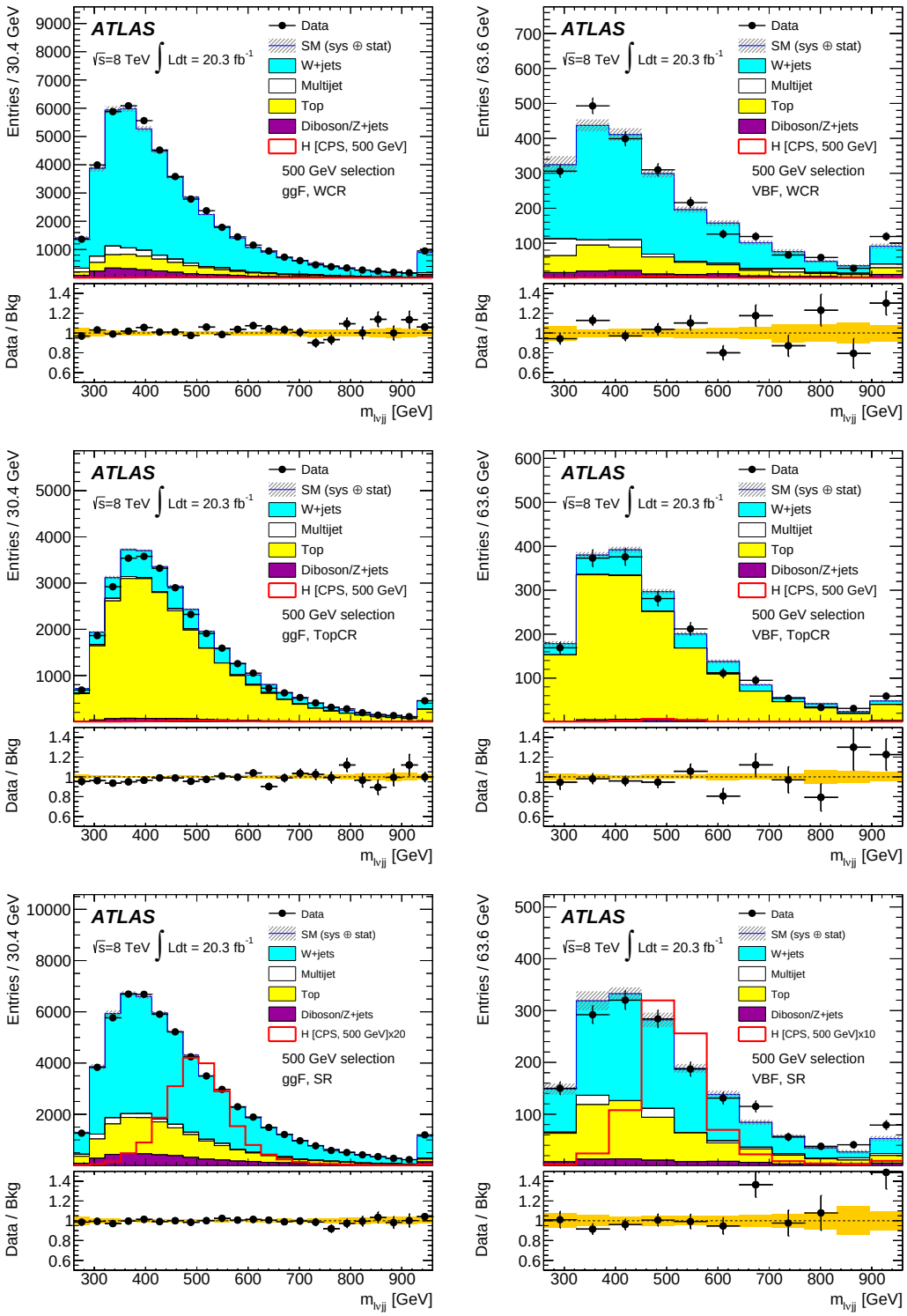

Figure 7: Distributions of the invariant mass $m_{\ell\nu jj}$ of the WW system and the ratio of data to background expectation for the WCR (top), TopCR (middle), and SR (bottom) after the ggF 500 GeV selection (left) and the VBF 500 GeV selection (right) in the $H \to WW \to \ell\nu qq$ analysis. These plots are after fitting for the $m_H = 500\,\text{GeV}$ hypothesis, and the binning used is identical to the binning used in the fit. The histograms for the background processes are shown stacked, and the distribution for a hypothetical CPS signal process with $m_H = 500\,\text{GeV}$ and the cross section predicted by the SM for that mass is overlaid. All the flavour and charge categories are summed in each plot. The combined statistical and systematic uncertainties on the prediction are shown by the hatched band in the upper pane and the shaded band in the lower pane. In each figure, the last bin contains the overflow.

Table 8: Summary of the expected signal and background in the $H \to WW \to \ell\nu qq$ signal regions. The top table compares the observed number of candidate events in data N_{data} with the expected total signal, N_{sig}, for several m_H values and the total background N_{bkg}, along with its statistical ($\sqrt{N_{\text{bkg}}}$) and systematic ($\delta N_{\text{bkg}}^{\text{sys}}$) uncertainties. The predictions are quoted for an $m_{\ell\nu jj}$ interval around the m_H hypothesis (details in the text). The bottom table shows the composition of the background for the ggF and VBF analysis categories at several m_H hypotheses. The "other" column contains the Z+ jets and diboson backgrounds.

	CPS signal expectation			Bkg. expectation	Observed
Category	m_H	$N_{\text{sig}}^{\text{ggF}}$	$N_{\text{sig}}^{\text{VBF}}$	$N_{\text{bkg}} \pm \sqrt{N_{\text{bkg}}} \pm \delta N_{\text{bkg}}$	N_{data}
ggF	300 GeV	1320	100	112890 ± 340 ± 460	111199
	600 GeV	440	40	23680 ± 150 ± 131	23397
	900 GeV	40	10	1940 ± 40 ± 56	1754
VBF	300 GeV	24	41	2282 ± 48 ± 33	2090
	600 GeV	24	34	850 ± 29 ± 19	829
	900 GeV	3	11	52 ± 7 ± 7	68

Category	m_H	W+ jets	top	multijet	other
ggF	300 GeV	70%	20%	3%	7%
	600 GeV	71%	19%	2%	7%
	900 GeV	73%	14%	3%	10%
VBF	300 GeV	58%	33%	5%	4%
	600 GeV	61%	27%	6%	5%
	900 GeV	52%	32%	4%	12%

Gaussian function (the set of all such nuisance parameters is $\boldsymbol{\theta}$). The modification of affected event yields is implemented as a log-normal distribution parameterised by θ to prevent predicted event yields from taking unphysical values.

In the $H \to WW \to \ell\nu\ell\nu$ analysis, the m_{T} distributions in the signal regions are divided into ten, six and four bins, respectively, for $N_{\text{jet}} = 0$, 1 and ≥ 2. The bins are of variable widths such as to have the same number of expected signal events in each bin. Because the signal is peaked in m_{T} and the background is not, this binning strategy improves the sensitivity by producing bins with different signal-to-background ratios and is robust against statistical fluctuations in the background model.

In the $H \to WW \to \ell\nu qq$ final state, the statistical analysis is performed using a variable fit range and number of bins, adapted to each m_H hypothesis and production mode. The bins are always of equal width, because the $m_{\ell\nu jj}$ distribution for signal peaks more strongly than the signal m_{T} distribution in the $H \to WW \to \ell\nu\ell\nu$ channel, so the discriminant produces bins with sufficiently different signal-to-background ratios without further optimisation. The bin width is chosen to ensure adequate statistical precision for the background predictions. The search is always preformed in a 700 GeV-wide window in

$m_{\ell\nu jj}$, enclosing the resonance peak and as much of the tails as feasible for non-NWA signal models. The range 200–900 GeV is used for the 300 GeV hypothesis, and 500–1200 GeV for the 1000 GeV hypothesis. The ggF (VBF) search uses 35 (17) bins for the 300 GeV hypothesis. The number of bins decreases with increasing m_H, and 12 (6) bins are used for the ggF (VBF) search for $m_H = 1000$ GeV. Mass hypotheses above 1 TeV are also tested, but the binning and fit range for the 1 TeV mass hypothesis are maintained, because there is insufficient data and simulated events to populate the background model at higher values of $m_{\ell\nu jj}$.

Both the $H \to WW \to \ell\nu\ell\nu$ and $H \to WW \to \ell\nu qq$ analyses have signal regions optimised for the VBF and ggF signal production modes, but the presence of both signal processes is accounted for in all signal regions. Limits are obtained separately for ggF and VBF production in all interpretations. To derive the expected limits on the ggF production mode, the VBF production cross section is set to zero, so that the expected limits correspond to the background-only hypothesis. To derive the observed limits on the ggF (VBF) production mode, the VBF (ggF) production cross section is treated as a nuisance parameter in the fit and profiled using a flat prior, as is used for the normalisation of backgrounds using CRs. This approach avoids making any assumption on the presence or absence of the signal in other production modes, by using the signal regions themselves to set the normalisation of the production mode not being tested.

The modified frequentist method known as CL_s, combined with the asymptotic approximation, is used to compute 95% CL upper limits [96, 97]. The method uses a test statistic q_μ, a function of the signal strength μ which is defined as the ratio of the measured $\sigma_H \times \mathrm{BR}(H \to WW)$ to that predicted.[3] The test statistic is defined as:

$$q_\mu = -2\ln(\mathcal{L}(\mu;\hat{\hat{\boldsymbol{\theta}}}_\mu)/\mathcal{L}(\hat{\mu};\hat{\boldsymbol{\theta}})) \tag{9}$$

The denominator does not depend on μ. The quantities $\hat{\mu}$ and $\hat{\boldsymbol{\theta}}$ are the values of μ and $\boldsymbol{\theta}$, respectively, that unconditionally maximise $\mathcal{L}$. The numerator depends on the values $\hat{\hat{\boldsymbol{\theta}}}_\mu$ that maximise $\mathcal{L}$ for a given value of μ.

9.2 Upper limits from the $H \to WW \to \ell\nu\ell\nu$ analysis

Figure 8 shows the 95% CL upper limits on $\sigma_H \times \mathrm{BR}(H \to WW)$ as a function of m_H for a Higgs boson in the CPS scenario, separately for ggF and VBF production, in the mass range 220 GeV $\leq m_H \leq$ 1000 GeV. Figure 9 shows the upper limits on a Higgs boson with a narrow width in the range 300 GeV $\leq m_H \leq$ 1500 GeV, separately for ggF and VBF production. Below 300 GeV, the limits in the NWA scenario are expected to be similar to the CPS scenario, as the width is small enough in the latter case to have a negligible effect.

The systematic uncertainties with the largest effect on the observed limits at $m_H = 300$ GeV, in approximate order of importance, are those related to the modelling of the WW background, the b-jet tagging efficiency, the jet energy scale and resolution, the top-quark background modelling in the $N_{\mathrm{jet}} = 0$ category, the QCD scale uncertainties on the signal from the exclusive jet multiplicity categories, and the jet energy scale and resolution. As the mass hypothesis increases, the experimental systematic uncertainties

[3] The SM cross-section prediction is used to define μ for the NWA and intermediate-width scenarios.

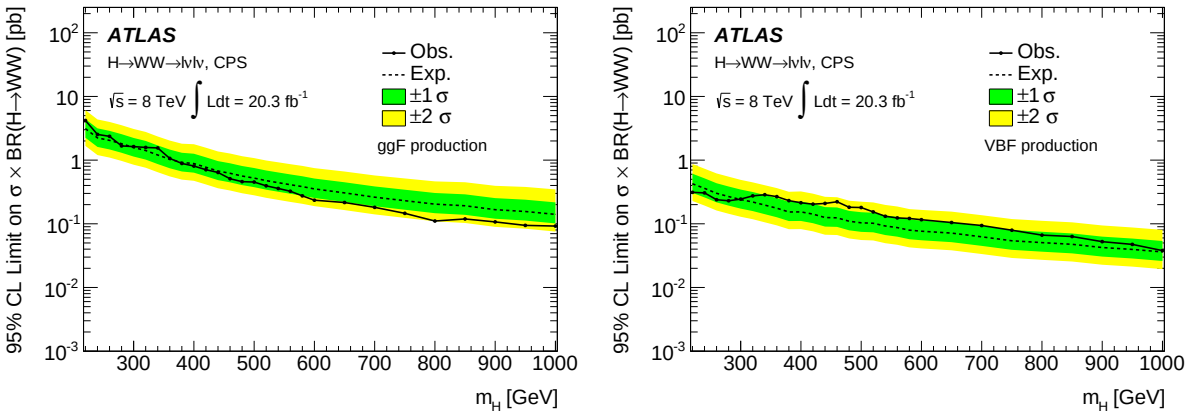

Figure 8: 95% CL upper limits on $\sigma_H \times \mathrm{BR}(H \to WW)$ from the $H \to WW \to \ell\nu\ell\nu$ analysis for the CPS scenario. Limits for ggF production (left) and VBF production (right) are shown. The green and yellow bands show the $\pm 1\sigma$ and $\pm 2\sigma$ uncertainties on the expected limit.

diminish in relative importance and the leading sources of uncertainty are on the signal cross section in exclusive N_{jet} categories and the WW background model. Also, for the CPS scenario, the uncertainty on the interference weighting becomes important at high m_H.

The relative importance of systematic and statistical uncertainties for the analysis can be illustrated by recalculating the limits with the systematic uncertainties omitted. For the CPS scenario, the ggF limits decrease by about 20% for $m_H = 300\,\mathrm{GeV}$ and by about 10% for $m_H = 1000\,\mathrm{GeV}$. For high mass hypotheses, higher values of m_{T}, where there are fewer events, are implicitly tested. Similarly, there are fewer candidates in the $N_{\mathrm{jet}} \geq 2$ category, so that the limits are less sensitive to systematic uncertainties than the corresponding ggF limits. For the CPS VBF limit, removing the systematic uncertainties has about an 8% effect on the observed limit at $m_H = 300\,\mathrm{GeV}$ and a negligible effect at $m_H = 1000\,\mathrm{GeV}$.

The deficit at $m_{\mathrm{T}} \gtrsim 450\,\mathrm{GeV}$ observed in Figure 5 results in a stronger limit than that predicted for background-only in the ggF production mode in both signal models, although they are consistent within the given uncertainties. For signal, the relation $m_{\mathrm{T}} \lesssim m_H$ holds, so the observed limits are stronger than the expected ones above this threshold of about 450 GeV.

9.3 Upper limits from the $H \to WW \to \ell\nu qq$ analysis

Limits are derived following the same procedure as for the $H \to WW \to \ell\nu\ell\nu$ channel. Figure 10 shows the 95% CL upper limits on $\sigma_H \times \mathrm{BR}(H \to WW)$ as a function of m_H for the CPS scenario, separately for ggF and VBF production, in the mass range $300\,\mathrm{GeV} \leq m_H \leq 1000\,\mathrm{GeV}$. The limits derived from the $H \to WW \to \ell\nu qq$ analysis are comparable to those derived from the $H \to WW \to \ell\nu\ell\nu$ analysis. Figure 11 shows the upper limits on a Higgs boson with a narrow width in the range $300\,\mathrm{GeV} \leq m_H \leq 1500\,\mathrm{GeV}$, separately for ggF and VBF production.

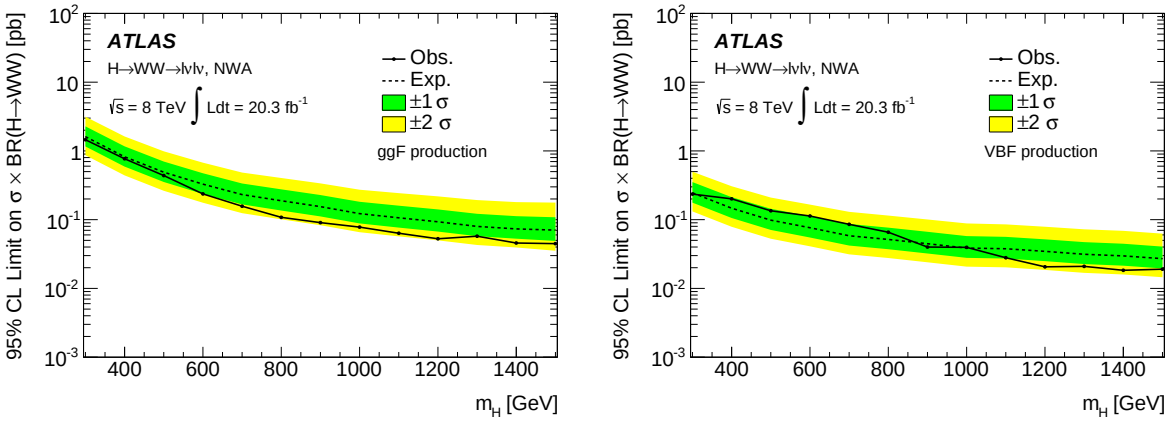

Figure 9: 95% CL upper limits on $\sigma_H \times \mathrm{BR}(H \to WW)$ from the $H \to WW \to \ell\nu\ell\nu$ analysis for a signal with a narrow width. Limits for ggF production (left) and VBF production (right) are shown. The green and yellow bands show the $\pm 1\sigma$ and $\pm 2\sigma$ uncertainties on the expected limit.

The systematic uncertainties with the largest effect on the observed limits at $m_H = 300\,\mathrm{GeV}$ are those related to the jet energy scale and resolution, the multijet background estimation, and the b-jet tagging, particularly the uncertainty on the rate for mistakenly tagging a light-quark jet as a b-jet. As the tested mass hypothesis increases, the $m_{\ell\nu jj}$ shape uncertainties on the W+jets and top backgrounds become the leading sources of uncertainty and the multijet background systematic uncertainties become negligible. For the CPS scenario, the uncertainty on the interference weighting also becomes a dominant systematic uncertainty at high m_H.

To show the overall effect of systematic uncertainties, the exercise done for the $H \to WW \to \ell\nu\ell\nu$ analysis is repeated. If systematic uncertainties are omitted, the observed ggF limits in the CPS scenario decrease by 66% at $m_H = 300\,\mathrm{GeV}$ and 40% at $m_H = 1000\,\mathrm{GeV}$. The corresponding VBF limits decrease by about 40% and 20%, respectively. The trends relative to m_H and ggF vs. VBF are similar to what is seen in the dilepton final state, but systematic uncertainties have a larger effect on the $H \to WW \to \ell\nu qq$ limits than on the $H \to WW \to \ell\nu\ell\nu$ limits because the larger candidate event samples in the former analysis result in smaller statistical uncertainties.

The downward excursions of the observed limits compared to the expected ones seen for $m_H \gtrsim 600\,\mathrm{GeV}$ in Figure 10 in the ggF category and for $m_H \approx 750\,\mathrm{GeV}$ in both categories in Figure 11 have been investigated and no underlying systematic effect identified. In particular, the simultaneous dip in the ggF and VBF NWA limits at $m_H \approx 750\,\mathrm{GeV}$ is attributable to a coincidence of deficits in the data in the statistically independent ggF and VBF SRs at that value of $m_{\ell\nu jj}$.

9.4 Combined upper limits

This section presents 95% CL upper limits on the production of high-mass Higgs bosons in the CPS and NWA scenarios from a combination of the $H \to WW \to \ell\nu\ell\nu$ and $H \to WW \to \ell\nu qq$ final states. In

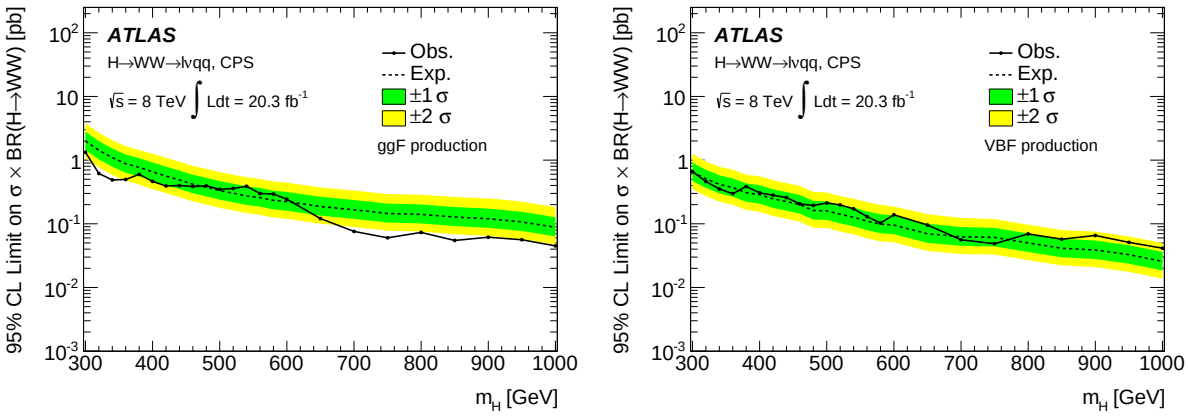

Figure 10: 95% CL upper limits on $\sigma_H \times \mathrm{BR}(H \to WW)$ from the $H \to WW \to \ell\nu qq$ analysis for the CPS scenario. Limits for ggF production (left) and VBF production (right) are shown. The green and yellow bands show the $\pm 1\sigma$ and $\pm 2\sigma$ uncertainties on the expected limit.

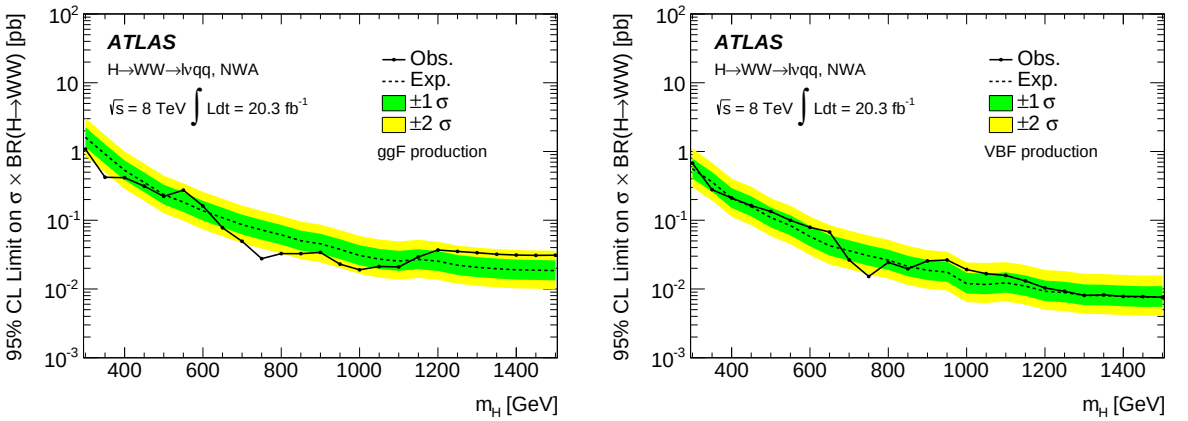

Figure 11: 95% CL upper limits on $\sigma_H \times \mathrm{BR}(H \to WW)$ from the $H \to WW \to \ell\nu qq$ analysis for a signal with a narrow width. Limits for ggF production (left) and VBF production (right) are shown. The green and yellow bands show the $\pm 1\sigma$ and $\pm 2\sigma$ uncertainties on the expected limit.

the statistical combination, the likelihood function is constructed from the signal and background probability density functions from the two analyses. The combination takes into account all statistical and systematic uncertainties in both analyses. In particular, correlated effects of given sources of systematic uncertainties in the two final states are taken into account correctly. These correlated effects arise from sources of uncertainty common to the final states, for example, those related to detector response affecting the reconstruction, identification and calibration of electrons, muons, jets, $E_{\mathrm{T}}^{\mathrm{miss}}$ and b-tagging, as well as the integrated luminosity. Systematic uncertainties that affect both final states are correlated in the combination unless there is a specific reason not to correlate them.

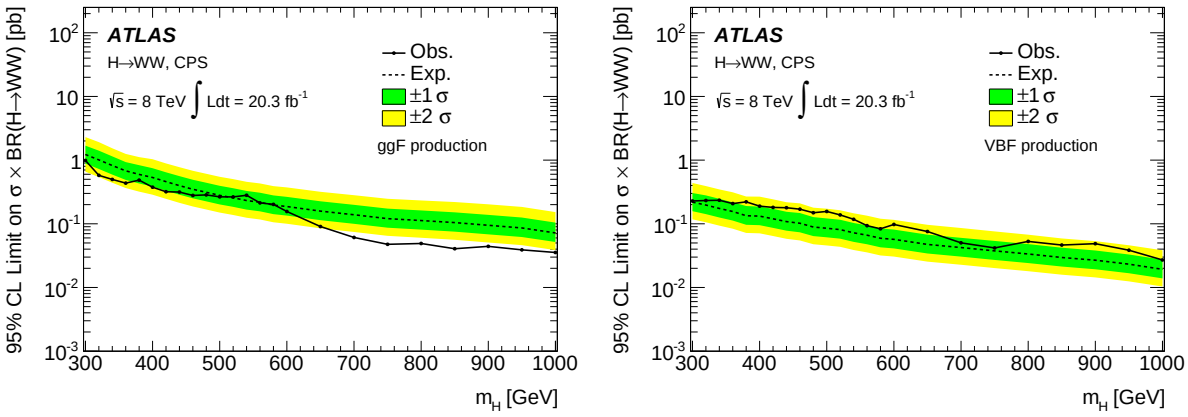

Figure 12: 95% CL upper limits on $\sigma_H \times \mathrm{BR}(H \to WW)$ for the CPS scenario from the combination of the $H \to WW \to \ell\nu\ell\nu$ and $H \to WW \to \ell\nu qq$ final states. Limits for ggF production (left) and VBF production (right) are shown. The green and yellow bands show the $\pm 1\sigma$ and $\pm 2\sigma$ uncertainties on the expected limit.

Since the $H \to WW \to \ell\nu qq$ analysis sets upper limits starting at a Higgs boson mass hypothesis of 300 GeV, the combination is performed starting at $m_H = 300\,\mathrm{GeV}$. In the CPS scenario, the upper range of the combination is $m_H = 1000\,\mathrm{GeV}$ since neither analysis performs the search above this mass because of the large width. In the NWA case, the upper range of the combination extends to $m_H = 1500\,\mathrm{GeV}$.

Figure 12 shows combined upper limits separately on the ggF and VBF production modes for a Higgs boson in the CPS scenario. As in the case of the $H \to WW \to \ell\nu\ell\nu$ and $H \to WW \to \ell\nu qq$ final states, when expected limits on a given production mode are extracted, the cross section of the other production mode is set to zero, while for deriving observed limits on the production mode, the cross section of the other mode is profiled using data.

Figure 13 shows the limits on $\sigma_H \times \mathrm{BR}(H \to WW)$ as a function of m_H for a narrow-width Higgs boson, separately for the ggF and VBF production modes. As in the CPS scenario, when observed limits on a given production mode are extracted, the strength parameter of the other production mode is profiled as a nuisance parameter in the fit.

9.5 Results in the intermediate-width scenario

The data can also be interpreted in terms of an additional Higgs boson with a width intermediate between the narrow-width approximation and the CPS scenario. This interpretation is motivated by the electroweak singlet (EWS) model, and assumes that the production cross sections and partial widths of the heavy Higgs boson are related to those of the SM Higgs boson by a single, constant scale factor $(\kappa')^2$. This allows combination of the ggF and VBF production modes as well as the two WW decay channels considered here. Non-SM decay modes, possible in the EWS model, are not considered in this analysis and the branching ratios of the heavy Higgs boson are the same as for a hypothetical SM Higgs boson of the same

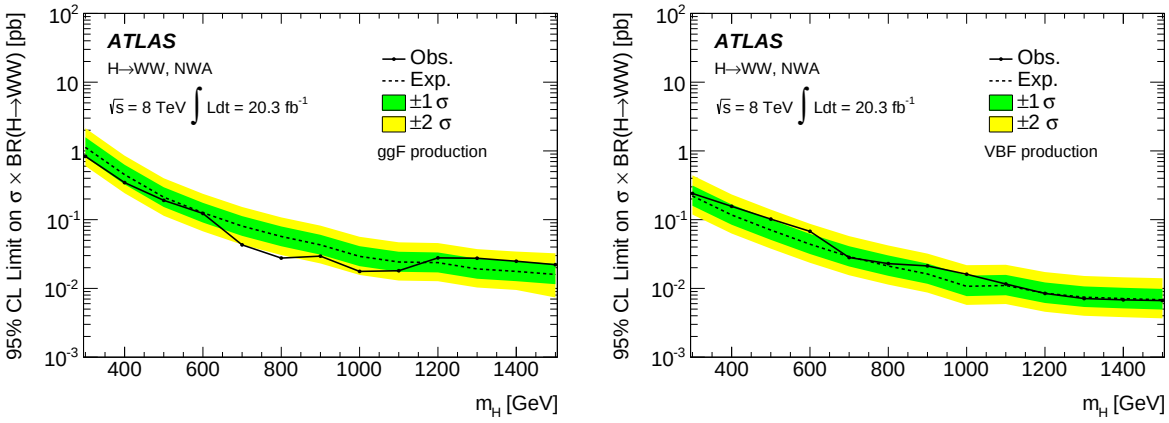

Figure 13: 95% CL upper limits on $\sigma_H \times \mathrm{BR}(H \to WW)$ for a signal with a narrow width from the combination of the $H \to WW \to \ell\nu\ell\nu$ and $H \to WW \to \ell\nu qq$ final states. Limits for ggF production (left) and VBF production (right) are shown. The green and yellow bands show the $\pm 1\sigma$ and $\pm 2\sigma$ uncertainties on the expected limit.

mass. The cross section, width and branching ratio of the heavy Higgs boson can be expressed as follows:

$$\begin{aligned} \sigma_H &= \kappa'^2 \times \sigma_{H,\mathrm{SM}} \\ \Gamma_H &= \kappa'^2 \times \Gamma_{H,\mathrm{SM}} \\ \mathrm{BR}_i &= \mathrm{BR}_{\mathrm{SM},i}. \end{aligned} \tag{10}$$

where $\sigma_{H,\mathrm{SM}}$, $\Gamma_{H,\mathrm{SM}}$, and $\mathrm{BR}_{\mathrm{SM},i}$ are the cross section, total width and branching ratio to decay mode i of a SM Higgs boson with mass m_H, respectively. The parameters of a true electroweak singlet model are substantially constrained by measurements of the Higgs boson at $m_H \approx 125\,\mathrm{GeV}$ [3]. The treatment described here allows a greater spectrum of possible widths to be explored.

Figure 14 shows upper limits in the $H \to WW \to \ell\nu\ell\nu$ channel as a function of m_H in the intermediate-width scenario for widths in the range $0.2\Gamma_{H,\mathrm{SM}} \leq \Gamma_H \leq 0.8\Gamma_{H,\mathrm{SM}}$. Limits are shown on $\sigma_H \times \mathrm{BR}(H \to WW)$ divided by κ'^2 to facilitate readability, since otherwise the limit curves corresponding to the various κ'^2 values approximately coincide. This feature indicates that the $H \to WW \to \ell\nu\ell\nu$ channel has little sensitivity to the width of the resonance. Similarly, Figure 15 shows corresponding limits for the $H \to WW \to \ell\nu qq$ analysis, and Figure 16 shows the combination of the $H \to WW \to \ell\nu\ell\nu$ and $H \to WW \to \ell\nu qq$ analyses.

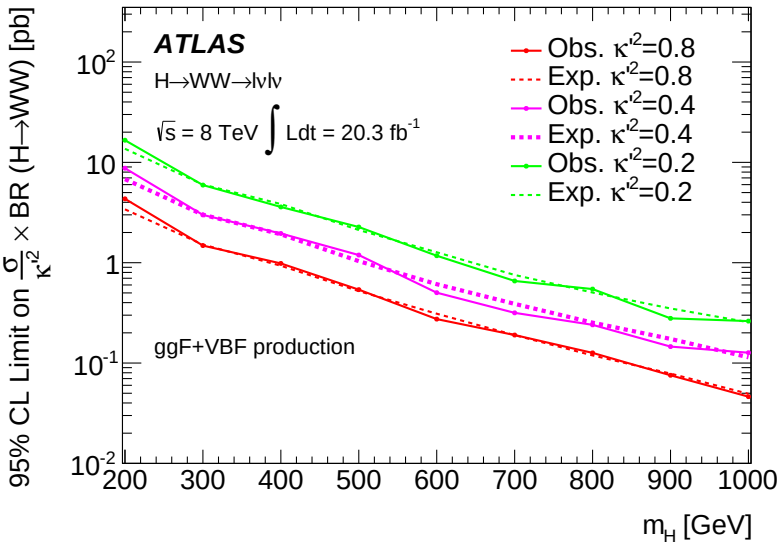

Figure 14: 95% CL upper limits in the intermediate-width scenario on $\frac{\sigma_H}{\kappa'^2} \times \mathrm{BR}(H \rightarrow WW)$ from the $H \rightarrow WW \rightarrow \ell\nu\ell\nu$ analysis for a heavy scalar resonance with width in the range $0.2\Gamma_{H,\mathrm{SM}} \leq \Gamma_H \leq 0.8\Gamma_{H,\mathrm{SM}}$. The ggF and VBF production modes have been combined.

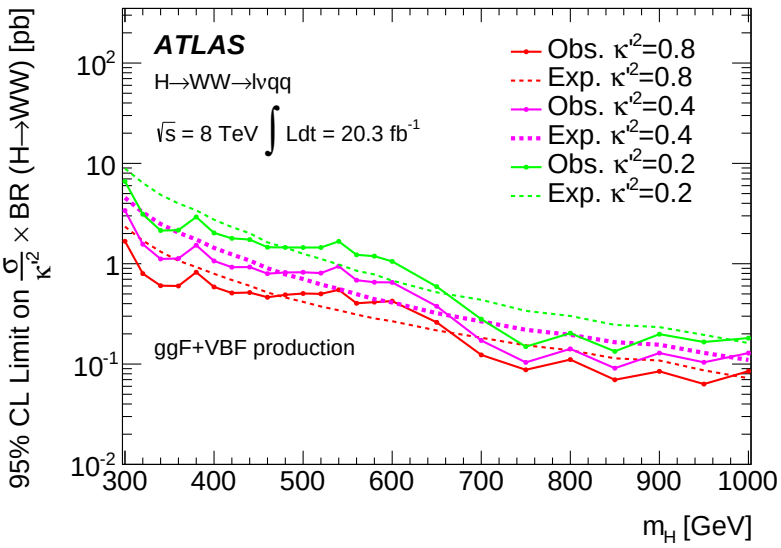

Figure 15: 95% CL upper limits in the intermediate-width scenario on $\frac{\sigma_H}{\kappa'^2} \times \mathrm{BR}(H \rightarrow WW)$ from the $H \rightarrow WW \rightarrow \ell\nu qq$ analysis for a heavy scalar resonance with width in the range $0.2\Gamma_{H,\mathrm{SM}} \leq \Gamma_H \leq 0.8\Gamma_{H,\mathrm{SM}}$. The ggF and VBF production modes have been combined.

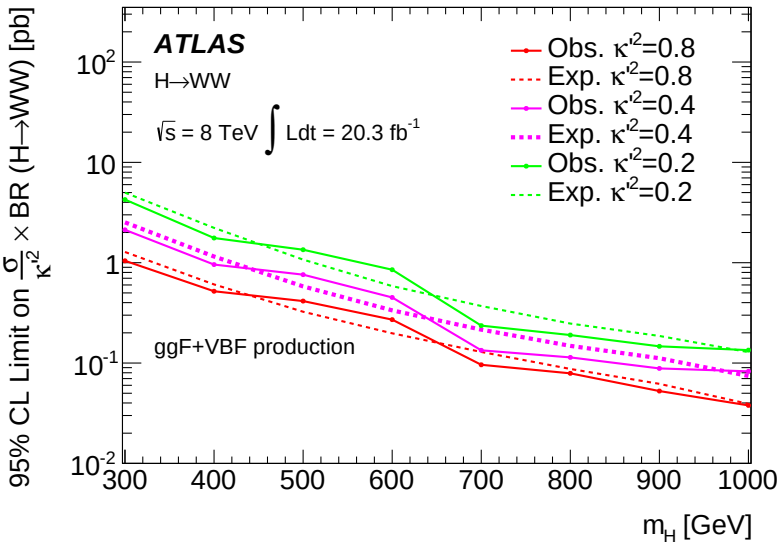

Figure 16: 95% CL upper limits in the intermediate-width scenario from the combination of the $H \to WW \to \ell\nu\ell\nu$ and $H \to WW \to \ell\nu qq$ final states. Limits are set on $\frac{\sigma_H}{\kappa'^2} \times \mathrm{BR}(H \to WW)$ for a heavy scalar resonance with a width in the range $0.2\Gamma_{H,\mathrm{SM}} \leq \Gamma_H \leq 0.8\Gamma_{H,\mathrm{SM}}$. The ggF and VBF production modes have been combined.

10 Conclusion

A search for a high-mass Higgs boson in the $H \to WW \to \ell\nu\ell\nu$ and $H \to WW \to \ell\nu qq$ channels by the ATLAS experiment at the LHC is reported. The search uses proton–proton collision data at a centre-of-mass energy of 8 TeV corresponding to an integrated luminosity of 20.3 fb^{-1}. No excess of events beyond the Standard Model background prediction is found. Upper limits are set on the product of the production cross section and the $H \to WW$ branching ratio in three different scenarios: a high-mass Higgs boson with a CPS lineshape and the width predicted for a SM Higgs boson, one with a narrow width, and one with an intermediate width.

For all mass hypotheses tested, the strongest upper limits are observed for the narrow-width scenario. At $m_H = 300\,\mathrm{GeV}$, these are $\sigma_H \times \mathrm{BR}(H \to WW) < 830$ fb at 95% CL for the gluon-fusion production mode and $\sigma_H \times \mathrm{BR}(H \to WW) < 240$ fb at 95% CL for the vector-boson fusion production mode. For $m_H = 1500\,\mathrm{GeV}$, the highest mass-point tested, the cross section times branching ratio is constrained to be less than 22 fb and 6.6 fb at the 95% CL for the ggF and VBF production modes, respectively.

The limits in the CPS and intermediate-width scenarios are qualitatively similar but somewhat weaker due to the increased resonance width, particularly for m_H approaching 1 TeV. For the CPS scenario, the combined 95% CL upper limits on $\sigma_H \times \mathrm{BR}(H \to WW)$ for the ggF production mode range from 990 fb at $m_H = 300\,\mathrm{GeV}$ to 35 fb at $m_H = 1000\,\mathrm{GeV}$. For the VBF production mode, the equivalent values are 230 fb and 27 fb, respectively. These results are a substantial improvement over the previous results from

the ATLAS experiment in terms of both the range of m_H explored and the cross section times branching ratio values excluded.

We thank CERN for the very successful operation of the LHC, as well as the support staff from our institutions without whom ATLAS could not be operated efficiently.

We acknowledge the support of ANPCyT, Argentina; YerPhI, Armenia; ARC, Australia; BMWFW and FWF, Austria; ANAS, Azerbaijan; SSTC, Belarus; CNPq and FAPESP, Brazil; NSERC, NRC and CFI, Canada; CERN; CONICYT, Chile; CAS, MOST and NSFC, China; COLCIENCIAS, Colombia; MSMT CR, MPO CR and VSC CR, Czech Republic; DNRF, DNSRC and Lundbeck Foundation, Denmark; EPLANET, ERC and NSRF, European Union; IN2P3-CNRS, CEA-DSM/IRFU, France; GNSF, Georgia; BMBF, DFG, HGF, MPG and AvH Foundation, Germany; GSRT and NSRF, Greece; RGC, Hong Kong SAR, China; ISF, MINERVA, GIF, I-CORE and Benoziyo Center, Israel; INFN, Italy; MEXT and JSPS, Japan; CNRST, Morocco; FOM and NWO, Netherlands; BRF and RCN, Norway; MNiSW and NCN, Poland; GRICES and FCT, Portugal; MNE/IFA, Romania; MES of Russia and NRC KI, Russian Federation; JINR; MSTD, Serbia; MSSR, Slovakia; ARRS and MIZŠ, Slovenia; DST/NRF, South Africa; MINECO, Spain; SRC and Wallenberg Foundation, Sweden; SER, SNSF and Cantons of Bern and Geneva, Switzerland; NSC, Taiwan; TAEK, Turkey; STFC, the Royal Society and Leverhulme Trust, United Kingdom; DOE and NSF, United States of America.

The crucial computing support from all WLCG partners is acknowledged gratefully, in particular from CERN and the ATLAS Tier-1 facilities at TRIUMF (Canada), NDGF (Denmark, Norway, Sweden), CC-IN2P3 (France), KIT/GridKA (Germany), INFN-CNAF (Italy), NL-T1 (Netherlands), PIC (Spain), ASGC (Taiwan), RAL (UK) and BNL (USA) and in the Tier-2 facilities worldwide.

References

[1] ATLAS Collaboration, *Observation of a new particle in the search for the Standard Model Higgs boson with the ATLAS detector at the LHC*, Phys. Lett. **B716** (2012) 1–29, arXiv:1207.7214 [hep-ex].

[2] CMS Collaboration, *Observation of a new boson at a mass of 125 GeV with the CMS experiment at the LHC*, Phys. Lett. **B716** (2012) 30–61, arXiv:1207.7235 [hep-ex].

[3] ATLAS Collaboration, *Measurements of the Higgs boson production and decay rates and coupling strengths using pp collision data at $\sqrt{s}$ = 7 and 8 TeV in the ATLAS experiment* (2015), arXiv:1507.04548 [hep-ex].

[4] CMS Collaboration, *Precise determination of the mass of the Higgs boson and tests of compatibility of its couplings with the standard model predictions using proton collisions at 7 and 8 TeV*, Eur. Phys. J. **C75** (2014) 212, arXiv:1412.8662 [hep-ex].

[5] A. Hill and J. van der Bij, *Strongly interacting singlet-doublet Higgs model*, Phys. Rev. **D36** (1987) 3463–3473.

[6] M. Veltman and F. Yndurain, *Radiative corrections to WW scattering*, Nucl. Phys. **B325** (1989) 1–17.

[7] T. Binoth and J. van der Bij, *Influence of strongly coupled, hidden scalars on Higgs signals*, Z. Phys. **C75** (1997) 17–25, arXiv:hep-ph/9608245 [hep-ph].

[8] R. Schabinger and J. D. Wells, *A minimal spontaneously broken hidden sector and its impact on Higgs boson physics at the large hadron collider*, Phys. Rev. D **72** (2005) 093007, arXiv:hep-ph/0509209 [hep-ph].

[9] B. Patt and F. Wilczek, *Higgs-field portal into hidden sectors* (2006), arXiv:hep-ph/0605188 [hep-ph].

[10] LHC Higgs Cross Section Working Group, *Handbook of LHC Higgs Cross Sections: 3. Higgs Properties*, CERN-2013-004 (2013), arXiv:1307.1347 [hep-ph].

[11] ATLAS Collaboration, *Search for the Standard Model Higgs boson in the $H \to WW^{(*)} \to \ell\nu\ell\nu$ decay mode with 4.7 fb^{-1} of ATLAS data at $\sqrt{s}$ = 7 TeV*, Phys. Lett. **B716** (2012) 62–81, arXiv:1206.0756 [hep-ex].

[12] ATLAS Collaboration, *Search for the Higgs boson in the $H \to WW \to l\nu jj$ decay channel at $\sqrt{s}$ = 7 TeV with the ATLAS detector*, Phys. Lett. **B718** (2012) 391–410, arXiv:1206.6074 [hep-ex].

[13] CMS Collaboration, *Search for a Higgs boson in the mass range from 145 to 1000 GeV decaying to a pair of W or Z bosons* (2015), arXiv:1504.00936 [hep-ex].

[14] C. Anastasiou et al., *Inclusive Higgs boson cross-section for the LHC at 8 TeV*, JHEP **1204** (2012) 4, arXiv:1202.3638 [hep-ph].

[15] N. Kauer and G. Passarino,
Inadequacy of zero-width approximation for a light Higgs boson signal, JHEP **1208** (2012) 116, arXiv:1206.4803 [hep-ph].

[16] S. Goria, G. Passarino and D. Rosco, *The Higgs Boson Lineshape*, Nucl. Phys. **B864** (2012) 530–579, arXiv:1112.5517 [hep-ph].

[17] G. Passarino, *Higgs Interference Effects in $gg \to ZZ$ and their Uncertainty*, JHEP **1208** (2012) 146, arXiv:1206.3824 [hep-ph].

[18] J. M. Campbell, R. K. Ellis and C. Williams,
Gluon-gluon contributions to W+ W- production and Higgs interference effects, JHEP **1110** (2011) 005, arXiv:1107.5569 [hep-ph].

[19] N. Kauer, *Signal-background interference in $gg \to H \to VV$*, PoS RADCOR2011 (2011) 027, arXiv:1201.1667 [hep-ph].

[20] M. Bonvini et al.,
Signal-background interference effects for $gg \to H \to W^+W^-$ beyond leading order, Phys. Rev. **D88** (2013) 034032, arXiv:1304.3053 [hep-ph].

[21] ATLAS Collaboration, *The ATLAS experiment at the CERN Large Hadron Collider*, JINST **3** (2008) S08003.

[22] ATLAS Collaboration, *Electron reconstruction and identification efficiency measurements with the ATLAS detector using the 2011 LHC proton-proton collision data*, Eur. Phys. J. **C74** (2014) 2941, arXiv:1404.2240 [hep-ex].

[23] ATLAS Collaboration, *Electron efficiency measurements with the ATLAS detector using the 2012 LHC proton-proton collision data*,
ATLAS-CONF-2014-032 (2014), https://cdsweb.cern.ch/record/1706245.

[24] ATLAS Collaboration,
Electron and photon energy calibration with the ATLAS detector using LHC Run 1 data, Eur. Phys. J. **C74** (2014) 3071, arXiv:1407.5063 [hep-ex].

[25] ATLAS Collaboration, *Measurement of the muon reconstruction performance of the ATLAS detector using 2011 and 2012 LHC proton-proton collision data*, Eur. Phys. J. **C74** (2014) 3130, arXiv:1407.3935 [hep-ex].

[26] M. Cacciari and G. P. Salam, *Pileup subtraction using jet areas*, Phys. Lett. **B 659** (2008) 119.

[27] ATLAS Collaboration, *Jet energy measurement and its systematic uncertainty in proton-proton collisions at $\sqrt{s} = 7$ TeV with the ATLAS detector*, Eur. Phys. J. **C75** (2015) 17, arXiv:1406.0076 [hep-ex].

[28] W. Lampl et al., *Calorimeter Clustering Algorithms: Description and Performance*, ATL-LARG-PUB-2008-002 (2008), https://cdsweb.cern.ch/record/1099735.

[29] ATLAS Collaboration, *Tagging and suppression of pileup jets with the ATLAS detector*, ATLAS-CONF-2014-018 (2014), https://cdsweb.cern.ch/record/1700870.

[30] M. Cacciari, G. P. Salam and G. Soyez, *The anti-k_t jet clustering algorithm*, JHEP **0804** (2008) 063, arXiv:0802.1189 [hep-ex].

[31] Y. L. Dokshitzer et al., *Better jet clustering algorithms*, JHEP **9708** (1997) 001, arXiv:hep-ph/9707323 [hep-ph].

[32] J. M. Butterworth et al., *Jet substructure as a new Higgs search channel at the LHC*, Phys. Rev. Lett. **100** (2008) 242001, arXiv:0802.2470 [hep-ph].

[33] ATLAS Collaboration, *Calibration of b-tagging using dileptonic top pair events in a combinatorial likelihood approach with the ATLAS experiment*, ATLAS-CONF-2014-004 (2014), https://cdsweb.cern.ch/record/1664335.

[34] ATLAS Collaboration, *Calibration of the performance of b-tagging for c and light-flavour jets in the 2012 ATLAS data*, ATLAS-CONF-2014-046 (2014), https://cdsweb.cern.ch/record/1741020.

[35] ATLAS Collaboration, *Performance of missing transverse momentum reconstruction in proton-proton collisions at 7 TeV with ATLAS*, Eur. Phys. J. C **72** (2012) 1844, arXiv:1108.5602 [hep-ex].

[36] T. Sjöstrand, S. Mrenna and P. Z. Skands, *A Brief Introduction to PYTHIA 8.1*, Comput. Phys. Commun. **178** (2008) 852–867, arXiv:0710.3820 [hep-ph].

[37] T. Sjöstrand, S. Mrenna, and P. Z. Skands, *PYTHIA 6.4 physics and manual*, JHEP **0605** (2006) 026, arXiv:hep-ph/0603175.

[38] G. Corcella et al., *HERWIG 6: An event generator for hadron emission reactions with interfering gluons (including super-symmetric processes)*, JHEP **0101** (2001) 010.

[39] T. Gleisberg et al., *Event generation with SHERPA 1.1*, JHEP **0902** (2009) 007, arXiv:0811.4622 [hep-ph].

[40] J. M. Butterworth, J. R. Forshaw and M. H. Seymour, *Multiparton interactions in photoproduction at HERA*, Z. Phys. **C72** (1996) 637, arXiv:hep-ph/9601371.

[41] H.-L. Lai et al., *New parton distributions for collider physics*, Phys. Rev. D **82** (2010) 074024, arXiv:1007.2241 [hep-ph].

[42] P. Nason and C. Oleari, *NLO Higgs boson production via vector-boson fusion matched with shower in POWHEG*, JHEP **1002** (2010) 037, arXiv:0911.5299 [hep-ph].

[43] P. M. Nadolsky et al., *Implications of CTEQ global analysis for collider observables*, Phys. Rev. D **78** (2008) 013004, arXiv:0802.0007 [hep-ph].

[44] M. L. Mangano et al., *ALPGEN, a generator for hard multi-parton processes in hadronic collisions*, JHEP **0307** (2003) 001, arXiv:hep-ph/0206293.

[45] T. Binoth, M. Ciccolini, N. Kauer and M. Krämer, *Gluon-induced W-boson pair production at the LHC*, JHEP **0612** (2006) 046, arXiv:hep-ph/0611170.

[46] ATLAS Collaboration, *The ATLAS simulation infrastructure*, Eur. Phys. J. C **70** (2010) 823, arXiv:1005.4568 [physics.ins-det].

[47] S. Agostinelli et al., *GEANT4: A simulation toolkit*, Nucl. Instrum. Meth. **A506** (2003) 250–303.

[48] ATLAS Collaboration,
The simulation principle and performance of the ATLAS fast calorimeter simulation FastCaloSim,
ATLAS-PHYS-PUB-2010-013 (2010), https://cdsweb.cern.ch/record/1300517.

[49] A. Djouadi, M. Spira and P. Zerwas,
Production of Higgs bosons in proton colliders: QCD corrections,
Phys. Lett. **B264** (1991) 440–446.

[50] S. Dawson, *Radiative corrections to Higgs boson production*, Nucl. Phys. **B359** (1991) 283–300.

[51] M. Spira et al., *Higgs boson production at the LHC*, Nucl. Phys. **B453** (1995) 17–82,
arXiv:hep-ph/9504378 [hep-ph].

[52] R. Harlander and W. B. Kilgore,
Next-to-next-to-leading order Higgs production at hadron colliders, **88** (2002) 201801,
arXiv:hep-ph/0201206.

[53] C. Anastasiou and K. Melnikov, *Higgs boson production at hadron colliders in NNLO QCD*,
Nucl. Phys. **B646** (2002) 220–256, arXiv:hep-ph/0207004 [hep-ph].

[54] V. Ravindran, J. Smith and W. L. van Neerven, *NNLO corrections to the total cross-section for Higgs boson production in hadron hadron collisions*, Nucl. Phys. **B665** (2003) 325–366,
arXiv:hep-ph/0302135 [hep-ph].

[55] U. Aglietti et al., *Two loop light fermion contribution to Higgs production and decays*,
Phys. Lett. **B595** (2004) 432–441, arXiv:hep-ph/0404071 [hep-ph].

[56] S. Actis et al., *NLO electroweak corrections to Higgs boson production at hadron colliders*,
Phys. Lett. **B670** (2008) 12–17, arXiv:0809.1301 [hep-ph].

[57] S. Catani et al., *Soft-gluon re-summation for Higgs boson production at hadron colliders*,
JHEP **0307** (2003) 028, arXiv:hep-ph/0306211.

[58] D. de Florian and M. Grazzini,
Higgs production at the LHC: updated cross sections at $\sqrt{s} = 8$ *TeV*,
Phys. Lett. **B718** (2012) 117–120, arXiv:1206.4133 [hep-ph].

[59] J. Baglio and A. Djouadi, *Higgs production at the LHC*, JHEP **1103** (2011) 055,
arXiv:1012.0530 [hep-ph].

[60] P. Bolzoni et al., *Higgs production via vector-boson fusion at NNLO in QCD*,
Phys. Rev. Lett. **105** (2010) 011801, arXiv:1003.4451 [hep-ph].

[61] M. Ciccolini, A. Denner and S. Dittmaier, *Strong and electroweak corrections to the production of Higgs+2 jets via weak interactions at the LHC*, Phys. Rev. Lett. **99** (2007) 161803,
arXiv:0707.0381 [hep-ph].

[62] M. Ciccolini, A. Denner and S. Dittmaier,
Electroweak and QCD corrections to Higgs production via vector-boson fusion at the LHC,
Phys. Rev. **D 77** (2008) 013002, arXiv:0710.4749 [hep-ph].

[63] K. Arnold et al., *VBFNLO: A parton level Monte Carlo for processes with electroweak bosons*,
Comput. Phys. Commun. **180** (2009) 1661, arXiv:0811.4559 [hep-ph].

[64] A. Djouadi, J. Kalinowski, and M. Spira, *HDECAY: A program for Higgs boson decays in the Standard Model and its supersymmetric extension*, Comput. Phys. Commun. **108** (1998) 56, arXiv:hep-ph/9704448.

[65] A. Bredenstein et al., *Precise predictions for the Higgs-boson decay $H \to WW/ZZ \to 4$ leptons*, Phys. Rev. **D74** (2006) 013004, arXiv:hep-ph/0604011 [hep-ph].

[66] A. Bredenstein et al., *Radiative corrections to the semileptonic and hadronic Higgs-boson decays $H \to WW/ZZ \to 4$ fermions*, JHEP **0702** (2007) 080, arXiv:hep-ph/0611234.

[67] J. M. Campbell and R. Ellis, *MCFM for the Tevatron and the LHC*, Nucl. Phys. Proc. Suppl. **205-206** (2010) 10–15, arXiv:1007.3492 [hep-ph].

[68] K. Arnold et al., *Release Note – VBFNLO-2.6.0* (2012), arXiv:1207.4975 [hep-ph].

[69] T. Figy, C. Oleari and D. Zeppenfeld, *Next-to-leading order jet distributions for Higgs boson production via weak boson fusion*, Phys. Rev. **D68** (2003) 073005, arXiv:hep-ph/0306109 [hep-ph].

[70] P. Bolzoni et al., *Vector boson fusion at NNLO in QCD: SM Higgs and beyond*, Phys. Rev. **D85** (2012) 035002, arXiv:1109.3717 [hep-ph].

[71] J. M. Campbell, R. K. Ellis and C. Williams, *Vector boson pair production at the LHC*, JHEP **07** (2011) 018, arXiv:1105.0020 [hep-ph].

[72] M. Czakon, P. Fiedler and A. Mitov, *Total Top-Quark Pair-Production Cross Section at Hadron Colliders Through $O(\alpha_S^4)$*, Phys. Rev. Lett. **110** (2013) 252004, arXiv:1303.6254 [hep-ph].

[73] M. Czakon and A. Mitov, *NNLO corrections to top pair production at hadron colliders: the quark-gluon reaction*, JHEP **1301** (2013) 080, arXiv:1210.6832 [hep-ph].

[74] M. Czakon and A. Mitov, *NNLO corrections to top-pair production at hadron colliders: the all-fermionic scattering channels*, JHEP **1212** (2012) 054, arXiv:1207.0236 [hep-ph].

[75] N. Kidonakis, *NNLL resummation for s-channel single top quark production*, Phys. Rev. **D81** (2010) 054028, arXiv:1001.5034 [hep-ph].

[76] N. Kidonakis, *Next-to-next-to-leading-order collinear and soft gluon corrections for t-channel single top quark production*, Phys. Rev. **D83** (2011) 091503, arXiv:1103.2792 [hep-ph].

[77] N. Kidonakis, *Two-loop soft anomalous dimensions for single top quark associated production with a W- or H-*, Phys. Rev. **D82** (2010) 054018, arXiv:1005.4451 [hep-ph].

[78] B. P. Kersevan and E. Richter-Was, *The Monte Carlo event generator AcerMC versions 2.0 to 3.8 with interfaces to PYTHIA 6.4, HERWIG 6.5 and ARIADNE 4.1*, Comput. Phys. Commun. **184** (2013) 919–985, arXiv:hep-ph/0405247 [hep-ph].

[79] S. Catani and M. Grazzini, *An NNLO subtraction formalism in hadron collisions and its application to Higgs boson production at the LHC*, Phys. Rev. Lett. **98** (2007) 222002, arXiv:hep-ph/0703012.

[80] S. Catani et al.,
Vector boson production at hadron colliders: a fully exclusive QCD calculation at NNLO,
103 (2009) 082001, arXiv:0903.2120 [hep-ph].

[81] ATLAS Collaboration, *Search for the Standard Model Higgs boson produced in association with top quarks and decaying into $b\bar{b}$ in pp collisions at $\sqrt{s}$ = 8 TeV with the ATLAS detector*,
Eur. Phys. J. **C75** (2015) 349, arXiv:1503.05066 [hep-ex].

[82] ATLAS Collaboration, *Measurements of normalized differential cross sections for $t\bar{t}$ production in pp collisions at $\sqrt{s}$ = 7 TeV using the ATLAS detector*, Phys. Rev. **D90** (2014) 072004,
arXiv:1407.0371 [hep-ex].

[83] ATLAS Collaboration,
Observation and measurement of Higgs boson decays to WW^* with the ATLAS detector,
Phys. Rev. **D92** (2015) 012006, arXiv:1412.2641 [hep-ex].

[84] G. Choudalakis, *On hypothesis testing, trials factor, hypertests and the BumpHunter* (2011),
arXiv:1101.0390 [physics.data-an].

[85] B. Mellado, X. Ruan, and Z. Zhang, *Extraction of top backgrounds in the Higgs boson search with the $H \to WW^\star \to \ell\ell + E_T^{miss}$ decay with a full-jet veto at the LHC*,
Phys. Rev. D **84** (2011) 096005, arXiv:1101.1383 [hep-ph].

[86] ATLAS Collaboration, *Improved luminosity determination in pp collisions at $\sqrt{s}$ = 7 TeV using the ATLAS detector at the LHC*, Eur. Phys. J. C **73** (2013) 2518, arXiv:1302.4393 [hep-ex].

[87] LHC Higgs Cross Section Working Group,
Handbook of LHC Higgs Cross Sections: 1. Inclusive Observables,
CERN-2011-002 (CERN, Geneva, 2011), arXiv:1101.0593 [hep-ph].

[88] LHC Higgs Cross Section Working Group,
Handbook of LHC Higgs Cross Sections: 2. Differential Distributions,
CERN-2012-002 (CERN, Geneva, 2012), arXiv:1201.3084 [hep-ph].

[89] M. Grazzini, *NNLO predictions for the Higgs boson signal in the $H \to WW \to lvlv$ and $H \to ZZ \to 4l$ decay channels*, JHEP **0802** (2008) 043, arXiv:0801.3232 [hep-ph].

[90] I. Stewart and F. Tackmann,
Theory uncertainties for Higgs mass and other searches using jet bins,
Phys. Rev. D **85** (2012) 034011, arXiv:1107.2117 [hep-ph].

[91] J. Alwall et al., *MadGraph/MadEvent v4: The new web generation*, JHEP **0709** (2007) 028,
arXiv:0706.2334 [hep-ph].

[92] ATLAS Collaboration, *Measurement of the electroweak production of dijets in association with a Z-boson and distributions sensitive to vector boson fusion in proton-proton collisions at $\sqrt{s}$ = 8 TeV using the ATLAS detector*, JHEP **1404** (2014) 031, arXiv:1401.7610 [hep-ex].

[93] ATLAS Collaboration, *Jet mass and substructure of inclusive jets in $\sqrt{s}$ = 7 TeV pp collisions with the ATLAS experiment*, JHEP **1205** (2012) 128, arXiv:1203.4606 [hep-ex].

[94] S. Frixione and B. R. Webber, *Matching NLO QCD computations and parton shower simulations*,
JHEP **0206** (2002) 029, arXiv:hep-ph/0204244.

[95] ATLAS Collaboration, *Combined search for the Standard Model Higgs boson in pp collisions at $\sqrt{s}$ = 7 TeV with the ATLAS detector*, Phys. Rev. **D86** (2012) 032003, arXiv:1207.0319 [hep-ex].

[96] A.L. Read, *Presentation of search results: the CL_s technique*, J. Phys. **G28** (2002) 2693.

[97] G. Cowan et al., *Asymptotic formulae for likelihood-based tests of new physics*, Eur. Phys. J. C **71** (2011) 1554, [Erratum: Eur. Phys. J.C73,2501(2013)], arXiv:1007.1727 [physics.data-an].

The ATLAS Collaboration

G. Aad[85], B. Abbott[113], J. Abdallah[151], O. Abdinov[11], R. Aben[107], M. Abolins[90], O.S. AbouZeid[158], H. Abramowicz[153], H. Abreu[152], R. Abreu[116], Y. Abulaiti[146a,146b], B.S. Acharya[164a,164b,a], L. Adamczyk[38a], D.L. Adams[25], J. Adelman[108], S. Adomeit[100], T. Adye[131], A.A. Affolder[74], T. Agatonovic-Jovin[13], J. Agricola[54], J.A. Aguilar-Saavedra[126a,126f], S.P. Ahlen[22], F. Ahmadov[65,b], G. Aielli[133a,133b], H. Akerstedt[146a,146b], T.P.A. Åkesson[81], A.V. Akimov[96], G.L. Alberghi[20a,20b], J. Albert[169], S. Albrand[55], M.J. Alconada Verzini[71], M. Aleksa[30], I.N. Aleksandrov[65], C. Alexa[26a], G. Alexander[153], T. Alexopoulos[10], M. Alhroob[113], G. Alimonti[91a], L. Alio[85], J. Alison[31], S.P. Alkire[35], B.M.M. Allbrooke[149], P.P. Allport[74], A. Aloisio[104a,104b], A. Alonso[36], F. Alonso[71], C. Alpigiani[76], A. Altheimer[35], B. Alvarez Gonzalez[30], D. Álvarez Piqueras[167], M.G. Alviggi[104a,104b], B.T. Amadio[15], K. Amako[66], Y. Amaral Coutinho[24a], C. Amelung[23], D. Amidei[89], S.P. Amor Dos Santos[126a,126c], A. Amorim[126a,126b], S. Amoroso[48], N. Amram[153], G. Amundsen[23], C. Anastopoulos[139], L.S. Ancu[49], N. Andari[108], T. Andeen[35], C.F. Anders[58b], G. Anders[30], J.K. Anders[74], K.J. Anderson[31], A. Andreazza[91a,91b], V. Andrei[58a], S. Angelidakis[9], I. Angelozzi[107], P. Anger[44], A. Angerami[35], F. Anghinolfi[30], A.V. Anisenkov[109,c], N. Anjos[12], A. Annovi[124a,124b], M. Antonelli[47], A. Antonov[98], J. Antos[144b], F. Anulli[132a], M. Aoki[66], L. Aperio Bella[18], G. Arabidze[90], Y. Arai[66], J.P. Araque[126a], A.T.H. Arce[45], F.A. Arduh[71], J-F. Arguin[95], S. Argyropoulos[63], M. Arik[19a], A.J. Armbruster[30], O. Arnaez[30], V. Arnal[82], H. Arnold[48], M. Arratia[28], O. Arslan[21], A. Artamonov[97], G. Artoni[23], S. Asai[155], N. Asbah[42], A. Ashkenazi[153], B. Åsman[146a,146b], L. Asquith[149], K. Assamagan[25], R. Astalos[144a], M. Atkinson[165], N.B. Atlay[141], K. Augsten[128], M. Aurousseau[145b], G. Avolio[30], B. Axen[15], M.K. Ayoub[117], G. Azuelos[95,d], M.A. Baak[30], A.E. Baas[58a], M.J. Baca[18], C. Bacci[134a,134b], H. Bachacou[136], K. Bachas[154], M. Backes[30], M. Backhaus[30], P. Bagiacchi[132a,132b], P. Bagnaia[132a,132b], Y. Bai[33a], T. Bain[35], J.T. Baines[131], O.K. Baker[176], E.M. Baldin[109,c], P. Balek[129], T. Balestri[148], F. Balli[84], W.K. Balunas[122], E. Banas[39], Sw. Banerjee[173], A.A.E. Bannoura[175], H.S. Bansil[18], L. Barak[30], E.L. Barberio[88], D. Barberis[50a,50b], M. Barbero[85], T. Barillari[101], M. Barisonzi[164a,164b], T. Barklow[143], N. Barlow[28], S.L. Barnes[84], B.M. Barnett[131], R.M. Barnett[15], Z. Barnovska[5], A. Baroncelli[134a], G. Barone[23], A.J. Barr[120], F. Barreiro[82], J. Barreiro Guimarães da Costa[57], R. Bartoldus[143], A.E. Barton[72], P. Bartos[144a], A. Basalaev[123], A. Bassalat[117], A. Basye[165], R.L. Bates[53], S.J. Batista[158], J.R. Batley[28], M. Battaglia[137], M. Bauce[132a,132b], F. Bauer[136], H.S. Bawa[143,e], J.B. Beacham[111], M.D. Beattie[72], T. Beau[80], P.H. Beauchemin[161], R. Beccherle[124a,124b], P. Bechtle[21], H.P. Beck[17,f], K. Becker[120], M. Becker[83], M. Beckingham[170], C. Becot[117], A.J. Beddall[19b], A. Beddall[19b], V.A. Bednyakov[65], C.P. Bee[148], L.J. Beemster[107], T.A. Beermann[30], M. Begel[25], J.K. Behr[120], C. Belanger-Champagne[87], W.H. Bell[49], G. Bella[153], L. Bellagamba[20a], A. Bellerive[29], M. Bellomo[86], K. Belotskiy[98], O. Beltramello[30], O. Benary[153], D. Benchekroun[135a], M. Bender[100], K. Bendtz[146a,146b], N. Benekos[10], Y. Benhammou[153], E. Benhar Noccioli[49], J.A. Benitez Garcia[159b], D.P. Benjamin[45], J.R. Bensinger[23], S. Bentvelsen[107], L. Beresford[120], M. Beretta[47], D. Berge[107], E. Bergeaas Kuutmann[166], N. Berger[5], F. Berghaus[169], J. Beringer[15], C. Bernard[22], N.R. Bernard[86], C. Bernius[110], F.U. Bernlochner[21], T. Berry[77], P. Berta[129], C. Bertella[83], G. Bertoli[146a,146b], F. Bertolucci[124a,124b], C. Bertsche[113], D. Bertsche[113], M.I. Besana[91a], G.J. Besjes[36], O. Bessidskaia Bylund[146a,146b], M. Bessner[42], N. Besson[136], C. Betancourt[48], S. Bethke[101], A.J. Bevan[76], W. Bhimji[15], R.M. Bianchi[125], L. Bianchini[23], M. Bianco[30], O. Biebel[100], D. Biedermann[16], S.P. Bieniek[78], M. Biglietti[134a], J. Bilbao De Mendizabal[49], H. Bilokon[47], M. Bindi[54], S. Binet[117],

A. Bingul[19b], C. Bini[132a,132b], S. Biondi[20a,20b], D.M. Bjergaard[45], C.W. Black[150], J.E. Black[143], K.M. Black[22], D. Blackburn[138], R.E. Blair[6], J.-B. Blanchard[136], J.E. Blanco[77], T. Blazek[144a], I. Bloch[42], C. Blocker[23], W. Blum[83,*], U. Blumenschein[54], G.J. Bobbink[107], V.S. Bobrovnikov[109,c], S.S. Bocchetta[81], A. Bocci[45], C. Bock[100], M. Boehler[48], J.A. Bogaerts[30], D. Bogavac[13], A.G. Bogdanchikov[109], C. Bohm[146a], V. Boisvert[77], T. Bold[38a], V. Boldea[26a], A.S. Boldyrev[99], M. Bomben[80], M. Bona[76], M. Boonekamp[136], A. Borisov[130], G. Borissov[72], S. Borroni[42], J. Bortfeldt[100], V. Bortolotto[60a,60b,60c], K. Bos[107], D. Boscherini[20a], M. Bosman[12], J. Boudreau[125], J. Bouffard[2], E.V. Bouhova-Thacker[72], D. Boumediene[34], C. Bourdarios[117], N. Bousson[114], S.K. Boutle[53], A. Boveia[30], J. Boyd[30], I.R. Boyko[65], I. Bozic[13], J. Bracinik[18], A. Brandt[8], G. Brandt[54], O. Brandt[58a], U. Bratzler[156], B. Brau[86], J.E. Brau[116], H.M. Braun[175,*], S.F. Brazzale[164a,164c], W.D. Breaden Madden[53], K. Brendlinger[122], A.J. Brennan[88], L. Brenner[107], R. Brenner[166], S. Bressler[172], K. Bristow[145c], T.M. Bristow[46], D. Britton[53], D. Britzger[42], F.M. Brochu[28], I. Brock[21], R. Brock[90], J. Bronner[101], G. Brooijmans[35], T. Brooks[77], W.K. Brooks[32b], J. Brosamer[15], E. Brost[116], J. Brown[55], P.A. Bruckman de Renstrom[39], D. Bruncko[144b], R. Bruneliere[48], A. Bruni[20a], G. Bruni[20a], M. Bruschi[20a], N. Bruscino[21], L. Bryngemark[81], T. Buanes[14], Q. Buat[142], P. Buchholz[141], A.G. Buckley[53], S.I. Buda[26a], I.A. Budagov[65], F. Buehrer[48], L. Bugge[119], M.K. Bugge[119], O. Bulekov[98], D. Bullock[8], H. Burckhart[30], S. Burdin[74], C.D. Burgard[48], B. Burghgrave[108], S. Burke[131], I. Burmeister[43], E. Busato[34], D. Büscher[48], V. Büscher[83], P. Bussey[53], J.M. Butler[22], A.I. Butt[3], C.M. Buttar[53], J.M. Butterworth[78], P. Butti[107], W. Buttinger[25], A. Buzatu[53], A.R. Buzykaev[109,c], S. Cabrera Urbán[167], D. Caforio[128], V.M. Cairo[37a,37b], O. Cakir[4a], N. Calace[49], P. Calafiura[15], A. Calandri[136], G. Calderini[80], P. Calfayan[100], L.P. Caloba[24a], D. Calvet[34], S. Calvet[34], R. Camacho Toro[31], S. Camarda[42], P. Camarri[133a,133b], D. Cameron[119], R. Caminal Armadans[165], S. Campana[30], M. Campanelli[78], A. Campoverde[148], V. Canale[104a,104b], A. Canepa[159a], M. Cano Bret[33e], J. Cantero[82], R. Cantrill[126a], T. Cao[40], M.D.M. Capeans Garrido[30], I. Caprini[26a], M. Caprini[26a], M. Capua[37a,37b], R. Caputo[83], R. Cardarelli[133a], F. Cardillo[48], T. Carli[30], G. Carlino[104a], L. Carminati[91a,91b], S. Caron[106], E. Carquin[32a], G.D. Carrillo-Montoya[30], J.R. Carter[28], J. Carvalho[126a,126c], D. Casadei[78], M.P. Casado[12], M. Casolino[12], E. Castaneda-Miranda[145a], A. Castelli[107], V. Castillo Gimenez[167], N.F. Castro[126a,g], P. Catastini[57], A. Catinaccio[30], J.R. Catmore[119], A. Cattai[30], J. Caudron[83], V. Cavaliere[165], D. Cavalli[91a], M. Cavalli-Sforza[12], V. Cavasinni[124a,124b], F. Ceradini[134a,134b], B.C. Cerio[45], K. Cerny[129], A.S. Cerqueira[24b], A. Cerri[149], L. Cerrito[76], F. Cerutti[15], M. Cerv[30], A. Cervelli[17], S.A. Cetin[19c], A. Chafaq[135a], D. Chakraborty[108], I. Chalupkova[129], P. Chang[165], J.D. Chapman[28], D.G. Charlton[18], C.C. Chau[158], C.A. Chavez Barajas[149], S. Cheatham[152], A. Chegwidden[90], S. Chekanov[6], S.V. Chekulaev[159a], G.A. Chelkov[65,h], M.A. Chelstowska[89], C. Chen[64], H. Chen[25], K. Chen[148], L. Chen[33d,i], S. Chen[33c], S. Chen[155], X. Chen[33f], Y. Chen[67], H.C. Cheng[89], Y. Cheng[31], A. Cheplakov[65], E. Cheremushkina[130], R. Cherkaoui El Moursli[135e], V. Chernyatin[25,*], E. Cheu[7], L. Chevalier[136], V. Chiarella[47], G. Chiarelli[124a,124b], G. Chiodini[73a], A.S. Chisholm[18], R.T. Chislett[78], A. Chitan[26a], M.V. Chizhov[65], K. Choi[61], S. Chouridou[9], B.K.B. Chow[100], V. Christodoulou[78], D. Chromek-Burckhart[30], J. Chudoba[127], A.J. Chuinard[87], J.J. Chwastowski[39], L. Chytka[115], G. Ciapetti[132a,132b], A.K. Ciftci[4a], D. Cinca[53], V. Cindro[75], I.A. Cioara[21], A. Ciocio[15], F. Cirotto[104a,104b], Z.H. Citron[172], M. Ciubancan[26a], A. Clark[49], B.L. Clark[57], P.J. Clark[46], R.N. Clarke[15], W. Cleland[125], C. Clement[146a,146b], Y. Coadou[85], M. Cobal[164a,164c], A. Coccaro[49], J. Cochran[64], L. Coffey[23], J.G. Cogan[143], L. Colasurdo[106], B. Cole[35], S. Cole[108], A.P. Colijn[107], J. Collot[55], T. Colombo[58c], G. Compostella[101], P. Conde Muiño[126a,126b], E. Coniavitis[48], S.H. Connell[145b], I.A. Connelly[77], V. Consorti[48], S. Constantinescu[26a], C. Conta[121a,121b], G. Conti[30], F. Conventi[104a,j], M. Cooke[15], B.D. Cooper[78], A.M. Cooper-Sarkar[120], T. Cornelissen[175], M. Corradi[20a], F. Corriveau[87,k],

A. Corso-Radu[163], A. Cortes-Gonzalez[12], G. Cortiana[101], G. Costa[91a], M.J. Costa[167], D. Costanzo[139], D. Côté[8], G. Cottin[28], G. Cowan[77], B.E. Cox[84], K. Cranmer[110], G. Cree[29], S. Crépé-Renaudin[55], F. Crescioli[80], W.A. Cribbs[146a,146b], M. Crispin Ortuzar[120], M. Cristinziani[21], V. Croft[106], G. Crosetti[37a,37b], T. Cuhadar Donszelmann[139], J. Cummings[176], M. Curatolo[47], J. Cúth[83], C. Cuthbert[150], H. Czirr[141], P. Czodrowski[3], S. D'Auria[53], M. D'Onofrio[74], M.J. Da Cunha Sargedas De Sousa[126a,126b], C. Da Via[84], W. Dabrowski[38a], A. Dafinca[120], T. Dai[89], O. Dale[14], F. Dallaire[95], C. Dallapiccola[86], M. Dam[36], J.R. Dandoy[31], N.P. Dang[48], A.C. Daniells[18], M. Danninger[168], M. Dano Hoffmann[136], V. Dao[48], G. Darbo[50a], S. Darmora[8], J. Dassoulas[3], A. Dattagupta[61], W. Davey[21], C. David[169], T. Davidek[129], E. Davies[120,l], M. Davies[153], P. Davison[78], Y. Davygora[58a], E. Dawe[88], I. Dawson[139], R.K. Daya-Ishmukhametova[86], K. De[8], R. de Asmundis[104a], A. De Benedetti[113], S. De Castro[20a,20b], S. De Cecco[80], N. De Groot[106], P. de Jong[107], H. De la Torre[82], F. De Lorenzi[64], D. De Pedis[132a], A. De Salvo[132a], U. De Sanctis[149], A. De Santo[149], J.B. De Vivie De Regie[117], W.J. Dearnaley[72], R. Debbe[25], C. Debenedetti[137], D.V. Dedovich[65], I. Deigaard[107], J. Del Peso[82], T. Del Prete[124a,124b], D. Delgove[117], F. Deliot[136], C.M. Delitzsch[49], M. Deliyergiyev[75], A. Dell'Acqua[30], L. Dell'Asta[22], M. Dell'Orso[124a,124b], M. Della Pietra[104a,j], D. della Volpe[49], M. Delmastro[5], P.A. Delsart[55], C. Deluca[107], D.A. DeMarco[158], S. Demers[176], M. Demichev[65], A. Demilly[80], S.P. Denisov[130], D. Derendarz[39], J.E. Derkaoui[135d], F. Derue[80], P. Dervan[74], K. Desch[21], C. Deterre[42], P.O. Deviveiros[30], A. Dewhurst[131], S. Dhaliwal[23], A. Di Ciaccio[133a,133b], L. Di Ciaccio[5], A. Di Domenico[132a,132b], C. Di Donato[104a,104b], A. Di Girolamo[30], B. Di Girolamo[30], A. Di Mattia[152], B. Di Micco[134a,134b], R. Di Nardo[47], A. Di Simone[48], R. Di Sipio[158], D. Di Valentino[29], C. Diaconu[85], M. Diamond[158], F.A. Dias[46], M.A. Diaz[32a], E.B. Diehl[89], J. Dietrich[16], S. Diglio[85], A. Dimitrievska[13], J. Dingfelder[21], P. Dita[26a], S. Dita[26a], F. Dittus[30], F. Djama[85], T. Djobava[51b], J.I. Djuvsland[58a], M.A.B. do Vale[24c], D. Dobos[30], M. Dobre[26a], C. Doglioni[81], T. Dohmae[155], J. Dolejsi[129], Z. Dolezal[129], B.A. Dolgoshein[98,*], M. Donadelli[24d], S. Donati[124a,124b], P. Dondero[121a,121b], J. Donini[34], J. Dopke[131], A. Doria[104a], M.T. Dova[71], A.T. Doyle[53], E. Drechsler[54], M. Dris[10], E. Dubreuil[34], E. Duchovni[172], G. Duckeck[100], O.A. Ducu[26a,85], D. Duda[107], A. Dudarev[30], L. Duflot[117], L. Duguid[77], M. Dührssen[30], M. Dunford[58a], H. Duran Yildiz[4a], M. Düren[52], A. Durglishvili[51b], D. Duschinger[44], M. Dyndal[38a], C. Eckardt[42], K.M. Ecker[101], R.C. Edgar[89], W. Edson[2], N.C. Edwards[46], W. Ehrenfeld[21], T. Eifert[30], G. Eigen[14], K. Einsweiler[15], T. Ekelof[166], M. El Kacimi[135c], M. Ellert[166], S. Elles[5], F. Ellinghaus[175], A.A. Elliot[169], N. Ellis[30], J. Elmsheuser[100], M. Elsing[30], D. Emeliyanov[131], Y. Enari[155], O.C. Endner[83], M. Endo[118], J. Erdmann[43], A. Ereditato[17], G. Ernis[175], J. Ernst[2], M. Ernst[25], S. Errede[165], E. Ertel[83], M. Escalier[117], H. Esch[43], C. Escobar[125], B. Esposito[47], A.I. Etienvre[136], E. Etzion[153], H. Evans[61], A. Ezhilov[123], L. Fabbri[20a,20b], G. Facini[31], R.M. Fakhrutdinov[130], S. Falciano[132a], R.J. Falla[78], J. Faltova[129], Y. Fang[33a], M. Fanti[91a,91b], A. Farbin[8], A. Farilla[134a], T. Farooque[12], S. Farrell[15], S.M. Farrington[170], P. Farthouat[30], F. Fassi[135e], P. Fassnacht[30], D. Fassouliotis[9], M. Faucci Giannelli[77], A. Favareto[50a,50b], L. Fayard[117], P. Federic[144a], O.L. Fedin[123,m], W. Fedorko[168], S. Feigl[30], L. Feligioni[85], C. Feng[33d], E.J. Feng[6], H. Feng[89], A.B. Fenyuk[130], L. Feremenga[8], P. Fernandez Martinez[167], S. Fernandez Perez[30], J. Ferrando[53], A. Ferrari[166], P. Ferrari[107], R. Ferrari[121a], D.E. Ferreira de Lima[53], A. Ferrer[167], D. Ferrere[49], C. Ferretti[89], A. Ferretto Parodi[50a,50b], M. Fiascaris[31], F. Fiedler[83], A. Filipčič[75], M. Filipuzzi[42], F. Filthaut[106], M. Fincke-Keeler[169], K.D. Finelli[150], M.C.N. Fiolhais[126a,126c], L. Fiorini[167], A. Firan[40], A. Fischer[2], C. Fischer[12], J. Fischer[175], W.C. Fisher[90], E.A. Fitzgerald[23], N. Flaschel[42], I. Fleck[141], P. Fleischmann[89], S. Fleischmann[175], G.T. Fletcher[139], G. Fletcher[76], R.R.M. Fletcher[122], T. Flick[175], A. Floderus[81], L.R. Flores Castillo[60a], M.J. Flowerdew[101], A. Formica[136], A. Forti[84], D. Fournier[117], H. Fox[72],

S. Fracchia[12], P. Francavilla[80], M. Franchini[20a,20b], D. Francis[30], L. Franconi[119], M. Franklin[57], M. Frate[163], M. Fraternali[121a,121b], D. Freeborn[78], S.T. French[28], F. Friedrich[44], D. Froidevaux[30], J.A. Frost[120], C. Fukunaga[156], E. Fullana Torregrosa[83], B.G. Fulsom[143], T. Fusayasu[102], J. Fuster[167], C. Gabaldon[55], O. Gabizon[175], A. Gabrielli[20a,20b], A. Gabrielli[15], G.P. Gach[38a], S. Gadatsch[30], S. Gadomski[49], G. Gagliardi[50a,50b], P. Gagnon[61], C. Galea[106], B. Galhardo[126a,126c], E.J. Gallas[120], B.J. Gallop[131], P. Gallus[128], G. Galster[36], K.K. Gan[111], J. Gao[33b,85], Y. Gao[46], Y.S. Gao[143,e], F.M. Garay Walls[46], F. Garberson[176], C. García[167], J.E. García Navarro[167], M. Garcia-Sciveres[15], R.W. Gardner[31], N. Garelli[143], V. Garonne[119], C. Gatti[47], A. Gaudiello[50a,50b], G. Gaudio[121a], B. Gaur[141], L. Gauthier[95], P. Gauzzi[132a,132b], I.L. Gavrilenko[96], C. Gay[168], G. Gaycken[21], E.N. Gazis[10], P. Ge[33d], Z. Gecse[168], C.N.P. Gee[131], Ch. Geich-Gimbel[21], M.P. Geisler[58a], C. Gemme[50a], M.H. Genest[55], S. Gentile[132a,132b], M. George[54], S. George[77], D. Gerbaudo[163], A. Gershon[153], S. Ghasemi[141], H. Ghazlane[135b], B. Giacobbe[20a], S. Giagu[132a,132b], V. Giangiobbe[12], P. Giannetti[124a,124b], B. Gibbard[25], S.M. Gibson[77], M. Gilchriese[15], T.P.S. Gillam[28], D. Gillberg[30], G. Gilles[34], D.M. Gingrich[3,d], N. Giokaris[9], M.P. Giordani[164a,164c], F.M. Giorgi[20a], F.M. Giorgi[16], P.F. Giraud[136], P. Giromini[47], D. Giugni[91a], C. Giuliani[48], M. Giulini[58b], B.K. Gjelsten[119], S. Gkaitatzis[154], I. Gkialas[154], E.L. Gkougkousis[117], L.K. Gladilin[99], C. Glasman[82], J. Glatzer[30], P.C.F. Glaysher[46], A. Glazov[42], M. Goblirsch-Kolb[101], J.R. Goddard[76], J. Godlewski[39], S. Goldfarb[89], T. Golling[49], D. Golubkov[130], A. Gomes[126a,126b,126d], R. Gonçalo[126a], J. Goncalves Pinto Firmino Da Costa[136], L. Gonella[21], S. González de la Hoz[167], G. Gonzalez Parra[12], S. Gonzalez-Sevilla[49], L. Goossens[30], P.A. Gorbounov[97], H.A. Gordon[25], I. Gorelov[105], B. Gorini[30], E. Gorini[73a,73b], A. Gorišek[75], E. Gornicki[39], A.T. Goshaw[45], C. Gössling[43], M.I. Gostkin[65], D. Goujdami[135c], A.G. Goussiou[138], N. Govender[145b], E. Gozani[152], H.M.X. Grabas[137], L. Graber[54], I. Grabowska-Bold[38a], P.O.J. Gradin[166], P. Grafström[20a,20b], K-J. Grahn[42], J. Gramling[49], E. Gramstad[119], S. Grancagnolo[16], V. Gratchev[123], H.M. Gray[30], E. Graziani[134a], Z.D. Greenwood[79,n], C. Grefe[21], K. Gregersen[78], I.M. Gregor[42], P. Grenier[143], J. Griffiths[8], A.A. Grillo[137], K. Grimm[72], S. Grinstein[12,o], Ph. Gris[34], J.-F. Grivaz[117], J.P. Grohs[44], A. Grohsjean[42], E. Gross[172], J. Grosse-Knetter[54], G.C. Grossi[79], Z.J. Grout[149], L. Guan[89], J. Guenther[128], F. Guescini[49], D. Guest[176], O. Gueta[153], E. Guido[50a,50b], T. Guillemin[117], S. Guindon[2], U. Gul[53], C. Gumpert[44], J. Guo[33e], Y. Guo[33b], S. Gupta[120], G. Gustavino[132a,132b], P. Gutierrez[113], N.G. Gutierrez Ortiz[78], C. Gutschow[44], C. Guyot[136], C. Gwenlan[120], C.B. Gwilliam[74], A. Haas[110], C. Haber[15], H.K. Hadavand[8], N. Haddad[135e], P. Haefner[21], S. Hageböck[21], Z. Hajduk[39], H. Hakobyan[177], M. Haleem[42], J. Haley[114], D. Hall[120], G. Halladjian[90], G.D. Hallewell[85], K. Hamacher[175], P. Hamal[115], K. Hamano[169], A. Hamilton[145a], G.N. Hamity[139], P.G. Hamnett[42], L. Han[33b], K. Hanagaki[66,p], K. Hanawa[155], M. Hance[15], B. Haney[122], P. Hanke[58a], R. Hanna[136], J.B. Hansen[36], J.D. Hansen[36], M.C. Hansen[21], P.H. Hansen[36], K. Hara[160], A.S. Hard[173], T. Harenberg[175], F. Hariri[117], S. Harkusha[92], R.D. Harrington[46], P.F. Harrison[170], F. Hartjes[107], M. Hasegawa[67], Y. Hasegawa[140], A. Hasib[113], S. Hassani[136], S. Haug[17], R. Hauser[90], L. Hauswald[44], M. Havranek[127], C.M. Hawkes[18], R.J. Hawkings[30], A.D. Hawkins[81], T. Hayashi[160], D. Hayden[90], C.P. Hays[120], J.M. Hays[76], H.S. Hayward[74], S.J. Haywood[131], S.J. Head[18], T. Heck[83], V. Hedberg[81], L. Heelan[8], S. Heim[122], T. Heim[175], B. Heinemann[15], L. Heinrich[110], J. Hejbal[127], L. Helary[22], S. Hellman[146a,146b], D. Hellmich[21], C. Helsens[12], J. Henderson[120], R.C.W. Henderson[72], Y. Heng[173], C. Hengler[42], S. Henkelmann[168], A. Henrichs[176], A.M. Henriques Correia[30], S. Henrot-Versille[117], G.H. Herbert[16], Y. Hernández Jiménez[167], R. Herrberg-Schubert[16], G. Herten[48], R. Hertenberger[100], L. Hervas[30], G.G. Hesketh[78], N.P. Hessey[107], J.W. Hetherly[40], R. Hickling[76], E. Higón-Rodriguez[167], E. Hill[169], J.C. Hill[28], K.H. Hiller[42], S.J. Hillier[18], I. Hinchliffe[15], E. Hines[122], R.R. Hinman[15], M. Hirose[157],

D. Hirschbuehl[175], J. Hobbs[148], N. Hod[107], M.C. Hodgkinson[139], P. Hodgson[139], A. Hoecker[30], M.R. Hoeferkamp[105], F. Hoenig[100], M. Hohlfeld[83], D. Hohn[21], T.R. Holmes[15], M. Homann[43], T.M. Hong[125], L. Hooft van Huysduynen[110], W.H. Hopkins[116], Y. Horii[103], A.J. Horton[142], J-Y. Hostachy[55], S. Hou[151], A. Hoummada[135a], J. Howard[120], J. Howarth[42], M. Hrabovsky[115], I. Hristova[16], J. Hrivnac[117], T. Hryn'ova[5], A. Hrynevich[93], C. Hsu[145c], P.J. Hsu[151,q], S.-C. Hsu[138], D. Hu[35], Q. Hu[33b], X. Hu[89], Y. Huang[42], Z. Hubacek[128], F. Hubaut[85], F. Huegging[21], T.B. Huffman[120], E.W. Hughes[35], G. Hughes[72], M. Huhtinen[30], T.A. Hülsing[83], N. Huseynov[65,b], J. Huston[90], J. Huth[57], G. Iacobucci[49], G. Iakovidis[25], I. Ibragimov[141], L. Iconomidou-Fayard[117], E. Ideal[176], Z. Idrissi[135e], P. Iengo[30], O. Igonkina[107], T. Iizawa[171], Y. Ikegami[66], K. Ikematsu[141], M. Ikeno[66], Y. Ilchenko[31,r], D. Iliadis[154], N. Ilic[143], T. Ince[101], G. Introzzi[121a,121b], P. Ioannou[9], M. Iodice[134a], K. Iordanidou[35], V. Ippolito[57], A. Irles Quiles[167], C. Isaksson[166], M. Ishino[68], M. Ishitsuka[157], R. Ishmukhametov[111], C. Issever[120], S. Istin[19a], J.M. Iturbe Ponce[84], R. Iuppa[133a,133b], J. Ivarsson[81], W. Iwanski[39], H. Iwasaki[66], J.M. Izen[41], V. Izzo[104a], S. Jabbar[3], B. Jackson[122], M. Jackson[74], P. Jackson[1], M.R. Jaekel[30], V. Jain[2], K. Jakobs[48], S. Jakobsen[30], T. Jakoubek[127], J. Jakubek[128], D.O. Jamin[114], D.K. Jana[79], E. Jansen[78], R. Jansky[62], J. Janssen[21], M. Janus[54], G. Jarlskog[81], N. Javadov[65,b], T. Javůrek[48], L. Jeanty[15], J. Jejelava[51a,s], G.-Y. Jeng[150], D. Jennens[88], P. Jenni[48,t], J. Jentzsch[43], C. Jeske[170], S. Jézéquel[5], H. Ji[173], J. Jia[148], Y. Jiang[33b], S. Jiggins[78], J. Jimenez Pena[167], S. Jin[33a], A. Jinaru[26a], O. Jinnouchi[157], M.D. Joergensen[36], P. Johansson[139], K.A. Johns[7], K. Jon-And[146a,146b], G. Jones[170], R.W.L. Jones[72], T.J. Jones[74], J. Jongmanns[58a], P.M. Jorge[126a,126b], K.D. Joshi[84], J. Jovicevic[159a], X. Ju[173], C.A. Jung[43], P. Jussel[62], A. Juste Rozas[12,o], M. Kaci[167], A. Kaczmarska[39], M. Kado[117], H. Kagan[111], M. Kagan[143], S.J. Kahn[85], E. Kajomovitz[45], C.W. Kalderon[120], S. Kama[40], A. Kamenshchikov[130], N. Kanaya[155], S. Kaneti[28], V.A. Kantserov[98], J. Kanzaki[66], B. Kaplan[110], L.S. Kaplan[173], A. Kapliy[31], D. Kar[145c], K. Karakostas[10], A. Karamaoun[3], N. Karastathis[10,107], M.J. Kareem[54], E. Karentzos[10], M. Karnevskiy[83], S.N. Karpov[65], Z.M. Karpova[65], K. Karthik[110], V. Kartvelishvili[72], A.N. Karyukhin[130], L. Kashif[173], R.D. Kass[111], A. Kastanas[14], Y. Kataoka[155], C. Kato[155], A. Katre[49], J. Katzy[42], K. Kawagoe[70], T. Kawamoto[155], G. Kawamura[54], S. Kazama[155], V.F. Kazanin[109,c], R. Keeler[169], R. Kehoe[40], J.S. Keller[42], J.J. Kempster[77], H. Keoshkerian[84], O. Kepka[127], B.P. Kerševan[75], S. Kersten[175], R.A. Keyes[87], F. Khalil-zada[11], H. Khandanyan[146a,146b], A. Khanov[114], A.G. Kharlamov[109,c], T.J. Khoo[28], V. Khovanskiy[97], E. Khramov[65], J. Khubua[51b,u], S. Kido[67], H.Y. Kim[8], S.H. Kim[160], Y.K. Kim[31], N. Kimura[154], O.M. Kind[16], B.T. King[74], M. King[167], S.B. King[168], J. Kirk[131], A.E. Kiryunin[101], T. Kishimoto[67], D. Kisielewska[38a], F. Kiss[48], K. Kiuchi[160], O. Kivernyk[136], E. Kladiva[144b], M.H. Klein[35], M. Klein[74], U. Klein[74], K. Kleinknecht[83], P. Klimek[146a,146b], A. Klimentov[25], R. Klingenberg[43], J.A. Klinger[139], T. Klioutchnikova[30], E.-E. Kluge[58a], P. Kluit[107], S. Kluth[101], J. Knapik[39], E. Kneringer[62], E.B.F.G. Knoops[85], A. Knue[53], A. Kobayashi[155], D. Kobayashi[157], T. Kobayashi[155], M. Kobel[44], M. Kocian[143], P. Kodys[129], T. Koffas[29], E. Koffeman[107], L.A. Kogan[120], S. Kohlmann[175], Z. Kohout[128], T. Kohriki[66], T. Koi[143], H. Kolanoski[16], I. Koletsou[5], A.A. Komar[96,*], Y. Komori[155], T. Kondo[66], N. Kondrashova[42], K. Köneke[48], A.C. König[106], T. Kono[66], R. Konoplich[110,v], N. Konstantinidis[78], R. Kopeliansky[152], S. Koperny[38a], L. Köpke[83], A.K. Kopp[48], K. Korcyl[39], K. Kordas[154], A. Korn[78], A.A. Korol[109,c], I. Korolkov[12], E.V. Korolkova[139], O. Kortner[101], S. Kortner[101], T. Kosek[129], V.V. Kostyukhin[21], V.M. Kotov[65], A. Kotwal[45], A. Kourkoumeli-Charalampidi[154], C. Kourkoumelis[9], V. Kouskoura[25], A. Koutsman[159a], R. Kowalewski[169], T.Z. Kowalski[38a], W. Kozanecki[136], A.S. Kozhin[130], V.A. Kramarenko[99], G. Kramberger[75], D. Krasnopevtsev[98], M.W. Krasny[80], A. Krasznahorkay[30], J.K. Kraus[21], A. Kravchenko[25], S. Kreiss[110], M. Kretz[58c], J. Kretzschmar[74], K. Kreutzfeldt[52], P. Krieger[158],

K. Krizka[31], K. Kroeninger[43], H. Kroha[101], J. Kroll[122], J. Kroseberg[21], J. Krstic[13], U. Kruchonak[65], H. Krüger[21], N. Krumnack[64], A. Kruse[173], M.C. Kruse[45], M. Kruskal[22], T. Kubota[88], H. Kucuk[78], S. Kuday[4b], S. Kuehn[48], A. Kugel[58c], F. Kuger[174], A. Kuhl[137], T. Kuhl[42], V. Kukhtin[65], R. Kukla[136], Y. Kulchitsky[92], S. Kuleshov[32b], M. Kuna[132a,132b], T. Kunigo[68], A. Kupco[127], H. Kurashige[67], Y.A. Kurochkin[92], V. Kus[127], E.S. Kuwertz[169], M. Kuze[157], J. Kvita[115], T. Kwan[169], D. Kyriazopoulos[139], A. La Rosa[137], J.L. La Rosa Navarro[24d], L. La Rotonda[37a,37b], C. Lacasta[167], F. Lacava[132a,132b], J. Lacey[29], H. Lacker[16], D. Lacour[80], V.R. Lacuesta[167], E. Ladygin[65], R. Lafaye[5], B. Laforge[80], T. Lagouri[176], S. Lai[54], L. Lambourne[78], S. Lammers[61], C.L. Lampen[7], W. Lampl[7], E. Lançon[136], U. Landgraf[48], M.P.J. Landon[76], V.S. Lang[58a], J.C. Lange[12], A.J. Lankford[163], F. Lanni[25], K. Lantzsch[21], A. Lanza[121a], S. Laplace[80], C. Lapoire[30], J.F. Laporte[136], T. Lari[91a], F. Lasagni Manghi[20a,20b], M. Lassnig[30], P. Laurelli[47], W. Lavrijsen[15], A.T. Law[137], P. Laycock[74], T. Lazovich[57], O. Le Dortz[80], E. Le Guirriec[85], E. Le Menedeu[12], M. LeBlanc[169], T. LeCompte[6], F. Ledroit-Guillon[55], C.A. Lee[145b], S.C. Lee[151], L. Lee[1], G. Lefebvre[80], M. Lefebvre[169], F. Legger[100], C. Leggett[15], A. Lehan[74], G. Lehmann Miotto[30], X. Lei[7], W.A. Leight[29], A. Leisos[154,w], A.G. Leister[176], M.A.L. Leite[24d], R. Leitner[129], D. Lellouch[172], B. Lemmer[54], K.J.C. Leney[78], T. Lenz[21], B. Lenzi[30], R. Leone[7], S. Leone[124a,124b], C. Leonidopoulos[46], S. Leontsinis[10], C. Leroy[95], C.G. Lester[28], M. Levchenko[123], J. Levêque[5], D. Levin[89], L.J. Levinson[172], M. Levy[18], A. Lewis[120], A.M. Leyko[21], M. Leyton[41], B. Li[33b,x], H. Li[148], H.L. Li[31], L. Li[45], L. Li[33e], S. Li[45], X. Li[84], Y. Li[33c,y], Z. Liang[137], H. Liao[34], B. Liberti[133a], A. Liblong[158], P. Lichard[30], K. Lie[165], J. Liebal[21], W. Liebig[14], C. Limbach[21], A. Limosani[150], S.C. Lin[151,z], T.H. Lin[83], F. Linde[107], B.E. Lindquist[148], J.T. Linnemann[90], E. Lipeles[122], A. Lipniacka[14], M. Lisovyi[58b], T.M. Liss[165], D. Lissauer[25], A. Lister[168], A.M. Litke[137], B. Liu[151,aa], D. Liu[151], H. Liu[89], J. Liu[85], J.B. Liu[33b], K. Liu[85], L. Liu[165], M. Liu[45], M. Liu[33b], Y. Liu[33b], M. Livan[121a,121b], A. Lleres[55], J. Llorente Merino[82], S.L. Lloyd[76], F. Lo Sterzo[151], E. Lobodzinska[42], P. Loch[7], W.S. Lockman[137], F.K. Loebinger[84], A.E. Loevschall-Jensen[36], K.M. Loew[23], A. Loginov[176], T. Lohse[16], K. Lohwasser[42], M. Lokajicek[127], B.A. Long[22], J.D. Long[89], R.E. Long[72], K.A. Looper[111], L. Lopes[126a], D. Lopez Mateos[57], B. Lopez Paredes[139], I. Lopez Paz[12], J. Lorenz[100], N. Lorenzo Martinez[61], M. Losada[162], P.J. Lösel[100], X. Lou[33a], A. Lounis[117], J. Love[6], P.A. Love[72], N. Lu[89], H.J. Lubatti[138], C. Luci[132a,132b], A. Lucotte[55], F. Luehring[61], W. Lukas[62], L. Luminari[132a], O. Lundberg[146a,146b], B. Lund-Jensen[147], D. Lynn[25], R. Lysak[127], E. Lytken[81], H. Ma[25], L.L. Ma[33d], G. Maccarrone[47], A. Macchiolo[101], C.M. Macdonald[139], B. Maček[75], J. Machado Miguens[122,126b], D. Macina[30], D. Madaffari[85], R. Madar[34], H.J. Maddocks[72], W.F. Mader[44], A. Madsen[166], J. Maeda[67], S. Maeland[14], T. Maeno[25], A. Maevskiy[99], E. Magradze[54], K. Mahboubi[48], J. Mahlstedt[107], C. Maiani[136], C. Maidantchik[24a], A.A. Maier[101], T. Maier[100], A. Maio[126a,126b,126d], S. Majewski[116], Y. Makida[66], N. Makovec[117], B. Malaescu[80], Pa. Malecki[39], V.P. Maleev[123], F. Malek[55], U. Mallik[63], D. Malon[6], C. Malone[143], S. Maltezos[10], V.M. Malyshev[109], S. Malyukov[30], J. Mamuzic[42], G. Mancini[47], B. Mandelli[30], L. Mandelli[91a], I. Mandić[75], R. Mandrysch[63], J. Maneira[126a,126b], A. Manfredini[101], L. Manhaes de Andrade Filho[24b], J. Manjarres Ramos[159b], A. Mann[100], A. Manousakis-Katsikakis[9], B. Mansoulie[136], R. Mantifel[87], M. Mantoani[54], L. Mapelli[30], L. March[145c], G. Marchiori[80], M. Marcisovsky[127], C.P. Marino[169], M. Marjanovic[13], D.E. Marley[89], F. Marroquim[24a], S.P. Marsden[84], Z. Marshall[15], L.F. Marti[17], S. Marti-Garcia[167], B. Martin[90], T.A. Martin[170], V.J. Martin[46], B. Martin dit Latour[14], M. Martinez[12,o], S. Martin-Haugh[131], V.S. Martoiu[26a], A.C. Martyniuk[78], M. Marx[138], F. Marzano[132a], A. Marzin[30], L. Masetti[83], T. Mashimo[155], R. Mashinistov[96], J. Masik[84], A.L. Maslennikov[109,c], I. Massa[20a,20b], L. Massa[20a,20b], P. Mastrandrea[148], A. Mastroberardino[37a,37b], T. Masubuchi[155], P. Mättig[175], J. Mattmann[83], J. Maurer[26a], S.J. Maxfield[74],

D.A. Maximov[109,c], R. Mazini[151], S.M. Mazza[91a,91b], L. Mazzaferro[133a,133b], G. Mc Goldrick[158], S.P. Mc Kee[89], A. McCarn[89], R.L. McCarthy[148], T.G. McCarthy[29], N.A. McCubbin[131], K.W. McFarlane[56,*], J.A. Mcfayden[78], G. Mchedlidze[54], S.J. McMahon[131], R.A. McPherson[169,k], M. Medinnis[42], S. Meehan[145a], S. Mehlhase[100], A. Mehta[74], K. Meier[58a], C. Meineck[100], B. Meirose[41], B.R. Mellado Garcia[145c], F. Meloni[17], A. Mengarelli[20a,20b], S. Menke[101], E. Meoni[161], K.M. Mercurio[57], S. Mergelmeyer[21], P. Mermod[49], L. Merola[104a,104b], C. Meroni[91a], F.S. Merritt[31], A. Messina[132a,132b], J. Metcalfe[25], A.S. Mete[163], C. Meyer[83], C. Meyer[122], J-P. Meyer[136], J. Meyer[107], H. Meyer Zu Theenhausen[58a], R.P. Middleton[131], S. Miglioranzi[164a,164c], L. Mijović[21], G. Mikenberg[172], M. Mikestikova[127], M. Mikuž[75], M. Milesi[88], A. Milic[30], D.W. Miller[31], C. Mills[46], A. Milov[172], D.A. Milstead[146a,146b], A.A. Minaenko[130], Y. Minami[155], I.A. Minashvili[65], A.I. Mincer[110], B. Mindur[38a], M. Mineev[65], Y. Ming[173], L.M. Mir[12], K.P. Mistry[122], T. Mitani[171], J. Mitrevski[100], V.A. Mitsou[167], A. Miucci[49], P.S. Miyagawa[139], J.U. Mjörnmark[81], T. Moa[146a,146b], K. Mochizuki[85], S. Mohapatra[35], W. Mohr[48], S. Molander[146a,146b], R. Moles-Valls[21], R. Monden[68], K. Mönig[42], C. Monini[55], J. Monk[36], E. Monnier[85], J. Montejo Berlingen[12], F. Monticelli[71], S. Monzani[132a,132b], R.W. Moore[3], N. Morange[117], D. Moreno[162], M. Moreno Llácer[54], P. Morettini[50a], D. Mori[142], T. Mori[155], M. Morii[57], M. Morinaga[155], V. Morisbak[119], S. Moritz[83], A.K. Morley[150], G. Mornacchi[30], J.D. Morris[76], S.S. Mortensen[36], A. Morton[53], L. Morvaj[103], M. Mosidze[51b], J. Moss[143], K. Motohashi[157], R. Mount[143], E. Mountricha[25], S.V. Mouraviev[96,*], E.J.W. Moyse[86], S. Muanza[85], R.D. Mudd[18], F. Mueller[101], J. Mueller[125], R.S.P. Mueller[100], T. Mueller[28], D. Muenstermann[49], P. Mullen[53], G.A. Mullier[17], J.A. Murillo Quijada[18], W.J. Murray[170,131], H. Musheghyan[54], E. Musto[152], A.G. Myagkov[130,ab], M. Myska[128], B.P. Nachman[143], O. Nackenhorst[54], J. Nadal[54], K. Nagai[120], R. Nagai[157], Y. Nagai[85], K. Nagano[66], A. Nagarkar[111], Y. Nagasaka[59], K. Nagata[160], M. Nagel[101], E. Nagy[85], A.M. Nairz[30], Y. Nakahama[30], K. Nakamura[66], T. Nakamura[155], I. Nakano[112], H. Namasivayam[41], R.F. Naranjo Garcia[42], R. Narayan[31], D.I. Narrias Villar[58a], T. Naumann[42], G. Navarro[162], R. Nayyar[7], H.A. Neal[89], P.Yu. Nechaeva[96], T.J. Neep[84], P.D. Nef[143], A. Negri[121a,121b], M. Negrini[20a], S. Nektarijevic[106], C. Nellist[117], A. Nelson[163], S. Nemecek[127], P. Nemethy[110], A.A. Nepomuceno[24a], M. Nessi[30,ac], M.S. Neubauer[165], M. Neumann[175], R.M. Neves[110], P. Nevski[25], P.R. Newman[18], D.H. Nguyen[6], R.B. Nickerson[120], R. Nicolaidou[136], B. Nicquevert[30], J. Nielsen[137], N. Nikiforou[35], A. Nikiforov[16], V. Nikolaenko[130,ab], I. Nikolic-Audit[80], K. Nikolopoulos[18], J.K. Nilsen[119], P. Nilsson[25], Y. Ninomiya[155], A. Nisati[132a], R. Nisius[101], T. Nobe[155], M. Nomachi[118], I. Nomidis[29], T. Nooney[76], S. Norberg[113], M. Nordberg[30], O. Novgorodova[44], S. Nowak[101], M. Nozaki[66], L. Nozka[115], K. Ntekas[10], G. Nunes Hanninger[88], T. Nunnemann[100], E. Nurse[78], F. Nuti[88], B.J. O'Brien[46], F. O'grady[7], D.C. O'Neil[142], V. O'Shea[53], F.G. Oakham[29,d], H. Oberlack[101], T. Obermann[21], J. Ocariz[80], A. Ochi[67], I. Ochoa[78], J.P. Ochoa-Ricoux[32a], S. Oda[70], S. Odaka[66], H. Ogren[61], A. Oh[84], S.H. Oh[45], C.C. Ohm[15], H. Ohman[166], H. Oide[30], W. Okamura[118], H. Okawa[160], Y. Okumura[31], T. Okuyama[66], A. Olariu[26a], S.A. Olivares Pino[46], D. Oliveira Damazio[25], E. Oliver Garcia[167], A. Olszewski[39], J. Olszowska[39], A. Onofre[126a,126e], K. Onogi[103], P.U.E. Onyisi[31,r], C.J. Oram[159a], M.J. Oreglia[31], Y. Oren[153], D. Orestano[134a,134b], N. Orlando[154], C. Oropeza Barrera[53], R.S. Orr[158], B. Osculati[50a,50b], R. Ospanov[84], G. Otero y Garzon[27], H. Otono[70], M. Ouchrif[135d], F. Ould-Saada[119], A. Ouraou[136], K.P. Oussoren[107], Q. Ouyang[33a], A. Ovcharova[15], M. Owen[53], R.E. Owen[18], V.E. Ozcan[19a], N. Ozturk[8], K. Pachal[142], A. Pacheco Pages[12], C. Padilla Aranda[12], M. Pagáčová[48], S. Pagan Griso[15], E. Paganis[139], F. Paige[25], P. Pais[86], K. Pajchel[119], G. Palacino[159b], S. Palestini[30], M. Palka[38b], D. Pallin[34], A. Palma[126a,126b], Y.B. Pan[173], E. Panagiotopoulou[10], C.E. Pandini[80], J.G. Panduro Vazquez[77], P. Pani[146a,146b], S. Panitkin[25], D. Pantea[26a], L. Paolozzi[49],

Th.D. Papadopoulou[10], K. Papageorgiou[154], A. Paramonov[6], D. Paredes Hernandez[154], M.A. Parker[28], K.A. Parker[139], F. Parodi[50a,50b], J.A. Parsons[35], U. Parzefall[48], E. Pasqualucci[132a], S. Passaggio[50a], F. Pastore[134a,134b,*], Fr. Pastore[77], G. Pásztor[29], S. Pataraia[175], N.D. Patel[150], J.R. Pater[84], T. Pauly[30], J. Pearce[169], B. Pearson[113], L.E. Pedersen[36], M. Pedersen[119], S. Pedraza Lopez[167], R. Pedro[126a,126b], S.V. Peleganchuk[109,c], D. Pelikan[166], O. Penc[127], C. Peng[33a], H. Peng[33b], B. Penning[31], J. Penwell[61], D.V. Perepelitsa[25], E. Perez Codina[159a], M.T. Pérez García-Estañ[167], L. Perini[91a,91b], H. Pernegger[30], S. Perrella[104a,104b], R. Peschke[42], V.D. Peshekhonov[65], K. Peters[30], R.F.Y. Peters[84], B.A. Petersen[30], T.C. Petersen[36], E. Petit[42], A. Petridis[1], C. Petridou[154], P. Petroff[117], E. Petrolo[132a], F. Petrucci[134a,134b], N.E. Pettersson[157], R. Pezoa[32b], P.W. Phillips[131], G. Piacquadio[143], E. Pianori[170], A. Picazio[49], E. Piccaro[76], M. Piccinini[20a,20b], M.A. Pickering[120], R. Piegaia[27], D.T. Pignotti[111], J.E. Pilcher[31], A.D. Pilkington[84], J. Pina[126a,126b,126d], M. Pinamonti[164a,164c,ad], J.L. Pinfold[3], A. Pingel[36], S. Pires[80], H. Pirumov[42], M. Pitt[172], C. Pizio[91a,91b], L. Plazak[144a], M.-A. Pleier[25], V. Pleskot[129], E. Plotnikova[65], P. Plucinski[146a,146b], D. Pluth[64], R. Poettgen[146a,146b], L. Poggioli[117], D. Pohl[21], G. Polesello[121a], A. Poley[42], A. Policicchio[37a,37b], R. Polifka[158], A. Polini[20a], C.S. Pollard[53], V. Polychronakos[25], K. Pommès[30], L. Pontecorvo[132a], B.G. Pope[90], G.A. Popeneciu[26b], D.S. Popovic[13], A. Poppleton[30], S. Pospisil[128], K. Potamianos[15], I.N. Potrap[65], C.J. Potter[149], C.T. Potter[116], G. Poulard[30], J. Poveda[30], V. Pozdnyakov[65], P. Pralavorio[85], A. Pranko[15], S. Prasad[30], S. Prell[64], D. Price[84], L.E. Price[6], M. Primavera[73a], S. Prince[87], M. Proissl[46], K. Prokofiev[60c], F. Prokoshin[32b], E. Protopapadaki[136], S. Protopopescu[25], J. Proudfoot[6], M. Przybycien[38a], E. Ptacek[116], D. Puddu[134a,134b], E. Pueschel[86], D. Puldon[148], M. Purohit[25,ae], P. Puzo[117], J. Qian[89], G. Qin[53], Y. Qin[84], A. Quadt[54], D.R. Quarrie[15], W.B. Quayle[164a,164b], M. Queitsch-Maitland[84], D. Quilty[53], S. Raddum[119], V. Radeka[25], V. Radescu[42], S.K. Radhakrishnan[148], P. Radloff[116], P. Rados[88], F. Ragusa[91a,91b], G. Rahal[178], S. Rajagopalan[25], M. Rammensee[30], C. Rangel-Smith[166], F. Rauscher[100], S. Rave[83], T. Ravenscroft[53], M. Raymond[30], A.L. Read[119], N.P. Readioff[74], D.M. Rebuzzi[121a,121b], A. Redelbach[174], G. Redlinger[25], R. Reece[137], K. Reeves[41], L. Rehnisch[16], J. Reichert[122], H. Reisin[27], M. Relich[163], C. Rembser[30], H. Ren[33a], A. Renaud[117], M. Rescigno[132a], S. Resconi[91a], O.L. Rezanova[109,c], P. Reznicek[129], R. Rezvani[95], R. Richter[101], S. Richter[78], E. Richter-Was[38b], O. Ricken[21], M. Ridel[80], P. Rieck[16], C.J. Riegel[175], J. Rieger[54], O. Rifki[113], M. Rijssenbeek[148], A. Rimoldi[121a,121b], L. Rinaldi[20a], B. Ristić[49], E. Ritsch[30], I. Riu[12], F. Rizatdinova[114], E. Rizvi[76], S.H. Robertson[87,k], A. Robichaud-Veronneau[87], D. Robinson[28], J.E.M. Robinson[42], A. Robson[53], C. Roda[124a,124b], S. Roe[30], O. Røhne[119], S. Rolli[161], A. Romaniouk[98], M. Romano[20a,20b], S.M. Romano Saez[34], E. Romero Adam[167], N. Rompotis[138], M. Ronzani[48], L. Roos[80], E. Ros[167], S. Rosati[132a], K. Rosbach[48], P. Rose[137], P.L. Rosendahl[14], O. Rosenthal[141], V. Rossetti[146a,146b], E. Rossi[104a,104b], L.P. Rossi[50a], J.H.N. Rosten[28], R. Rosten[138], M. Rotaru[26a], I. Roth[172], J. Rothberg[138], D. Rousseau[117], C.R. Royon[136], A. Rozanov[85], Y. Rozen[152], X. Ruan[145c], F. Rubbo[143], I. Rubinskiy[42], V.I. Rud[99], C. Rudolph[44], M.S. Rudolph[158], F. Rühr[48], A. Ruiz-Martinez[30], Z. Rurikova[48], N.A. Rusakovich[65], A. Ruschke[100], H.L. Russell[138], J.P. Rutherfoord[7], N. Ruthmann[48], Y.F. Ryabov[123], M. Rybar[165], G. Rybkin[117], N.C. Ryder[120], A.F. Saavedra[150], G. Sabato[107], S. Sacerdoti[27], A. Saddique[3], H.F-W. Sadrozinski[137], R. Sadykov[65], F. Safai Tehrani[132a], M. Sahinsoy[58a], M. Saimpert[136], T. Saito[155], H. Sakamoto[155], Y. Sakurai[171], G. Salamanna[134a,134b], A. Salamon[133a], J.E. Salazar Loyola[32b], M. Saleem[113], D. Salek[107], P.H. Sales De Bruin[138], D. Salihagic[101], A. Salnikov[143], J. Salt[167], D. Salvatore[37a,37b], F. Salvatore[149], A. Salvucci[60a], A. Salzburger[30], D. Sammel[48], D. Sampsonidis[154], A. Sanchez[104a,104b], J. Sánchez[167], V. Sanchez Martinez[167], H. Sandaker[119], R.L. Sandbach[76], H.G. Sander[83], M.P. Sanders[100], M. Sandhoff[175], C. Sandoval[162], R. Sandstroem[101], D.P.C. Sankey[131], M. Sannino[50a,50b], A. Sansoni[47], C. Santoni[34], R. Santonico[133a,133b],

H. Santos[126a], I. Santoyo Castillo[149], K. Sapp[125], A. Sapronov[65], J.G. Saraiva[126a,126d], B. Sarrazin[21], O. Sasaki[66], Y. Sasaki[155], K. Sato[160], G. Sauvage[5,*], E. Sauvan[5], G. Savage[77], P. Savard[158,d], C. Sawyer[131], L. Sawyer[79,n], J. Saxon[31], C. Sbarra[20a], A. Sbrizzi[20a,20b], T. Scanlon[78], D.A. Scannicchio[163], M. Scarcella[150], V. Scarfone[37a,37b], J. Schaarschmidt[172], P. Schacht[101], D. Schaefer[30], R. Schaefer[42], J. Schaeffer[83], S. Schaepe[21], S. Schaetzel[58b], U. Schäfer[83], A.C. Schaffer[117], D. Schaile[100], R.D. Schamberger[148], V. Scharf[58a], V.A. Schegelsky[123], D. Scheirich[129], M. Schernau[163], C. Schiavi[50a,50b], C. Schillo[48], M. Schioppa[37a,37b], S. Schlenker[30], K. Schmieden[30], C. Schmitt[83], S. Schmitt[58b], S. Schmitt[42], B. Schneider[159a], Y.J. Schnellbach[74], U. Schnoor[44], L. Schoeffel[136], A. Schoening[58b], B.D. Schoenrock[90], E. Schopf[21], A.L.S. Schorlemmer[54], M. Schott[83], D. Schouten[159a], J. Schovancova[8], S. Schramm[49], M. Schreyer[174], C. Schroeder[83], N. Schuh[83], M.J. Schultens[21], H.-C. Schultz-Coulon[58a], H. Schulz[16], M. Schumacher[48], B.A. Schumm[137], Ph. Schune[136], C. Schwanenberger[84], A. Schwartzman[143], T.A. Schwarz[89], Ph. Schwegler[101], H. Schweiger[84], Ph. Schwemling[136], R. Schwienhorst[90], J. Schwindling[136], T. Schwindt[21], F.G. Sciacca[17], E. Scifo[117], G. Sciolla[23], F. Scuri[124a,124b], F. Scutti[21], J. Searcy[89], G. Sedov[42], E. Sedykh[123], P. Seema[21], S.C. Seidel[105], A. Seiden[137], F. Seifert[128], J.M. Seixas[24a], G. Sekhniaidze[104a], K. Sekhon[89], S.J. Sekula[40], D.M. Seliverstov[123,*], N. Semprini-Cesari[20a,20b], C. Serfon[30], L. Serin[117], L. Serkin[164a,164b], T. Serre[85], M. Sessa[134a,134b], R. Seuster[159a], H. Severini[113], T. Sfiligoj[75], F. Sforza[30], A. Sfyrla[30], E. Shabalina[54], M. Shamim[116], L.Y. Shan[33a], R. Shang[165], J.T. Shank[22], M. Shapiro[15], P.B. Shatalov[97], K. Shaw[164a,164b], S.M. Shaw[84], A. Shcherbakova[146a,146b], C.Y. Shehu[149], P. Sherwood[78], L. Shi[151,af], S. Shimizu[67], C.O. Shimmin[163], M. Shimojima[102], M. Shiyakova[65], A. Shmeleva[96], D. Shoaleh Saadi[95], M.J. Shochet[31], S. Shojaii[91a,91b], S. Shrestha[111], E. Shulga[98], M.A. Shupe[7], S. Shushkevich[42], P. Sicho[127], P.E. Sidebo[147], O. Sidiropoulou[174], D. Sidorov[114], A. Sidoti[20a,20b], F. Siegert[44], Dj. Sijacki[13], J. Silva[126a,126d], Y. Silver[153], S.B. Silverstein[146a], V. Simak[128], O. Simard[5], Lj. Simic[13], S. Simion[117], E. Simioni[83], B. Simmons[78], D. Simon[34], P. Sinervo[158], N.B. Sinev[116], M. Sioli[20a,20b], G. Siragusa[174], A.N. Sisakyan[65,*], S.Yu. Sivoklokov[99], J. Sjölin[146a,146b], T.B. Sjursen[14], M.B. Skinner[72], H.P. Skottowe[57], P. Skubic[113], M. Slater[18], T. Slavicek[128], M. Slawinska[107], K. Sliwa[161], V. Smakhtin[172], B.H. Smart[46], L. Smestad[14], S.Yu. Smirnov[98], Y. Smirnov[98], L.N. Smirnova[99,ag], O. Smirnova[81], M.N.K. Smith[35], R.W. Smith[35], M. Smizanska[72], K. Smolek[128], A.A. Snesarev[96], G. Snidero[76], S. Snyder[25], R. Sobie[169,k], F. Socher[44], A. Soffer[153], D.A. Soh[151,af], G. Sokhrannyi[75], C.A. Solans[30], M. Solar[128], J. Solc[128], E.Yu. Soldatov[98], U. Soldevila[167], A.A. Solodkov[130], A. Soloshenko[65], O.V. Solovyanov[130], V. Solovyev[123], P. Sommer[48], H.Y. Song[33b], N. Soni[1], A. Sood[15], A. Sopczak[128], B. Sopko[128], V. Sopko[128], V. Sorin[12], D. Sosa[58b], M. Sosebee[8], C.L. Sotiropoulou[124a,124b], R. Soualah[164a,164c], A.M. Soukharev[109,c], D. South[42], B.C. Sowden[77], S. Spagnolo[73a,73b], M. Spalla[124a,124b], M. Spangenberg[170], F. Spanò[77], W.R. Spearman[57], D. Sperlich[16], F. Spettel[101], R. Spighi[20a], G. Spigo[30], L.A. Spiller[88], M. Spousta[129], T. Spreitzer[158], R.D. St. Denis[53,*], A. Stabile[91a], S. Staerz[44], J. Stahlman[122], R. Stamen[58a], S. Stamm[16], E. Stanecka[39], C. Stanescu[134a], M. Stanescu-Bellu[42], M.M. Stanitzki[42], S. Stapnes[119], E.A. Starchenko[130], J. Stark[55], P. Staroba[127], P. Starovoitov[58a], R. Staszewski[39], P. Steinberg[25], B. Stelzer[142], H.J. Stelzer[30], O. Stelzer-Chilton[159a], H. Stenzel[52], G.A. Stewart[53], J.A. Stillings[21], M.C. Stockton[87], M. Stoebe[87], G. Stoicea[26a], P. Stolte[54], S. Stonjek[101], A.R. Stradling[8], A. Straessner[44], M.E. Stramaglia[17], J. Strandberg[147], S. Strandberg[146a,146b], A. Strandlie[119], E. Strauss[143], M. Strauss[113], P. Strizenec[144b], R. Ströhmer[174], D.M. Strom[116], R. Stroynowski[40], A. Strubig[106], S.A. Stucci[17], B. Stugu[14], N.A. Styles[42], D. Su[143], J. Su[125], R. Subramaniam[79], A. Succurro[12], Y. Sugaya[118], M. Suk[128], V.V. Sulin[96], S. Sultansoy[4c], T. Sumida[68], S. Sun[57], X. Sun[33a], J.E. Sundermann[48], K. Suruliz[149], G. Susinno[37a,37b], M.R. Sutton[149],

S. Suzuki[66], M. Svatos[127], M. Swiatlowski[143], I. Sykora[144a], T. Sykora[129], D. Ta[48], C. Taccini[134a,134b], K. Tackmann[42], J. Taenzer[158], A. Taffard[163], R. Tafirout[159a], N. Taiblum[153], H. Takai[25], R. Takashima[69], H. Takeda[67], T. Takeshita[140], Y. Takubo[66], M. Talby[85], A.A. Talyshev[109,c], J.Y.C. Tam[174], K.G. Tan[88], J. Tanaka[155], R. Tanaka[117], S. Tanaka[66], B.B. Tannenwald[111], N. Tannoury[21], S. Tapprogge[83], S. Tarem[152], F. Tarrade[29], G.F. Tartarelli[91a], P. Tas[129], M. Tasevsky[127], T. Tashiro[68], E. Tassi[37a,37b], A. Tavares Delgado[126a,126b], Y. Tayalati[135d], F.E. Taylor[94], G.N. Taylor[88], P.T.E. Taylor[88], W. Taylor[159b], F.A. Teischinger[30], M. Teixeira Dias Castanheira[76], P. Teixeira-Dias[77], K.K. Temming[48], D. Temple[142], H. Ten Kate[30], P.K. Teng[151], J.J. Teoh[118], F. Tepel[175], S. Terada[66], K. Terashi[155], J. Terron[82], S. Terzo[101], M. Testa[47], R.J. Teuscher[158,k], T. Theveneaux-Pelzer[34], J.P. Thomas[18], J. Thomas-Wilsker[77], E.N. Thompson[35], P.D. Thompson[18], R.J. Thompson[84], A.S. Thompson[53], L.A. Thomsen[176], E. Thomson[122], M. Thomson[28], R.P. Thun[89,*], M.J. Tibbetts[15], R.E. Ticse Torres[85], V.O. Tikhomirov[96,ah], Yu.A. Tikhonov[109,c], S. Timoshenko[98], E. Tiouchichine[85], P. Tipton[176], S. Tisserant[85], K. Todome[157], T. Todorov[5,*], S. Todorova-Nova[129], J. Tojo[70], S. Tokár[144a], K. Tokushuku[66], K. Tollefson[90], E. Tolley[57], L. Tomlinson[84], M. Tomoto[103], L. Tompkins[143,ai], K. Toms[105], E. Torrence[116], H. Torres[142], E. Torró Pastor[138], J. Toth[85,aj], F. Touchard[85], D.R. Tovey[139], T. Trefzger[174], L. Tremblet[30], A. Tricoli[30], I.M. Trigger[159a], S. Trincaz-Duvoid[80], M.F. Tripiana[12], W. Trischuk[158], B. Trocmé[55], C. Troncon[91a], M. Trottier-McDonald[15], M. Trovatelli[169], L. Truong[164a,164c], M. Trzebinski[39], A. Trzupek[39], C. Tsarouchas[30], J.C-L. Tseng[120], P.V. Tsiareshka[92], D. Tsionou[154], G. Tsipolitis[10], N. Tsirintanis[9], S. Tsiskaridze[12], V. Tsiskaridze[48], E.G. Tskhadadze[51a], I.I. Tsukerman[97], V. Tsulaia[15], S. Tsuno[66], D. Tsybychev[148], A. Tudorache[26a], V. Tudorache[26a], A.N. Tuna[57], S.A. Tupputi[20a,20b], S. Turchikhin[99,ag], D. Turecek[128], R. Turra[91a,91b], A.J. Turvey[40], P.M. Tuts[35], A. Tykhonov[49], M. Tylmad[146a,146b], M. Tyndel[131], I. Ueda[155], R. Ueno[29], M. Ughetto[146a,146b], M. Ugland[14], F. Ukegawa[160], G. Unal[30], A. Undrus[25], G. Unel[163], F.C. Ungaro[48], Y. Unno[66], C. Unverdorben[100], J. Urban[144b], P. Urquijo[88], P. Urrejola[83], G. Usai[8], A. Usanova[62], L. Vacavant[85], V. Vacek[128], B. Vachon[87], C. Valderanis[83], N. Valencic[107], S. Valentinetti[20a,20b], A. Valero[167], L. Valery[12], S. Valkar[129], E. Valladolid Gallego[167], S. Vallecorsa[49], J.A. Valls Ferrer[167], W. Van Den Wollenberg[107], P.C. Van Der Deijl[107], R. van der Geer[107], H. van der Graaf[107], N. van Eldik[152], P. van Gemmeren[6], J. Van Nieuwkoop[142], I. van Vulpen[107], M.C. van Woerden[30], M. Vanadia[132a,132b], W. Vandelli[30], R. Vanguri[122], A. Vaniachine[6], F. Vannucci[80], G. Vardanyan[177], R. Vari[132a], E.W. Varnes[7], T. Varol[40], D. Varouchas[80], A. Vartapetian[8], K.E. Varvell[150], F. Vazeille[34], T. Vazquez Schroeder[87], J. Veatch[7], L.M. Veloce[158], F. Veloso[126a,126c], T. Velz[21], S. Veneziano[132a], A. Ventura[73a,73b], D. Ventura[86], M. Venturi[169], N. Venturi[158], A. Venturini[23], V. Vercesi[121a], M. Verducci[132a,132b], W. Verkerke[107], J.C. Vermeulen[107], A. Vest[44], M.C. Vetterli[142,d], O. Viazlo[81], I. Vichou[165], T. Vickey[139], O.E. Vickey Boeriu[139], G.H.A. Viehhauser[120], S. Viel[15], R. Vigne[62], M. Villa[20a,20b], M. Villaplana Perez[91a,91b], E. Vilucchi[47], M.G. Vincter[29], V.B. Vinogradov[65], I. Vivarelli[149], F. Vives Vaque[3], S. Vlachos[10], D. Vladoiu[100], M. Vlasak[128], M. Vogel[32a], P. Vokac[128], G. Volpi[124a,124b], M. Volpi[88], H. von der Schmitt[101], H. von Radziewski[48], E. von Toerne[21], V. Vorobel[129], K. Vorobev[98], M. Vos[167], R. Voss[30], J.H. Vossebeld[74], N. Vranjes[13], M. Vranjes Milosavljevic[13], V. Vrba[127], M. Vreeswijk[107], R. Vuillermet[30], I. Vukotic[31], Z. Vykydal[128], P. Wagner[21], W. Wagner[175], H. Wahlberg[71], S. Wahrmund[44], J. Wakabayashi[103], J. Walder[72], R. Walker[100], W. Walkowiak[141], C. Wang[151], F. Wang[173], H. Wang[15], H. Wang[40], J. Wang[42], J. Wang[33a], K. Wang[87], R. Wang[6], S.M. Wang[151], T. Wang[21], T. Wang[35], X. Wang[176], C. Wanotayaroj[116], A. Warburton[87], C.P. Ward[28], D.R. Wardrope[78], A. Washbrook[46], C. Wasicki[42], P.M. Watkins[18], A.T. Watson[18], I.J. Watson[150], M.F. Watson[18], G. Watts[138], S. Watts[84], B.M. Waugh[78], S. Webb[84],

M.S. Weber[17], S.W. Weber[174], J.S. Webster[31], A.R. Weidberg[120], B. Weinert[61], J. Weingarten[54], C. Weiser[48], H. Weits[107], P.S. Wells[30], T. Wenaus[25], T. Wengler[30], S. Wenig[30], N. Wermes[21], M. Werner[48], P. Werner[30], M. Wessels[58a], J. Wetter[161], K. Whalen[116], A.M. Wharton[72], A. White[8], M.J. White[1], R. White[32b], S. White[124a,124b], D. Whiteson[163], F.J. Wickens[131], W. Wiedenmann[173], M. Wielers[131], P. Wienemann[21], C. Wiglesworth[36], L.A.M. Wiik-Fuchs[21], A. Wildauer[101], H.G. Wilkens[30], H.H. Williams[122], S. Williams[107], C. Willis[90], S. Willocq[86], A. Wilson[89], J.A. Wilson[18], I. Wingerter-Seez[5], F. Winklmeier[116], B.T. Winter[21], M. Wittgen[143], J. Wittkowski[100], S.J. Wollstadt[83], M.W. Wolter[39], H. Wolters[126a,126c], B.K. Wosiek[39], J. Wotschack[30], M.J. Woudstra[84], K.W. Wozniak[39], M. Wu[55], M. Wu[31], S.L. Wu[173], X. Wu[49], Y. Wu[89], T.R. Wyatt[84], B.M. Wynne[46], S. Xella[36], D. Xu[33a], L. Xu[25], B. Yabsley[150], S. Yacoob[145a], R. Yakabe[67], M. Yamada[66], D. Yamaguchi[157], Y. Yamaguchi[118], A. Yamamoto[66], S. Yamamoto[155], T. Yamanaka[155], K. Yamauchi[103], Y. Yamazaki[67], Z. Yan[22], H. Yang[33e], H. Yang[173], Y. Yang[151], W-M. Yao[15], Y. Yasu[66], E. Yatsenko[5], K.H. Yau Wong[21], J. Ye[40], S. Ye[25], I. Yeletskikh[65], A.L. Yen[57], E. Yildirim[42], K. Yorita[171], R. Yoshida[6], K. Yoshihara[122], C. Young[143], C.J.S. Young[30], S. Youssef[22], D.R. Yu[15], J. Yu[8], J.M. Yu[89], J. Yu[114], L. Yuan[67], S.P.Y. Yuen[21], A. Yurkewicz[108], I. Yusuff[28,*ak*], B. Zabinski[39], R. Zaidan[63], A.M. Zaitsev[130,*ab*], J. Zalieckas[14], A. Zaman[148], S. Zambito[57], L. Zanello[132a,132b], D. Zanzi[88], C. Zeitnitz[175], M. Zeman[128], A. Zemla[38a], Q. Zeng[143], K. Zengel[23], O. Zenin[130], T. Ženiš[144a], D. Zerwas[117], D. Zhang[89], F. Zhang[173], H. Zhang[33c], J. Zhang[6], L. Zhang[48], R. Zhang[33b], X. Zhang[33d], Z. Zhang[117], X. Zhao[40], Y. Zhao[33d,117], Z. Zhao[33b], A. Zhemchugov[65], J. Zhong[120], B. Zhou[89], C. Zhou[45], L. Zhou[35], L. Zhou[40], M. Zhou[148], N. Zhou[33f], C.G. Zhu[33d], H. Zhu[33a], J. Zhu[89], Y. Zhu[33b], X. Zhuang[33a], K. Zhukov[96], A. Zibell[174], D. Zieminska[61], N.I. Zimine[65], C. Zimmermann[83], S. Zimmermann[48], Z. Zinonos[54], M. Zinser[83], M. Ziolkowski[141], L. Živković[13], G. Zobernig[173], A. Zoccoli[20a,20b], M. zur Nedden[16], G. Zurzolo[104a,104b], L. Zwalinski[30].

[1] Department of Physics, University of Adelaide, Adelaide, Australia
[2] Physics Department, SUNY Albany, Albany NY, United States of America
[3] Department of Physics, University of Alberta, Edmonton AB, Canada
[4] [(a)] Department of Physics, Ankara University, Ankara; [(b)] Istanbul Aydin University, Istanbul; [(c)] Division of Physics, TOBB University of Economics and Technology, Ankara, Turkey
[5] LAPP, CNRS/IN2P3 and Université Savoie Mont Blanc, Annecy-le-Vieux, France
[6] High Energy Physics Division, Argonne National Laboratory, Argonne IL, United States of America
[7] Department of Physics, University of Arizona, Tucson AZ, United States of America
[8] Department of Physics, The University of Texas at Arlington, Arlington TX, United States of America
[9] Physics Department, University of Athens, Athens, Greece
[10] Physics Department, National Technical University of Athens, Zografou, Greece
[11] Institute of Physics, Azerbaijan Academy of Sciences, Baku, Azerbaijan
[12] Institut de Física d'Altes Energies and Departament de Física de la Universitat Autònoma de Barcelona, Barcelona, Spain
[13] Institute of Physics, University of Belgrade, Belgrade, Serbia
[14] Department for Physics and Technology, University of Bergen, Bergen, Norway
[15] Physics Division, Lawrence Berkeley National Laboratory and University of California, Berkeley CA, United States of America
[16] Department of Physics, Humboldt University, Berlin, Germany
[17] Albert Einstein Center for Fundamental Physics and Laboratory for High Energy Physics, University

of Bern, Bern, Switzerland
[18] School of Physics and Astronomy, University of Birmingham, Birmingham, United Kingdom
[19] [(a)] Department of Physics, Bogazici University, Istanbul; [(b)] Department of Physics Engineering, Gaziantep University, Gaziantep; [(c)] Department of Physics, Dogus University, Istanbul, Turkey
[20] [(a)] INFN Sezione di Bologna; [(b)] Dipartimento di Fisica e Astronomia, Università di Bologna, Bologna, Italy
[21] Physikalisches Institut, University of Bonn, Bonn, Germany
[22] Department of Physics, Boston University, Boston MA, United States of America
[23] Department of Physics, Brandeis University, Waltham MA, United States of America
[24] [(a)] Universidade Federal do Rio De Janeiro COPPE/EE/IF, Rio de Janeiro; [(b)] Electrical Circuits Department, Federal University of Juiz de Fora (UFJF), Juiz de Fora; [(c)] Federal University of Sao Joao del Rei (UFSJ), Sao Joao del Rei; [(d)] Instituto de Fisica, Universidade de Sao Paulo, Sao Paulo, Brazil
[25] Physics Department, Brookhaven National Laboratory, Upton NY, United States of America
[26] [(a)] National Institute of Physics and Nuclear Engineering, Bucharest; [(b)] National Institute for Research and Development of Isotopic and Molecular Technologies, Physics Department, Cluj Napoca; [(c)] University Politehnica Bucharest, Bucharest; [(d)] West University in Timisoara, Timisoara, Romania
[27] Departamento de Física, Universidad de Buenos Aires, Buenos Aires, Argentina
[28] Cavendish Laboratory, University of Cambridge, Cambridge, United Kingdom
[29] Department of Physics, Carleton University, Ottawa ON, Canada
[30] CERN, Geneva, Switzerland
[31] Enrico Fermi Institute, University of Chicago, Chicago IL, United States of America
[32] [(a)] Departamento de Física, Pontificia Universidad Católica de Chile, Santiago; [(b)] Departamento de Física, Universidad Técnica Federico Santa María, Valparaíso, Chile
[33] [(a)] Institute of High Energy Physics, Chinese Academy of Sciences, Beijing; [(b)] Department of Modern Physics, University of Science and Technology of China, Anhui; [(c)] Department of Physics, Nanjing University, Jiangsu; [(d)] School of Physics, Shandong University, Shandong; [(e)] Department of Physics and Astronomy, Shanghai Key Laboratory for Particle Physics and Cosmology, Shanghai Jiao Tong University, Shanghai; [(f)] Physics Department, Tsinghua University, Beijing 100084, China
[34] Laboratoire de Physique Corpusculaire, Clermont Université and Université Blaise Pascal and CNRS/IN2P3, Clermont-Ferrand, France
[35] Nevis Laboratory, Columbia University, Irvington NY, United States of America
[36] Niels Bohr Institute, University of Copenhagen, Kobenhavn, Denmark
[37] [(a)] INFN Gruppo Collegato di Cosenza, Laboratori Nazionali di Frascati; [(b)] Dipartimento di Fisica, Università della Calabria, Rende, Italy
[38] [(a)] AGH University of Science and Technology, Faculty of Physics and Applied Computer Science, Krakow; [(b)] Marian Smoluchowski Institute of Physics, Jagiellonian University, Krakow, Poland
[39] Institute of Nuclear Physics Polish Academy of Sciences, Krakow, Poland
[40] Physics Department, Southern Methodist University, Dallas TX, United States of America
[41] Physics Department, University of Texas at Dallas, Richardson TX, United States of America
[42] DESY, Hamburg and Zeuthen, Germany
[43] Institut für Experimentelle Physik IV, Technische Universität Dortmund, Dortmund, Germany
[44] Institut für Kern- und Teilchenphysik, Technische Universität Dresden, Dresden, Germany
[45] Department of Physics, Duke University, Durham NC, United States of America
[46] SUPA - School of Physics and Astronomy, University of Edinburgh, Edinburgh, United Kingdom

[47] INFN Laboratori Nazionali di Frascati, Frascati, Italy
[48] Fakultät für Mathematik und Physik, Albert-Ludwigs-Universität, Freiburg, Germany
[49] Section de Physique, Université de Genève, Geneva, Switzerland
[50] [(a)] INFN Sezione di Genova; [(b)] Dipartimento di Fisica, Università di Genova, Genova, Italy
[51] [(a)] E. Andronikashvili Institute of Physics, Iv. Javakhishvili Tbilisi State University, Tbilisi; [(b)] High Energy Physics Institute, Tbilisi State University, Tbilisi, Georgia
[52] II Physikalisches Institut, Justus-Liebig-Universität Giessen, Giessen, Germany
[53] SUPA - School of Physics and Astronomy, University of Glasgow, Glasgow, United Kingdom
[54] II Physikalisches Institut, Georg-August-Universität, Göttingen, Germany
[55] Laboratoire de Physique Subatomique et de Cosmologie, Université Grenoble-Alpes, CNRS/IN2P3, Grenoble, France
[56] Department of Physics, Hampton University, Hampton VA, United States of America
[57] Laboratory for Particle Physics and Cosmology, Harvard University, Cambridge MA, United States of America
[58] [(a)] Kirchhoff-Institut für Physik, Ruprecht-Karls-Universität Heidelberg, Heidelberg; [(b)] Physikalisches Institut, Ruprecht-Karls-Universität Heidelberg, Heidelberg; [(c)] ZITI Institut für technische Informatik, Ruprecht-Karls-Universität Heidelberg, Mannheim, Germany
[59] Faculty of Applied Information Science, Hiroshima Institute of Technology, Hiroshima, Japan
[60] [(a)] Department of Physics, The Chinese University of Hong Kong, Shatin, N.T., Hong Kong; [(b)] Department of Physics, The University of Hong Kong, Hong Kong; [(c)] Department of Physics, The Hong Kong University of Science and Technology, Clear Water Bay, Kowloon, Hong Kong, China
[61] Department of Physics, Indiana University, Bloomington IN, United States of America
[62] Institut für Astro- und Teilchenphysik, Leopold-Franzens-Universität, Innsbruck, Austria
[63] University of Iowa, Iowa City IA, United States of America
[64] Department of Physics and Astronomy, Iowa State University, Ames IA, United States of America
[65] Joint Institute for Nuclear Research, JINR Dubna, Dubna, Russia
[66] KEK, High Energy Accelerator Research Organization, Tsukuba, Japan
[67] Graduate School of Science, Kobe University, Kobe, Japan
[68] Faculty of Science, Kyoto University, Kyoto, Japan
[69] Kyoto University of Education, Kyoto, Japan
[70] Department of Physics, Kyushu University, Fukuoka, Japan
[71] Instituto de Física La Plata, Universidad Nacional de La Plata and CONICET, La Plata, Argentina
[72] Physics Department, Lancaster University, Lancaster, United Kingdom
[73] [(a)] INFN Sezione di Lecce; [(b)] Dipartimento di Matematica e Fisica, Università del Salento, Lecce, Italy
[74] Oliver Lodge Laboratory, University of Liverpool, Liverpool, United Kingdom
[75] Department of Physics, Jožef Stefan Institute and University of Ljubljana, Ljubljana, Slovenia
[76] School of Physics and Astronomy, Queen Mary University of London, London, United Kingdom
[77] Department of Physics, Royal Holloway University of London, Surrey, United Kingdom
[78] Department of Physics and Astronomy, University College London, London, United Kingdom
[79] Louisiana Tech University, Ruston LA, United States of America
[80] Laboratoire de Physique Nucléaire et de Hautes Energies, UPMC and Université Paris-Diderot and CNRS/IN2P3, Paris, France
[81] Fysiska institutionen, Lunds universitet, Lund, Sweden

[82] Departamento de Fisica Teorica C-15, Universidad Autonoma de Madrid, Madrid, Spain
[83] Institut für Physik, Universität Mainz, Mainz, Germany
[84] School of Physics and Astronomy, University of Manchester, Manchester, United Kingdom
[85] CPPM, Aix-Marseille Université and CNRS/IN2P3, Marseille, France
[86] Department of Physics, University of Massachusetts, Amherst MA, United States of America
[87] Department of Physics, McGill University, Montreal QC, Canada
[88] School of Physics, University of Melbourne, Victoria, Australia
[89] Department of Physics, The University of Michigan, Ann Arbor MI, United States of America
[90] Department of Physics and Astronomy, Michigan State University, East Lansing MI, United States of America
[91] [(a)] INFN Sezione di Milano; [(b)] Dipartimento di Fisica, Università di Milano, Milano, Italy
[92] B.I. Stepanov Institute of Physics, National Academy of Sciences of Belarus, Minsk, Republic of Belarus
[93] National Scientific and Educational Centre for Particle and High Energy Physics, Minsk, Republic of Belarus
[94] Department of Physics, Massachusetts Institute of Technology, Cambridge MA, United States of America
[95] Group of Particle Physics, University of Montreal, Montreal QC, Canada
[96] P.N. Lebedev Institute of Physics, Academy of Sciences, Moscow, Russia
[97] Institute for Theoretical and Experimental Physics (ITEP), Moscow, Russia
[98] National Research Nuclear University MEPhI, Moscow, Russia
[99] D.V. Skobeltsyn Institute of Nuclear Physics, M.V. Lomonosov Moscow State University, Moscow, Russia
[100] Fakultät für Physik, Ludwig-Maximilians-Universität München, München, Germany
[101] Max-Planck-Institut für Physik (Werner-Heisenberg-Institut), München, Germany
[102] Nagasaki Institute of Applied Science, Nagasaki, Japan
[103] Graduate School of Science and Kobayashi-Maskawa Institute, Nagoya University, Nagoya, Japan
[104] [(a)] INFN Sezione di Napoli; [(b)] Dipartimento di Fisica, Università di Napoli, Napoli, Italy
[105] Department of Physics and Astronomy, University of New Mexico, Albuquerque NM, United States of America
[106] Institute for Mathematics, Astrophysics and Particle Physics, Radboud University Nijmegen/Nikhef, Nijmegen, Netherlands
[107] Nikhef National Institute for Subatomic Physics and University of Amsterdam, Amsterdam, Netherlands
[108] Department of Physics, Northern Illinois University, DeKalb IL, United States of America
[109] Budker Institute of Nuclear Physics, SB RAS, Novosibirsk, Russia
[110] Department of Physics, New York University, New York NY, United States of America
[111] Ohio State University, Columbus OH, United States of America
[112] Faculty of Science, Okayama University, Okayama, Japan
[113] Homer L. Dodge Department of Physics and Astronomy, University of Oklahoma, Norman OK, United States of America
[114] Department of Physics, Oklahoma State University, Stillwater OK, United States of America
[115] Palacký University, RCPTM, Olomouc, Czech Republic
[116] Center for High Energy Physics, University of Oregon, Eugene OR, United States of America

[117] LAL, Université Paris-Sud and CNRS/IN2P3, Orsay, France
[118] Graduate School of Science, Osaka University, Osaka, Japan
[119] Department of Physics, University of Oslo, Oslo, Norway
[120] Department of Physics, Oxford University, Oxford, United Kingdom
[121] [(a)] INFN Sezione di Pavia; [(b)] Dipartimento di Fisica, Università di Pavia, Pavia, Italy
[122] Department of Physics, University of Pennsylvania, Philadelphia PA, United States of America
[123] National Research Centre "Kurchatov Institute" B.P.Konstantinov Petersburg Nuclear Physics Institute, St. Petersburg, Russia
[124] [(a)] INFN Sezione di Pisa; [(b)] Dipartimento di Fisica E. Fermi, Università di Pisa, Pisa, Italy
[125] Department of Physics and Astronomy, University of Pittsburgh, Pittsburgh PA, United States of America
[126] [(a)] Laboratório de Instrumentação e Física Experimental de Partículas - LIP, Lisboa; [(b)] Faculdade de Ciências, Universidade de Lisboa, Lisboa; [(c)] Department of Physics, University of Coimbra, Coimbra; [(d)] Centro de Física Nuclear da Universidade de Lisboa, Lisboa; [(e)] Departamento de Fisica, Universidade do Minho, Braga; [(f)] Departamento de Fisica Teorica y del Cosmos and CAFPE, Universidad de Granada, Granada (Spain); [(g)] Dep Fisica and CEFITEC of Faculdade de Ciencias e Tecnologia, Universidade Nova de Lisboa, Caparica, Portugal
[127] Institute of Physics, Academy of Sciences of the Czech Republic, Praha, Czech Republic
[128] Czech Technical University in Prague, Praha, Czech Republic
[129] Faculty of Mathematics and Physics, Charles University in Prague, Praha, Czech Republic
[130] State Research Center Institute for High Energy Physics, Protvino, Russia
[131] Particle Physics Department, Rutherford Appleton Laboratory, Didcot, United Kingdom
[132] [(a)] INFN Sezione di Roma; [(b)] Dipartimento di Fisica, Sapienza Università di Roma, Roma, Italy
[133] [(a)] INFN Sezione di Roma Tor Vergata; [(b)] Dipartimento di Fisica, Università di Roma Tor Vergata, Roma, Italy
[134] [(a)] INFN Sezione di Roma Tre; [(b)] Dipartimento di Matematica e Fisica, Università Roma Tre, Roma, Italy
[135] [(a)] Faculté des Sciences Ain Chock, Réseau Universitaire de Physique des Hautes Energies - Université Hassan II, Casablanca; [(b)] Centre National de l'Energie des Sciences Techniques Nucleaires, Rabat; [(c)] Faculté des Sciences Semlalia, Université Cadi Ayyad, LPHEA-Marrakech; [(d)] Faculté des Sciences, Université Mohamed Premier and LPTPM, Oujda; [(e)] Faculté des sciences, Université Mohammed V, Rabat, Morocco
[136] DSM/IRFU (Institut de Recherches sur les Lois Fondamentales de l'Univers), CEA Saclay (Commissariat à l'Energie Atomique et aux Energies Alternatives), Gif-sur-Yvette, France
[137] Santa Cruz Institute for Particle Physics, University of California Santa Cruz, Santa Cruz CA, United States of America
[138] Department of Physics, University of Washington, Seattle WA, United States of America
[139] Department of Physics and Astronomy, University of Sheffield, Sheffield, United Kingdom
[140] Department of Physics, Shinshu University, Nagano, Japan
[141] Fachbereich Physik, Universität Siegen, Siegen, Germany
[142] Department of Physics, Simon Fraser University, Burnaby BC, Canada
[143] SLAC National Accelerator Laboratory, Stanford CA, United States of America
[144] [(a)] Faculty of Mathematics, Physics & Informatics, Comenius University, Bratislava; [(b)] Department of Subnuclear Physics, Institute of Experimental Physics of the Slovak Academy of Sciences, Kosice,

Slovak Republic
[145] [(a)] Department of Physics, University of Cape Town, Cape Town; [(b)] Department of Physics, University of Johannesburg, Johannesburg; [(c)] School of Physics, University of the Witwatersrand, Johannesburg, South Africa
[146] [(a)] Department of Physics, Stockholm University; [(b)] The Oskar Klein Centre, Stockholm, Sweden
[147] Physics Department, Royal Institute of Technology, Stockholm, Sweden
[148] Departments of Physics & Astronomy and Chemistry, Stony Brook University, Stony Brook NY, United States of America
[149] Department of Physics and Astronomy, University of Sussex, Brighton, United Kingdom
[150] School of Physics, University of Sydney, Sydney, Australia
[151] Institute of Physics, Academia Sinica, Taipei, Taiwan
[152] Department of Physics, Technion: Israel Institute of Technology, Haifa, Israel
[153] Raymond and Beverly Sackler School of Physics and Astronomy, Tel Aviv University, Tel Aviv, Israel
[154] Department of Physics, Aristotle University of Thessaloniki, Thessaloniki, Greece
[155] International Center for Elementary Particle Physics and Department of Physics, The University of Tokyo, Tokyo, Japan
[156] Graduate School of Science and Technology, Tokyo Metropolitan University, Tokyo, Japan
[157] Department of Physics, Tokyo Institute of Technology, Tokyo, Japan
[158] Department of Physics, University of Toronto, Toronto ON, Canada
[159] [(a)] TRIUMF, Vancouver BC; [(b)] Department of Physics and Astronomy, York University, Toronto ON, Canada
[160] Faculty of Pure and Applied Sciences, University of Tsukuba, Tsukuba, Japan
[161] Department of Physics and Astronomy, Tufts University, Medford MA, United States of America
[162] Centro de Investigaciones, Universidad Antonio Narino, Bogota, Colombia
[163] Department of Physics and Astronomy, University of California Irvine, Irvine CA, United States of America
[164] [(a)] INFN Gruppo Collegato di Udine, Sezione di Trieste, Udine; [(b)] ICTP, Trieste; [(c)] Dipartimento di Chimica, Fisica e Ambiente, Università di Udine, Udine, Italy
[165] Department of Physics, University of Illinois, Urbana IL, United States of America
[166] Department of Physics and Astronomy, University of Uppsala, Uppsala, Sweden
[167] Instituto de Física Corpuscular (IFIC) and Departamento de Física Atómica, Molecular y Nuclear and Departamento de Ingeniería Electrónica and Instituto de Microelectrónica de Barcelona (IMB-CNM), University of Valencia and CSIC, Valencia, Spain
[168] Department of Physics, University of British Columbia, Vancouver BC, Canada
[169] Department of Physics and Astronomy, University of Victoria, Victoria BC, Canada
[170] Department of Physics, University of Warwick, Coventry, United Kingdom
[171] Waseda University, Tokyo, Japan
[172] Department of Particle Physics, The Weizmann Institute of Science, Rehovot, Israel
[173] Department of Physics, University of Wisconsin, Madison WI, United States of America
[174] Fakultät für Physik und Astronomie, Julius-Maximilians-Universität, Würzburg, Germany
[175] Fachbereich C Physik, Bergische Universität Wuppertal, Wuppertal, Germany
[176] Department of Physics, Yale University, New Haven CT, United States of America
[177] Yerevan Physics Institute, Yerevan, Armenia
[178] Centre de Calcul de l'Institut National de Physique Nucléaire et de Physique des Particules (IN2P3),

Villeurbanne, France
[a] Also at Department of Physics, King's College London, London, United Kingdom
[b] Also at Institute of Physics, Azerbaijan Academy of Sciences, Baku, Azerbaijan
[c] Also at Novosibirsk State University, Novosibirsk, Russia
[d] Also at TRIUMF, Vancouver BC, Canada
[e] Also at Department of Physics, California State University, Fresno CA, United States of America
[f] Also at Department of Physics, University of Fribourg, Fribourg, Switzerland
[g] Also at Departamento de Fisica e Astronomia, Faculdade de Ciencias, Universidade do Porto, Portugal
[h] Also at Tomsk State University, Tomsk, Russia
[i] Also at CPPM, Aix-Marseille Université and CNRS/IN2P3, Marseille, France
[j] Also at Universita di Napoli Parthenope, Napoli, Italy
[k] Also at Institute of Particle Physics (IPP), Canada
[l] Also at Particle Physics Department, Rutherford Appleton Laboratory, Didcot, United Kingdom
[m] Also at Department of Physics, St. Petersburg State Polytechnical University, St. Petersburg, Russia
[n] Also at Louisiana Tech University, Ruston LA, United States of America
[o] Also at Institucio Catalana de Recerca i Estudis Avancats, ICREA, Barcelona, Spain
[p] Also at Graduate School of Science, Osaka University, Osaka, Japan
[q] Also at Department of Physics, National Tsing Hua University, Taiwan
[r] Also at Department of Physics, The University of Texas at Austin, Austin TX, United States of America
[s] Also at Institute of Theoretical Physics, Ilia State University, Tbilisi, Georgia
[t] Also at CERN, Geneva, Switzerland
[u] Also at Georgian Technical University (GTU),Tbilisi, Georgia
[v] Also at Manhattan College, New York NY, United States of America
[w] Also at Hellenic Open University, Patras, Greece
[x] Also at Institute of Physics, Academia Sinica, Taipei, Taiwan
[y] Also at LAL, Université Paris-Sud and CNRS/IN2P3, Orsay, France
[z] Also at Academia Sinica Grid Computing, Institute of Physics, Academia Sinica, Taipei, Taiwan
[aa] Also at School of Physics, Shandong University, Shandong, China
[ab] Also at Moscow Institute of Physics and Technology State University, Dolgoprudny, Russia
[ac] Also at Section de Physique, Université de Genève, Geneva, Switzerland
[ad] Also at International School for Advanced Studies (SISSA), Trieste, Italy
[ae] Also at Department of Physics and Astronomy, University of South Carolina, Columbia SC, United States of America
[af] Also at School of Physics and Engineering, Sun Yat-sen University, Guangzhou, China
[ag] Also at Faculty of Physics, M.V.Lomonosov Moscow State University, Moscow, Russia
[ah] Also at National Research Nuclear University MEPhI, Moscow, Russia
[ai] Also at Department of Physics, Stanford University, Stanford CA, United States of America
[aj] Also at Institute for Particle and Nuclear Physics, Wigner Research Centre for Physics, Budapest, Hungary
[ak] Also at University of Malaya, Department of Physics, Kuala Lumpur, Malaysia
[*] Deceased